2014

MULTIFERROIC NANOMAGNETIC LOGIC: HYBRID SPINTRONICS-STRAINTRONIC PARADIGM FOR ULTRA-LOW ENERGY COMPUTING

Mohammad Salehi Fashami
Virginia Commonwealth University

MULTIFERROIC NANOMAGNETIC LOGIC: HYBRID SPINTRONICS-STRAINTRONIC PARADIGM FOR ULTRA-LOW ENERGY COMPUTING

A dissertation submitted in partial fulfillment of the requirements for the degree of Doctor of Philosophy in Engineering at Virginia Commonwealth University.

by

Mohammad Salehi Fashami
M.Sc Amirkabir University of Technology (Tehran Polytechnic), IRAN, 2007.

Director: Jayasimha Atulasimha, PhD.
Associate Professor, Department of Mechanical and Nuclear Engineering
School of Engineering

Virginia Commonwealth University
Richmond, Virginia
August 2014

Dedication

This dissertation is dedicated to my ***wife***, my ***parents*** and my ***grandmother*.**

Acknowledgement

I would like to acknowledge discussions with Prof. J. Atulasimha and Prof. S. Bandyopadhyay at The Virginia Commonwealth University on many aspects of this dissertation and also Prof. A. W. Ghosh at The University of Virginia for discussions of the effect of thermal noise on multiferroic nanomagnetic logic. I also thank my other PhD committee members, Prof. S. N. Khanna, Prof. H. V. Tafreshi and Prof. G. C. Tepper for their time and feedback on my work. Finally, I thank my lab mates who were a constant source of support during my PhD. I also acknowledge Dr. M. Donahue at NIST for discussions on Object-Oriented Micromagnetic Framework (OOMMF) simulations. In addition, I would like to acknowledge Prof D. Pestov, Prof G. Atkinson and Prof E. Carpenter for providing excellent environment at the VCU Nano center (NCC) and Wright Virginia Microelectronics Center(WVMC)for research, nano-fabrication and characterization.

This work is supported by the National Science Foundation (NSF) under NSF CAREER grant CCF- 1253370, the NEB2020 Grant ECCS-1124714 and SHF grant CCF-1216614 as well as the Semiconductor Research Company (SRC) under NRI task 2203.001.

Table of Contents

Page

List of Tables viii

List of Figures ix

Abstract xii

Chapter

1 Introduction 1

1.1 Transistors 1
1.2 Straintronic nanomagnetic logic devices (SML) 3
1.2.1 Dissipation limits: transistor versus nanomagnet 3
1.2.2 Clocking nanomagnetic logic (NML): the Achilles' heal 4
1.2.3 Multiferroic nanomagnet: Paradigm that offers ultra low energy clocking 5
1.2.4 Potential application for ultra low power straintronic nanomagnetic logic devices 7

1.3 Magnetic domains and nanomagnetism 7
1.3.1 Paramagnetic and ferromagnetic behavior: Role of exchange coupling 8
1.3.2 Domains in ferromagnetic materials: Illustrating the effects of exchange coupling energy, magnetocrystalline anisotropy energy and magnetostatic energy 8
1.3.3 Single domain states: why this is preferred when dimensions~ 100nm or less 10

1.4 Introduction to nanomagnetic logic 13
1.4.1 The multiferroic nanomagnetic chain and wires 14
1.4.2 The multiferroic nanomagnetic logic gate 15

1.5 Thermal effect of magnetization dynamics in nanomagnets 15

1.6 Dissertation overview 16

2 Magnetization dynamics and theory of multiferroic nanomagnetic logic 19

2.1 Introduction 19

2.2 The fundamental concepts 20

2.3 Exchange coupling energy.....21

2.4 Magnetostatic shape energy 23

2.5 Magnetoelastic energy (stress anisotropy) 26

2.6 Dipole coupling energy 27

2.7 Energy terms in nanomagnetic structures 29

2.8 Magnetization dynamics and Landau-Lifshitz-Gilbert (LLG) equation..31

2.9 Energy dissipation 34

3 Bennett clocking with strain in multiferroic nanomagnets for unidirectional logic propagation in a nanomagnetic “wire” and a universal logic (NAND) gate...36

3.1 The energy landscape and static behavior of nanomagnet 37

3.2 Critical stress 41

3.3 The multiferroic nanomagnetic logic “wires” 42

3.3.1 Case 1: Compressive stress of 5.2 MPa is applied instantaneously on multiferroic nanomagnets 2 and 3 by applying a potential of 26 mV, followed by instantaneous removal of stress from multiferroic nanomagnet 2 after its magnetization aligns close to the in-plane hard axis.....48

3.3.2 - Case 2: Compressive stress of 40 MPa is applied on multiferroic nanomagnets 2 and 3 to align their magnetizations along the hard axis, followed by applying a tensile stress of 40 MPa on multiferroic nanomagnet 2 to help it relax to its easy axis faster and in the process flipping its magnetization.....53

3.3.3 Conclusion for multiferroic nanomagnetic logic.....58

3.4 The universal multiferroic nanomagnetic logic gate 59
3.4.1 Magnet switching schemes 60
3.4.2 Results and discussions 63
3.4.3 Energy considerations: power dissipated internally in the magnets and externally in the clock 70

3.5 Conclusions 73

4 Behavior of multiferroic nanomagnetic logic in the presence of thermal noise 75

4.1 Overview 75
4.2 Introduction 75

4.3 Modeling magnetization dynamics in the presence of thermal noise ...77

4.4 Analysis of switching error in the presence of thermal noise 82
4.4.1 Effect of dipole coupling at various stress levels 83
4.4.2 Effect of stress withdrawal time (ramp rate) at various stress levels .87
4.4.3 The use of sinusoidal clocking at different stress levels 89
4.4.4 Increased dipole coupling 92

4.5 Multiferroic nanomagnetic NAND gate error 93

4.6 Conclusions 96

5 Limits to energy dissipation vs. error rate in practical nanomagnetic logic in the presence of thermal noise 97

Overview 97

5.1 Introduction 98

5.2 Discussion 100

5.3. Conclusions 113

6 Magnetization dynamics with Surface Acoustic Waves (SAWs) 114

6.1 Overview 114

6.2 Introduction 114

6.3 Results 116

6.4 Conclusion.....122

7 Implementation of 4-state nanomagnetic devices with shape anisotropy.....123

7.1 Overview 123

7.2 Introduction 124

7.3 Method: micro magnetic modeling 126

7.4 Results 129
7.4.1. Nonlinear magnetization hysteresis and Anisotropy Field.....130
7.4.2 Switching modes in diamond- and concave-shaped nanomagnets ..133
7.4.3 Magnetization dynamics.....136
7.4.4 Strain control 4-State nanomagnet 138

7.5 Discussion 141

7.6 Four-State nanomagnetic device fabrication.....142

7.7 Conclusion.....148

8 Conclusions and future work 150

8.1 Conclusions. 150

8.2 Future work 153

References.....154

List of Tables

Page

Table 3.1 :Material parameter and geometric design for Terfenol-D.....65

Table 4.1 : Material parameter and geometric design for Terfenol-D. 79

List of Figures

Page

Figure 1.1 2
Figure 1.2 6
Figure 1.3 9
Figure 1.4 11
Figure 1.5 12
Figure 1.6 13
Figure 1.7 13
Figure 1.8 14
Figure 1.9 15
Figure 1.10 16

Figure 2.1 25
Figure 2.2 27
Figure 2.3 28

Figure 3.1 38
Figure 3.2 39
Figure 3.3 40
Figure 3.4 41
Figure 3.5 43
Figure 3.6 46
Figure 3.7 50
Figure 3.8 52
Figure 3.9 53
Figure 3.10 55
Figure 3.11 57
Figure 3.12 58
Figure 3.13 60
Figure 3.14 62
Figure 3.15 64
Figure 3.16 67
Figure 3.17 68
Figure 3.18 69
Figure 3.19 70

Figure 4.1 76
Figure 4.2 81
Figure 4.3 83
Figure 4.4 84
Figure 4.5 86
Figure 4.6 87
Figure 4.7 88
Figure 4.8 89
Figure 4.9 90
Figure 4.10 91
Figure 4.11 93
Figure 4.12 94
Figure 4.13 95
Figure 4.14 95

Figure 5.1. 98
Figure 5.2. 101
Figure 5.3 102
Figure 5.4. 104
Figure 5.5. 105
Figure 5.6. 107
Figure 5.7. 109
Figure 5.8. 111
Figure 5.9. 112

Figure 6.1 118
Figure 6.2 119
Figure 6.3(a,b)....120
Figure 6.3(c,d)....121

Figure 7.1 127
Figure 7.2(a)....130
Figure 7.2(b) 131
Figure 7.3 132
Figure 7.4(a)....134
Figure 7.4(b) 135
Figure 7.4(c)....136

Figure 7.5(a).....137
Figure 7.5(b) 138
Figure 7.6(a).....139
Figure 7.6(b) 140
Figure 7.6(c).....141
Figure 7.6(d) 143
Figure 7.7 144
Figure 7.8 145
Figure 7.9 146
Figure 7.10(a,b).....147
Figure 7.11 148

Figure 8.1 152

Abstract

MULTIFERROIC NANOMAGNETIC LOGIC: HYBRID SPINTRONICS-STRAINTRONIC PARADIGM FOR ULTRA-LOW ENERGY COMPUTING

By Mohammad Salehi Fashami
A dissertation submitted in partial fulfillment of the requirements for the degree of Doctor of Philosophy at Virginia Commonwealth University.

Virginia Commonwealth University, 2014

Director: Jayasimha Atulasimh, PhD.
Associate Professor, Department of Mechanical and Nuclear Engineering
School of Engineering

Excessive energy dissipation in CMOS devices during switching is the primary threat to continued downscaling of computing devices in accordance with Moore's law. In the quest for alternatives to traditional transistor based electronics, nanomagnet-based computing [1, 2] is emerging as an attractive alternative since: (i) nanomagnets are intrinsically more energy-efficient than transistors due to the *correlated* switching of spins [3], and (ii) unlike transistors, magnets have no leakage and hence have no standby power dissipation. However, large energy dissipation in the clocking circuit appears to be a barrier to the realization of ultra low power logic devices with such nanomagnets. To alleviate this issue, we propose the use of a hybrid spintronics-straintronics or straintronic nanomagnetic logic (SML) paradigm. This uses a piezoelectric layer elastically coupled to an elliptically shaped magnetostrictive nanomagnetic layer for both logic [4-6] and memory [7-8] and

other information processing [9-10] applications that could potentially be 2-3 orders of magnitude more energy efficient than current CMOS based devices. This dissertation focuses on studying the feasibility, performance and reliability of such nanomagnetic logic circuits by simulating the nanoscale magnetization dynamics of dipole coupled nanomagnets clocked by stress. Specifically, the topics addressed are:

1. Theoretical study of multiferroic nanomagnetic arrays laid out in specific geometric patterns to implement a "logic wire" for unidirectional information propagation and a universal logic gate [4-6].
2. Monte Carlo simulations of the magnetization trajectories in a simple system of dipole coupled nanomagnets and NAND gate described by the Landau-Lifshitz-Gilbert (LLG) equations simulated in the presence of random thermal noise to understand the dynamics switching error [11, 12] in such devices.
3. Arriving at a lower bound for energy dissipation as a function of switching error [13] for a practical nanomagnetic logic scheme.
4. Clocking of nanomagnetic logic with surface acoustic waves (SAW) to drastically decrease the lithographic burden needed to contact each multiferroic nanomagnet while maintaining pipelined information processing.
5. Nanomagnets with four (or higher states) implemented with shape engineering. Two types of magnet that encode four states: (i) diamond, and (ii) concave nanomagnets are studied for coherence of the switching process.

Chapter 1

Introduction

This dissertation describes research towards the understanding of Straintronic Multiferroic Nanomagnetic Logic devices (SML), which are capable of performing universal computations, while dissipating very little energy (2-3 orders of magnitude less than the state of the art transistors). The Straintronic Multiferroic Nanomagnetic Logic (SML) devices are based on: (i) mechanical strain produced by a bottom piezoelectric layer that is transferred to the magnetostrictive layer which rotates the magnetization through a large angle ("clocks it") due to the magnetoelastic coupling and (ii) nearest-neighbor interaction (dipole-coupling) between neighboring single domain nanomagnets that is elicited to propagate information and perform logic operation. In this section, we will begin with a background on semiconductor devices and an overview of magnetism and nanomagnetic computing in order to motivate the need for such SML devices.

1.1 Transistors

J. Barden and W. Brattain demonstrated the first transistor in 1947 and in 1956, along with their supervisor W. Shockley, were awarded the Nobel prize for this invention that has revolutionized the world and the computer industry. It was later considered as one of the most important inventions in 20th century. The transistor rapidly displaced the three terminal vacuum tube device that preceded them, which had the disadvantages of large size, slow start up and large

power dissipation. By development of the IC technology, the number of transistors per unit area has been increased at a predicted rate, known as the Moore's law that states that "the numbers of transistors on integrated circuits (IC) would double in every two years."

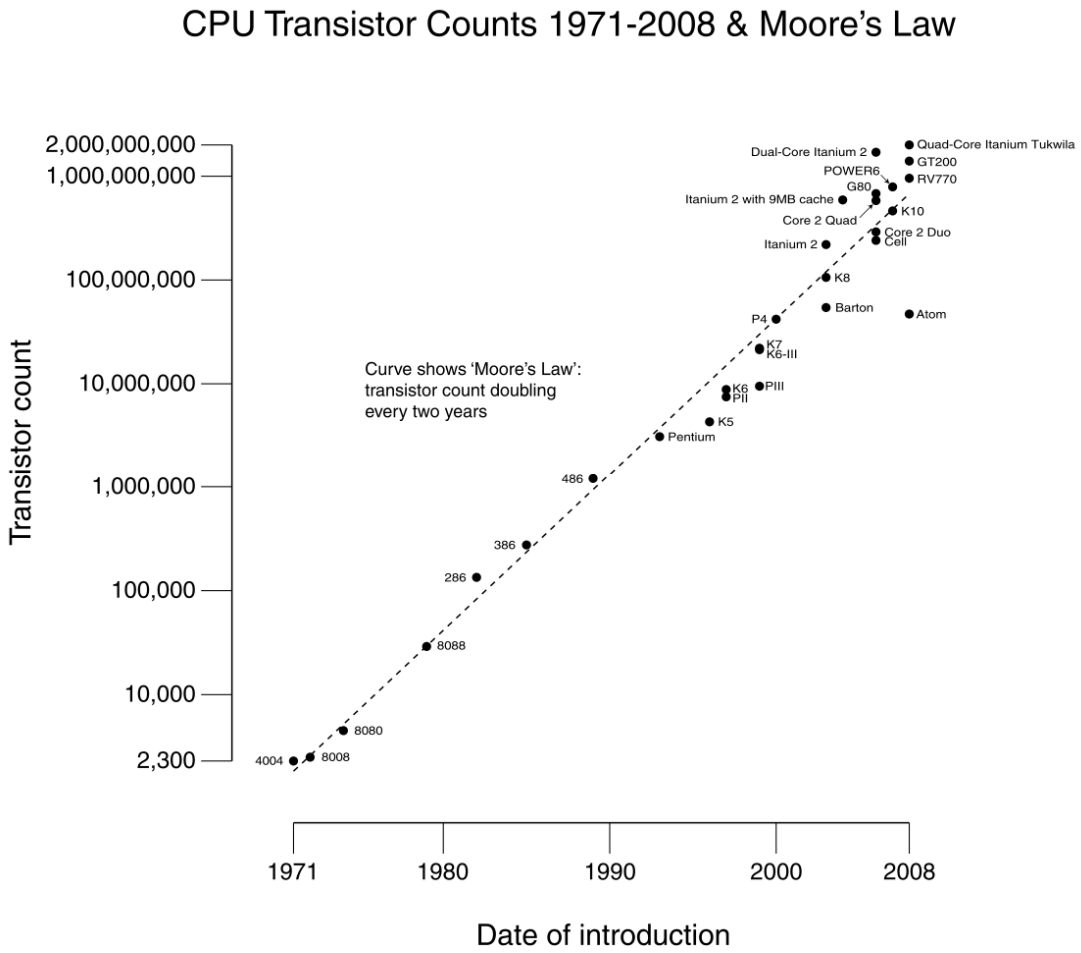

Fig 1.1.The exponential increasing of transistors density on IC based on the Moore's Law [14].

When the transistors were scaled down, they operated faster, dissipated less energy and cost less for manufacturing. Down scaling of transistors in ICs has led to devices with gate lengths nearing 20 nm. However, further down scaling of CMOS is severely challenged by high circuit power

densities and energy dissipation of the basic switching element. This is the strong motivation for developing ultra low power computing devices. Another equally important motivation for developing extremely energy efficient computing devices is their potential use in embedded application such as medically implemented processors and distributed sensing/monitoring systems where energy is a premium. As a result, the semiconductor industry is looking for new computing devices with unprecedented energy efficiency to replace the transistor. In order to realize such a device, researchers have been working on several novel device concepts and computational paradigms that are able to replace CMOS transistors (charge based devices) with other physical quantities such as spin (magnetism). One such device concept employs a bi-stable single domain nanomagnet whose magnetization orientation encodes a bit of information [1-2].

1.2 Straintronic nanomagnetic logic devices (SML)

This section briefly explains the reason why spin based logic, in particular nanomagnetic logic, has great potential to emerge as an extremely energy efficient switching device. Further, the problem with nanomagnetic logic, viz. the energy dissipation in the clocking circuit is discussed. Finally, the reason why clocking/switching nanomagnets with strain using multiferroic nanomagnets could solve this problem is discussed.

1.2.1 Dissipation limits: transistor versus nanomagnet

It can be shown from fundamental arguments that the *minimum* energy dissipated in switching a transistor at a temperature T is $NkTln(1/p)$ independent of the switching speed , where N is the number of information carriers (electrons) in the transistor, k is the Boltzmann constant, and p is the bit error probability. On the other hand, the minimum energy dissipated to switch a *single-*

domain magnet's magnetization is ~ *kTln(1/p)*, since the *exchange interaction* between many spins makes all of them behave collectively like a giant single spin [3,15] and rotate in *unison* to switch the magnetization [3]. Thus, if we assume the same number of information carriers in a transistor and in a single domain nanomagnet, then for the same bit error probability, the ratio of the minimum energy dissipated to switch a magnet to that dissipated to switch a transistor will be ~1/N <<1. This makes the magnet *intrinsically* much more energy-efficient than the transistor as a logic switch. Note that it is the mutual *interaction* between spins (exchange interaction), which is absent between charges – and not any inherent advantage of spin over charge, – that gives the magnet this advantage.

Thus, nanomagnet-based computing has two advantages over traditional transistor based electronics since: (i) magnets are intrinsically more energy-efficient than transistors, and (ii) unlike transistors, magnets suffer from no leakage and hence *no standby power dissipation.*

1.2.2 Clocking Nanomagnetic Logic (NML): The Achilles' heel

Despite these advantages, nanomagnet–based technology [1, 2, 16] has not been able to displace transistor technology because the methods employed to switch or clock these nanomagnets dissipate a lot of energy and hence do not exploit the advantage of the nanomagnet [17]. Some such switching techniques are:

(i) A magnetic field generated by a current: In this approach, [18] a magnetic field is generated by a current based on Ampere's law: $I = \int_c \vec{H} \cdot d\vec{l}$. The minimum magnetic field $\vec{H}_{\min}$ required to flip a magnet is found by equating the magnetic energy in the field to the energy barrier E_b separating the two stable magnetization directions encoding the bits 0 and 1 in a shape-anisotropic

nanomagnet, i.e. $\mu_0 M_s H_{\min} \Omega = E_b$, where μ_0 is the permeability of free space, M_s is the saturation magnetization which we assume is 10^5 A/m (typical value for nickel or cobalt), and Ω is the magnet's volume which we assume is ~$105\ \text{nm} \times 95\ \text{nm} \times 6\ \text{nm}$ which guarantees that the magnet is in a single-domain state The energy barrier determines the equilibrium bit error probability $e^{-E_b/kT}$. For reasonable error rate, we should ensure that $E_b \geq 30kT$, which yields an $I_{\min}$ = 6 mA. The resistance *R* of the magnet is typically 1-10 ohms, so that the energy dissipated, assuming that the magnet flips in Δt =1 ns, is $I_{\min}^2 R \Delta t$ = 36-360 fJ, or 10^7-10^8kT.

(ii) With a spin transfer torque delivered by a spin polarized current: Spin transfer torque is a method of switching a magnet by driving a spin-polarized current through it. The magnetization flips in the direction of spin polarization because of angular momentum transfer [19]. This method dissipates about $10^8 kT$of energy to switch a single-domain nanomagnet in ~ 1 ns, even when the energy barrier within the magnet is only ~ 30 *kT* [7].

(iii) With domain wall motion induced by a spin polarized current: In this method, a magnet is switched by inducing domain wall motion [20]. The switching of a multi-domain nanomagnet may be possible in ~2 ns while dissipating $10^4 kT$– $10^5 kT$of energy [21]. However, this is still 2-3 orders of magnitude more dissipative than what will be shown to be achievable with "straintronics", where a multiferroic nanomagnet is switched with mechanical strain generated by a tiny voltage [5-7].

1.2. 3 Multiferroic nanomagnets: paradigm that offers ultra low energy clocking

A multiferroic structure consists of a piezoelectric layer (e.g. PZT) elastically coupled to a *single domain* magnetostrictive layer (e.g. Nickel or Terfenol-D) as shown in Fig 1.2.

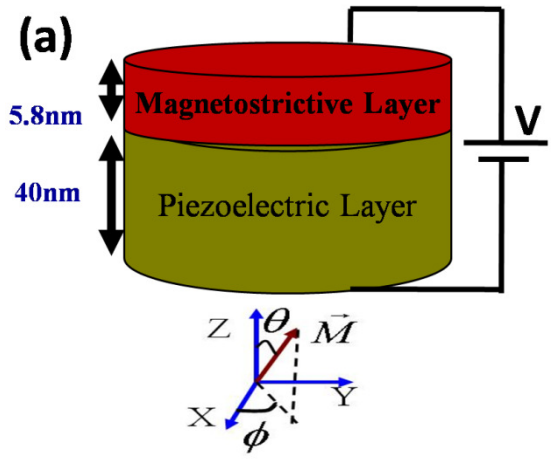

Fig 1.2. Schematic view of a multiferroic nanomagnet with bottom layer of PZT and top layer of magnetostrictive material.

When an electric potential is applied across the piezoelectric layer, it deforms elastically. The resulting stress/strain is transferred to the magnetostrictive layer on top and causes the latter's magnetization to rotate[95,96]. For materials with positive magnetostriction (e.g. Terfenol-D), tensile stress favors a magnetization orientation parallel to itself and compressive stress favors a magnetization orientation perpendicular to itself [5,22]. Thus, if we apply compressive stress along the "easy axis" of the magnet (which is the major axis of the ellipse shown in Fig. 1.2, or the y-axis), then the magnetization will rotate towards the in-plane hard axis, or the minor axis (x-axis).When the stress is withdrawn the magnetization is now in an unstable state and will have roughly equal likelihood of returning to the original stable orientation (not flipping,

or 0◦ rotation) or flipping to the other stable orientation (180◦ rotation). That makes the flipping only 50% likely, which is unacceptable. However, if a neighboring nanomagnet has a specific

magnetic orientation, dipole coupling from the neighboring magnet favors the magnetization of this magnet relaxing from the hard axis to a state anti-parallel to its magnetization orientation. This forms the basis of nanomagnetic logic discussed in this dissertation. There are also various schemes to implement memory with a single, isolated multiferroic nanomagnet, but this is beyond the scope of this dissertation and is not discussed here.

In the above configuration, when an electric field is applied in the z-direction, we ensure that it produces uniaxial tension or compression exclusively along the *y*-axis by mechanically restraining the PZT layer from expansion or contraction along the *x*-axis. The same can be achieved by applying the electric field along the *y*-direction, which will generate a stress along it, but this is harder as it requires lateral contacts.

1.2.4 Potential applications for ultra low power straintronic nanomagnetic logic devices

While traditional computing applications could be one potential application of straintronic multiferroic nanomagnetic logic (SML) devices, due to their extremely small energy requirements they can potentially be used to build processors that can just be driven from energy harvested from the ambient vibrations or stray electromagnetic fields. Such processors can have *unique* applications in medically implanted devices powered by motion of the human body, "wrist-watch" computers that are powered by the wearer's arm motion, or processors for structural health monitoring that process inputs from sensors attached to bridges and building that are powered by the mechanical vibrations of the structure due to wind or passing traffic.

1.3 Magnetic domains and nanomagnetism

This section gives an overview of magnetic materials (in particular ferromagnetic materials) and explains what leads to the formation of domains in magnetic micro and macro-scale materials.

It then explains how nanomagnetic structures have a strong tendency to exhibit single domain behavior and how this can be exploited to encode a logic state or a bit of information.

1.3.1 Paramagnetic and ferromagnetic behavior: Role of exchange coupling

In some materials that have net magnetic moment, the moments locally tend to align with an applied magnetic field. Thus the magnetization produced in the material is proportional and is in the direction of the applied magnetic field. This is known as paramagnetism. In certain solids, such as iron, nickel and cobalt, the moments in neighboring atoms are strongly coupled (due to exchange coupling) and tend to align with each other at room temperature. Thus, even in the absence of magnetic fields there is spontaneous magnetization in the material, this is typical of ferromagnetic materials. At sufficiently high temperature, the thermal energy exceeds the exchange coupling energy between spins and breaks this alignment, leading to a paramagnetic state. The temperature at which this transition from ferromagnetic to paramagnetic state or vice versa occurs is known as the Curie temperature [22].

1.3.2 Domains in ferromagnetic materials: Illustrating the effects of exchange coupling energy, magnetocrystalline anisotropy energy and magnetostatic energy

Macroscopic samples of ferromagnetic materials are formed of magnetic domains, regions where the atomic magnetic moments roughly point in the same direction. The presence of domains with different directions may lead to an approximate cancellation of the total magnetic moment, or to an average magnetization close to zero. However, these domains themselves are “polarized” or contain a non-zero magnetic moment even when no magnetic field is applied to them.

The division of volume of a sample into magnetic domains arises from the balance of the contributions of the different energy terms. This is shown in Fig 1.3.

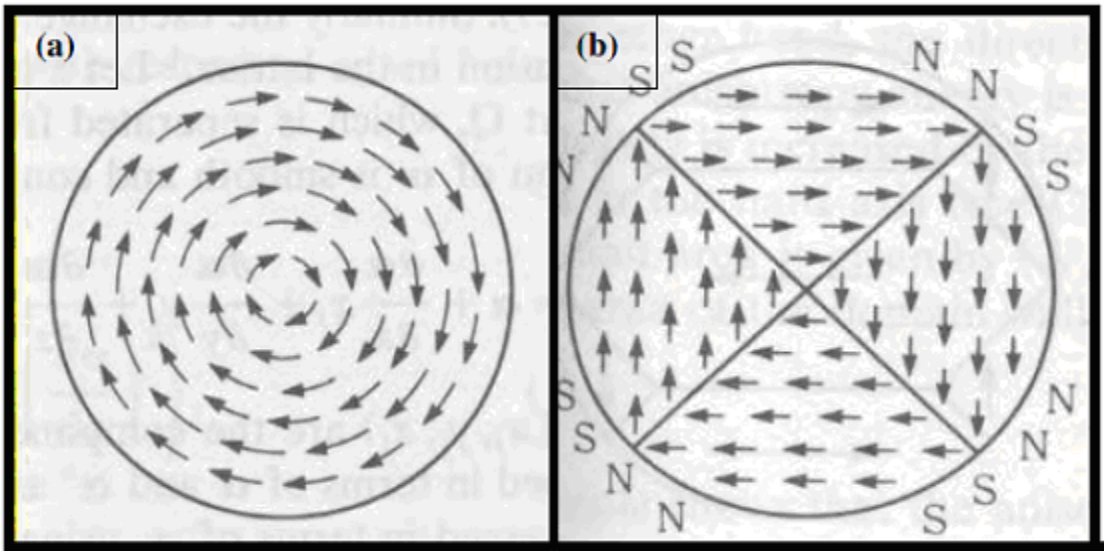

Fig1.3 Domain patterns in discs under different criterion.
(a)Zero magnetocrystalline anisotropy. (b) Cubic magnetocrystalline anisotropy.
[22],[23].

The exchange coupling would favor the formation of one big domain in which all the spins point in the same direction. However, in a macro-sized (or even micro-sized) sample this would lead to a large magnetostatic energy (shape anisotropy energy) penalty due to dipole coupling between the different magnetized regions. Thus, to minimize the magnetostatic energy the formation of a large number of domains is favored but this would also incur a large exchange coupling or

magnetocrystalline anisotropy energy penalty. This is because the presence of a transition region between the domains, the domain walls, also brings about an increase in exchange and anisotropy energy. Two scenarios can emerge (at zero applied field) depending on the magnitude of the magnetocrystalline anisotropy (this energy is minimized when the magnetization (spins) point along preferred crystallographic directions):

(i) Closed flux path or vortex states (see Fig 1.3 a): The magnetic moments would prefer to arrange themselves to form a closed flux path as shown in Figure 1.3 (a). However, this pattern is energetically feasible only if the magnetocrystalline anisotropy is extremely low.

NOTE: The expense of exchange coupling is small in this case, as the difference in orientation between two neighboring moments is small. However, some moments would have to assume orientations which result in large magnetocrystalline anisotropy energy so this is possible only when the material has low magnetocrystalline anisotropy.

(ii) Discrete domains that form a closed flux path (for example, see Fig 1.3b): For materials with cubic anisotropy this typically results in a domain pattern, such as the one seen in Figure 1.3 (b). The moments are oriented along the easy <100>directions leading to small magnetocrystalline anisotropy energy with some expense in exchange coupling energy at the domain boundaries.

1.3.3 Single domain states: why this is preferred when dimensions ~ 100 nm or less

Fig 1.4 shows the formation of multiple domains in a disk of $1\,\mu m$ in diameter. By reducing the length scale of the magnetic structure, the probability of formation of a single domain magnetic state would be increased as the effect of exchange coupling is very strong and forces the spins to point in the same direction. This phenomenon typically occurs when the dimensions of a

magnet is on the order of 100 to 200 nanometers or less. This can be called a single domain nanomagnet. This has a single well-defined magnetization vector orientation with absolute magnitude that equals the saturation magnetization of the ferromagnetic material even in the absence of a magnetic field. The corresponding schematic of a single-domain nanomagnet is shown in fig 1.5.

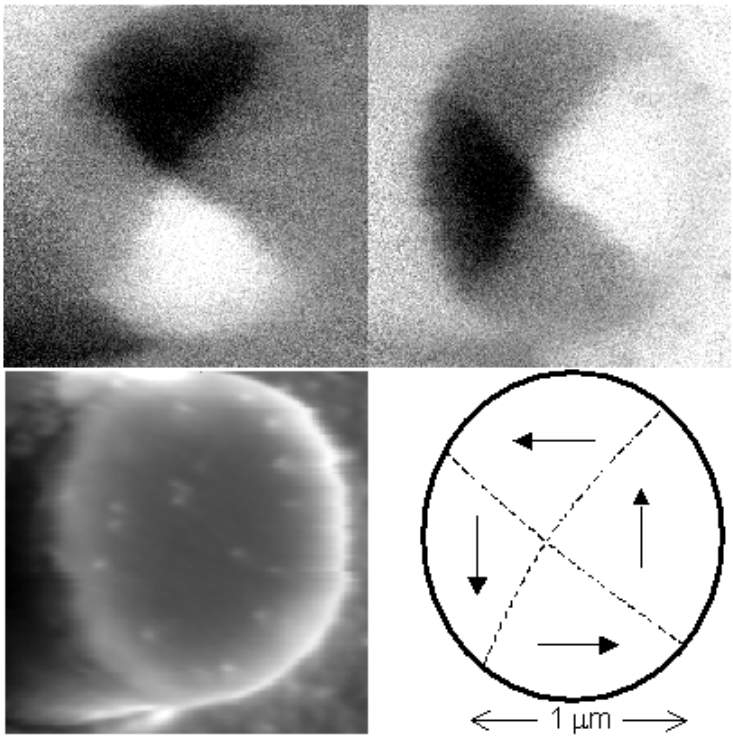

Fig 1.4. A disc with 1 um Diameter shows multi magnetic domains [24].

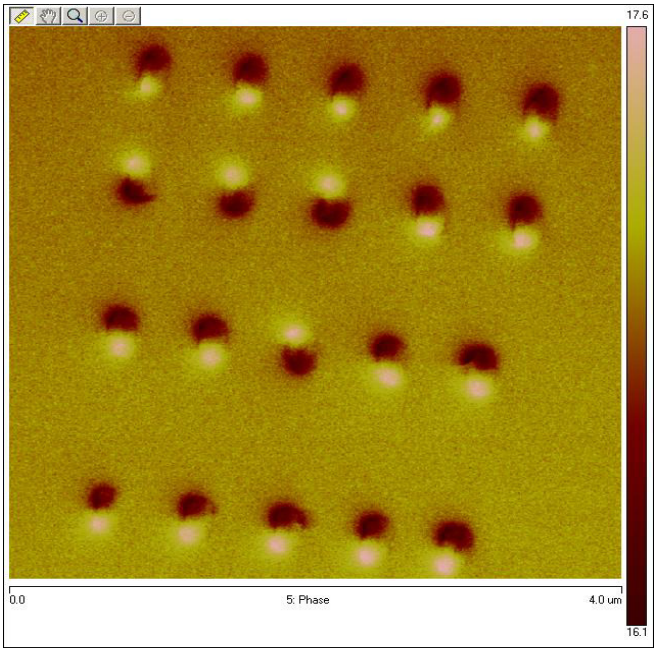

Fig. 1.5. The MFM Image of a single-domain nanomagnet with its magnetization state.

In a single domain nanomagnet, the direction of orientation of magnetization strongly depends on the shape of the nanomagnet. In other words, the shape of a single domain nanomagnet plays an important role in the response of its magnetization vector to stress and field. This property is called shape anisotropy and can be explained as a term that arises from the magnetic moments in a ferromagnet attempting to orient themselves to reduce their energy by minimizing the internal magnetic field (also known as the demagnetizing field).

When a single domain nanomagnet has the shape of a circle, its magnetization vector is free to point in any direction. In a circular magnet there is no shape anisotropy energy barrier for different in-plane magnetization orientations. As a result, its magnetization vector is free to rotate to any angle in response to a small external field or stress. However, this is not true for non-circular structures such as an elliptical shape. The nanomagnet with elliptical shape prefers to have magnetization vector pointing a long its long axis as this is the minimum energy state.

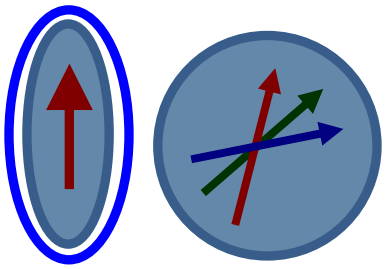

Fig 1.6. The stability of the magnetization orientation vector for elliptical and circular shapes.

Thus in an ellipse, the preferred axis (up/down state) is known as the “easy axis” and can encode the "0" or "1" state. The left/right direction is known as the hard axis and forms an in-plane energy barrier that prevents spontaneous switching between the "0" and "1" states.

1.4 Introduction to nanomagnetic logic

This uniaxial anisotropy single domain nanomagnet can be used to implement computing and propagate information in a unidirectional manner using the dipole-coupling in conjunction with clocking (rotation through large angle) using stress. In chapters 3-5, the nanomagnet is patterned to be elliptical to maintain bistable magnetization orientation. Fig 1.7 shows schematic energy landscape of such a single domain nanomagnet.

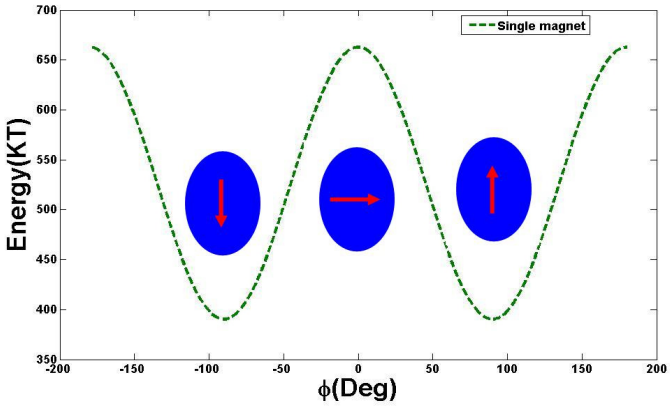

Fig 1.7. Encode binary information of a uniaxial elliptical nanomagnet with its energy landscape due to its shape anisotropy.

1.4.1 The multiferroic nanomagnetic chain and wires

To transfer a bit of information from one magnet to another, a nanomagnetic chain is needed. By placing a chain of single domain nanomagnets next to a fixed input, the information can propagate by removing the energy barrier of each nanomagnet by applying stress through bottom layer (PZT), which causes the nanomagnets to point along their hard axis. Under the influence of the dipole field coupling, the magnet rotates to the desired stable position, upon removal of stress. If magnets are arranged so their hard axes coincide with the direction of the line joining their centers, their magnetizations form an anti-ferromagnetic arrangement. If the hard axes are perpendicular to the line joining the nanomagnet centers (arranged so that their easy axes are lined up), their magnetizations prefer to orient parallel to each other. Through this operation, the magnetization state of the nanomagnet at the beginning of the chain will be transferred to the magnetization state of the nanomagnet at the end of the chain as shown in fig 1.8.

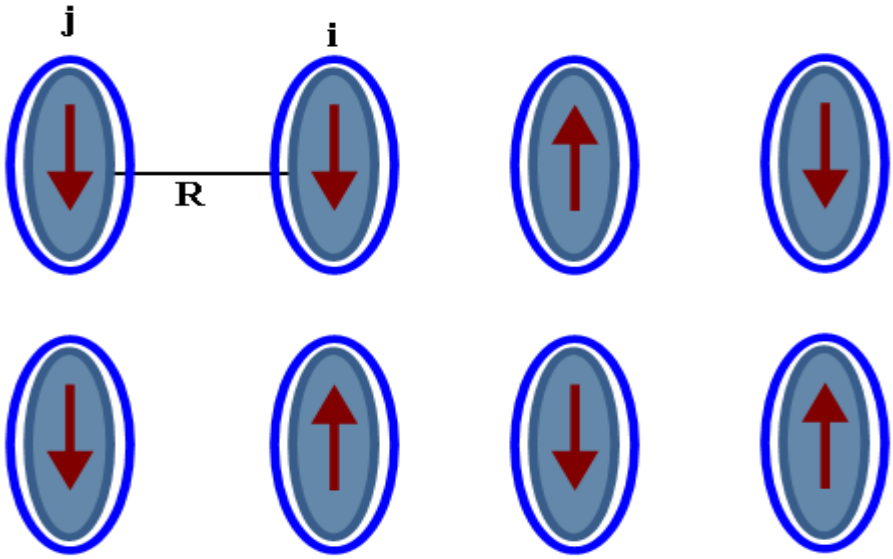

Fig. 1.8 Binary information can be transferred by nanomagnetic wires.

1.4.2 The multiferroic nanomagnetic logic gate

One interesting application of multiferroic nanomagnets is to perform logical computation with nanomagnets. The universal logic gate is composed of input chains and an additional magnet to generate a bias field to resolve a tied state that occurs when one input favors an up state and the other a down state. We will also show in Chapter 3 that the specific geometric layout shown in Fig 1.9 can not only implement a NAND gate but also successfully input fan-out (where output from one stage can be connected to inputs of multiple gates of the next stage).

.

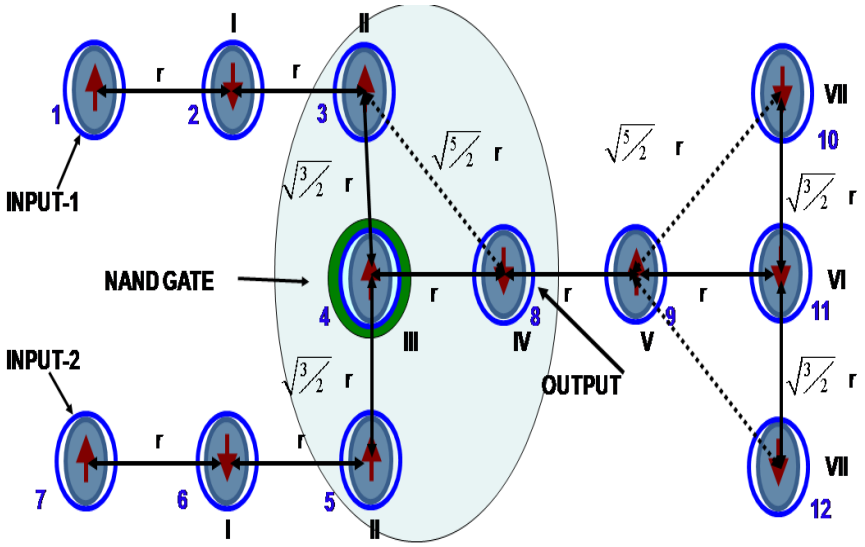

Fig 1.9The schematic of a NAND multiferroic nanomagnetic logic gate with two inputs, bias magnet and output.

1.5 Thermal effect of magnetization dynamics in nanomagnets

While chapter 3 discusses nanomagnetic wires and gates in the absence of thermal noise, it is important to analyze the effect of thermal noise at room temperatures on the performance of nanomagentic logic. This is carried out in chapters 4 and 5 wherein an extra effective field term

due to thermal noise is added. It has an uncorrelated Gaussian distribution and zero mean in all three coordinate axes because the temperature influence should not direct the system in any particular direction.

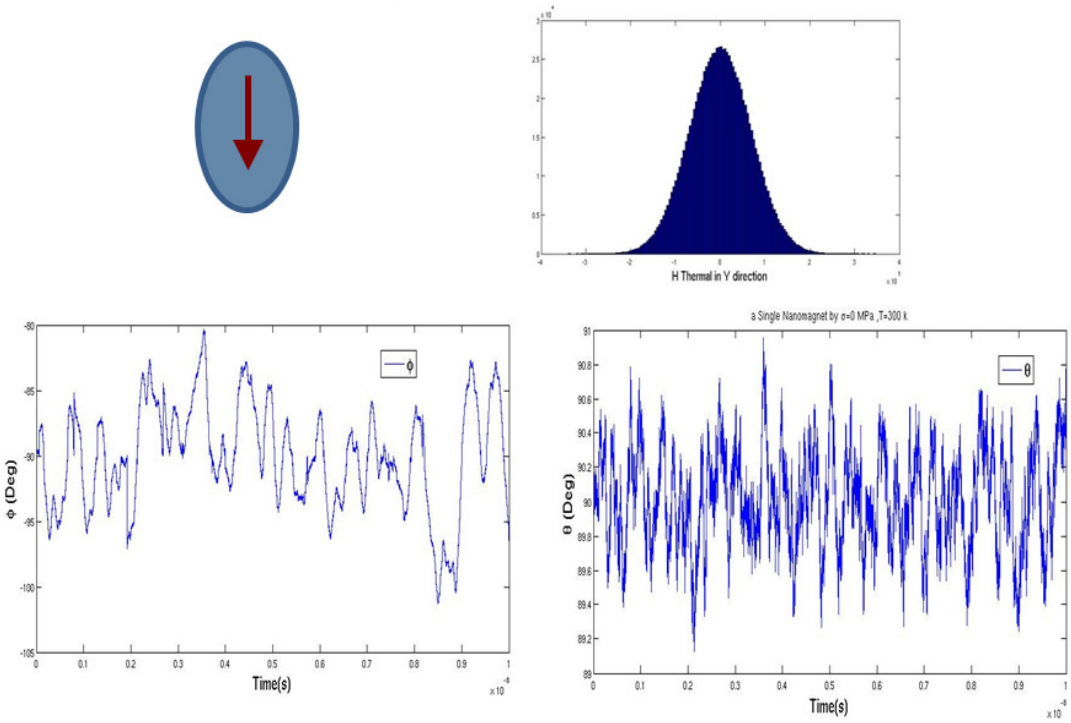

Fig 1.10 T=300 K(room temperature)simulation of magnetization orientation in a single nanomagnet.

1.6 Dissertation overview

In this dissertation, chapter 2 proposes a theoretical formulation for the stress induced magnetization dynamics in dipole coupled nanomagnets. This formulation is used to analyze multiferroic nanomagnetic logic to understand issues of engineering interest such as switching

speed, energy dissipation during switching and reliability (error probability) for the switching process. Specifically:

Chapter 3 analyses the propagation of nanomagnetic logic in a chain of multiferroic nanomagnets (Bennett Clocking) and implementation of a universal logic (NAND) gate with fan-out by appropriate design of the geometric layout for these nanomagnets and 4-phase clocking. This chapter focuses on the magnetization dynamics and high energy efficiency of multiferroic nanomagnetic logic.

Chapter 4 studies the dynamic switching error of a dipole coupled multiferroic nanomagnetic system as a function of various parameters including the dipole strength and concludes that magnetic quantum cellular automata (MQCA) type architectures that rely on dipole coupling are extremely error prone. In the next step, the reliability of a multiferroic NAND gate in the presence of thermal noise was studied. It was found that there are some major factors that have an important influence in correct operation of this architecture such as : (i) dipole coupling (ii) stress level (iii) clocking frequency, and (iv) temperature.

Chapter 5 discusses a *new* switching scheme that does not require a timing synchronization in modulating the barrier (hence fault-tolerant) while dissipating arbitrarily small energy in the absence of thermal noise to switch with 100% reliability. Further, we show that when complex modulation of the potential energy profile of a two well potential is *not* permitted, the least energy that MUST be dissipated to switch with a certain probability (in the presence of thermal noise) approaches the limit $2kTln(1/p)$ [p = switching error probability, T=temperature, k=Boltzmann constant]. This is clearly more conservative (necessitates more energy dissipation) than the minimum bound of $kTln(2)$, popularly known as the Landauer limit [47,51,52]. This case is exemplified using a multiferroic nanomagentic system where we show that energy dissipation will

exceed the limit (lower bound) that we derived due to out-of-plane distribution of the magnetization vector.

In chapter 6, application of Surface Acoustic Waves (SAW) to clock magnetic devices is studied. It is shown that a SAW can clock nanomagnets and transfer information in chain of dipole nanomagnets and in a nanomagnetic NAND gate. Specific design of a NAND gate that is amenable to clocking with a SAW is discussed.

Finally, a comparison of single-domain (or macro-spin) LLG analysis with modified OOMMF based models that allow incoherent switching has been performed to get a preliminary idea of the possible extent of deviation of magnetization dynamics from the macro-spin approximation. In the chapter 7, a paradigm for creating nanomagnets with higher states (2 bits) is discussed and simulated. Such nanomagnets may be implemented by shape engineering. Two different shapes has been studied to understand the effect of geometry on coherent switching in 4-state nanomagnets. It is reported that concave magnets may be considered as a good option for implementing four-state nanomagnetic memory and logic.

Chapter 8 discusses the conclusion drawn from this study and future work .

Chapter 2

Magnetization dynamics and theory of multiferroic nanomagnetic logic

2.1 Introduction

The scale dependent magnetic behavior arises from the effect of several interactions that are present in magnetic materials, mainly (i) exchange coupling between spins that leads domains (ii) magneto-crystalline anisotropy due to spin orbit interaction that creates a preferred orientation for spins with respect to the crystallographic directions (iii) dipole (magneto-static) interaction between spins that leads to shape anisotropy. Furthermore, in magnetostrictive materials a fourth interaction known as the magnetoelastic or stress anisotropy arises that couples the stress/strain in the lattice to the magnetization orientation. This chapter develops a theory for the magnetization dynamics in shape-anisotropic (elliptical) magnetostrictive nanomagnets under application of stress and dipole coupling with neighboring elements. This is applied to study straintronic multiferroic nanomagnetic logic (SML) in this dissertation.

It is important to note (as explained in the introduction) that large magnetic samples (lateral dimensions > 1 micron) are usually found to have complex domain structures. However, in magnets with lateral dimensions ~ 100 nm (as studied in this thesis) the predominant magnetic structure is a single domain state [25] and can hence be studied using a macro-spin approximation. Questions do arise that while the final equilibrium states are single-domain the non-equilibrium switching process under the action of a stress pulse may proceed through metastable non single-domain states. This will be clarified (see summary and future work) by comparing the single

domain simulations with OOMMF [26] simulations that allow spatial variation in magnetization direction within a nanomagnet.

2.2 The fundamental concepts.

Some important parameters that characterize the magnetic behavior are[27]:

1. The magnetization $\vec{M}$, defined as the combination of magnetic moments divided by the volume(Ω) of magnetic structure:

$$\vec{M} = \frac{\sum \mu}{\Omega} \tag{2.1}$$

where Ω is the volume of any nanomagnet (only that of the magnetostrictive layer) and μ is magnetic moment and the magnetization (M) in the SI units is A/m.

2. The magnetic susceptibility χ , can be introduces as the magnetization divided by the absolute value of the magnetic field:

$$\chi = \frac{\left|\vec{M}\right|}{\left|\vec{H}\right|} \tag{2.2}$$

This scalar definition is true for isotropic materials, for general magnetic materials the susceptibility is a rank 2 tensor.

3. In the materials with spontaneous magnetic order, the ordering temperatures are the highest temperatures at which this order is still remained. These are the Curie temperature (T_C) for ferromagnets and the Neel temperature (T_N) for antiferromagnets and ferrimagnets.

4. The magnetic permeability μ , defined as:

$$\mu = \frac{\left|\vec{\mathbf{B}}\right|}{\left|\vec{H}\right|} \tag{2.3}$$

Where $\vec{B}$ is the magnetic induction or magnetic flux density or simply $\vec{B}$ field; μ is measured in Henry per meter (SI) and H is the magnetic field. The magnetic induction in matter depends on the magnetic field intensity $\vec{H}$ and the magnetization $\vec{M}$, and is given by :

$$\vec{B} = \mu_0(\vec{H} + \vec{M}) \tag{2.4}$$

Where $\mu_0 = 4\pi \times 10^{-7} (H/m \text{ or } \mathrm{N/A^2})$ is the permeability in vacuum.

2.3 **Exchange coupling energy**

The exchange coupling energy is the interaction responsible for the establishment of magnetic order in magnetic materials. This interaction originates from a quantum effect. The exchange interaction between two spins S_i and $\mathrm{S_j}$ can be described by the Hamiltonian [27].

$$H = -2\xi \vec{S}_i.\vec{S}_j \tag{2.5}$$

Where ξ is the exchange constant, which it is a measure of the intensity of this interaction. This is known as the Heisenberg Hamiltonian, and is widely used for the description of many magnetic properties of materials.

In the classical description, the energy of a pair of spins is:

$$E_{ex} = -2\,\xi\,\vec{\mathrm{S}}_\mathrm{i}.\vec{S}_j \tag{2.6}$$

The exchange energy can also be written as:

$$E_{ex} = -2\,\xi\,\vec{\mathrm{S}}_\mathrm{i}.\vec{S}_j = -2\,\xi\,\mathrm{S}^2\vec{m}_i.\vec{m}_j \tag{2.7}$$

Where the reduced magnetization can be defined as:

$$\vec{m} = \frac{\vec{M}}{\left|\vec{M}\right|} = \frac{\vec{M}}{M_s} \tag{2.8}$$

M_s is the maximum saturation magnetization and "m" is cosine direction of magnetization vector and $|m| = 1$.

If the angle between the two spins or moments of i and j is $\theta(i, j) = \Delta\theta$.

Therefore, for small $\Delta\theta_{i,j}$, $\left|\Delta\theta_{ij}\right| = \left|\vec{m}_i - \vec{m}_j\right|$. considering that one can introduce a continuous function $\vec{m}$, such that $\vec{m}$ is developed around $\vec{r}_j$, the vector of lattice site j as:

$$\vec{m}_j - \vec{m}_i = (\vec{r}_j.\nabla)m \tag{2.9}$$

where ∇ is the gradient operator and

$$\vec{r}_j = x_j\hat{i} + y_j\hat{j} + z_j\hat{k} \tag{2.10}$$

Therefore, from equation (2.7)

$$E_{ex} = -2\,\xi\,\mathrm{S}^2\cos(\Delta\theta) \cong \xi\,S^2(\Delta\theta)^2 \tag{2.11}$$

By replacing equation 2.9 in equation 2.11, we have :

$$E_{ex} = \xi\,\mathrm{S}^2((\vec{r}_j.\nabla)m)^2 = \xi\,\mathrm{S}^2[(\vec{r}_j.\vec{\nabla}m_x)^2 + (\vec{r}_j.\vec{\nabla}m_y)^2 + (\vec{r}_j.\vec{\nabla}m_z)^2] \tag{2.12}$$

The equation (2.12) is the exchange energy part of the total energy. One must integrate or sum over j and divide by two to avoid counting the contribution of the pairs of spins twice. In materials with cubic symmetry, the sum of the products of the coordinates of $\vec{r}$ is zero and $\sum_j x_j{}^2 = \frac{1}{3}\sum_j r_j^2$

The exchange energy per unit volume is found by dividing by $\Omega = a^3$ in the simple cubic case. In this case $\sum_j r_j^2 = 6a^2$ and we have:

$$\frac{E_{ex}}{\Omega} = \frac{\xi S^2}{a}[(\nabla m_x)^2 + (\nabla m_y)^2 + (\nabla m_z)^2] \quad (2.13)$$

The coefficient in equation (2.13) is the exchange stiffness constant **A**, proportional to the exchange constant ξ and measured in J/m .

$$A = \frac{n\xi S^2}{a} \quad (2.14)$$

n =1 for a simple cubic lattice, 2 for a bcc lattice and 4 for a fcc lattice.

NOTE: This stiffness term is not used in most simulations in this thesis as we assume that for small volumes (~100 nm × 100 nm × 10) considered the exchange coupling is so strong that the spins switch coherently. The only exception (where this term is used) is for the OOMMF [26] simulations.

2.4 Magnetostatic shape energy

The magnetostatic shape energy is the magnetic energy of a sample in its own magnetic field. This field is the demagnetization or demagnetizing field H_d , the magnetic field arising from the fact that the divergence of the total magnetic induction is zero. Maxwell's equation states that $\nabla.\vec{B} = \nabla.\mu_0(\vec{H} + \vec{M}) = 0$.

Therefore[27]:

$$\nabla.\vec{H}_d = -\nabla.\vec{M} \quad (2.15)$$

The magnetostatic energy E_{ms} , given by the energy of magnetization in the demagnetizing field is:

$$E_{ms} = -\frac{1}{2}\mu_0 \int_{\Omega} \vec{H}_d.\vec{M} \; d\Omega \quad (2.16)$$

Where the integral is performed over V, the volume of the sample. The factor ½ accounts for the fact that this energy term, also called magnetic self-energy, arises from the integration of the magnetization with the magnetic field that it creates.

The magnetostatic energy of samples of ellipsoid shape is simple to calculate[22] since the magnetic field is the same at every point of sample. The demagnetizing field is $\vec{H}_d$.

$$\vec{H}_d = -N_d \vec{M} \tag{2.17}$$

Where N_d is the demagnetizing factor and depends on the sample shape. It should be noted that if the nanomagnets have a non-ellipsoidal shape, the demagnetizing field is not constant throughout the volume.

The magnetostatic energy of an ellipsoid nanomagnet given by equation 2.16, in terms of the demagnetizing factors N_i and the components of magnetization $\vec{M}_i$ along the axes a, b and c is :

$$E_{ms} = -\frac{1}{2}\mu_0 \Omega (N_a M_a^2 + N_b M_b^2 + N_c M_c^2) \tag{2.18}$$

Where $N_a + N_b + N_c = 1$ (2.19)

And a, b and c refer to X, Y and Z direction in the Cartesian coordinate system.

The equation (2.18) can be simplified in the case of ellipsoid to:

$$E_{ms} = \frac{1}{2}\mu_0 M_S^2 \Omega (N_{d-xx} m_x^2 + N_{d-yy} m_y^2 + N_{d-zz} m_z^2) \tag{2.20}$$

Where :

$$m_x^2 + m_y^2 + m_z^2 = 1 \tag{2.21}$$

Therefore, we can simplify equation (2.21) by normalizing the magnetization with respect to azimutal and polar angle with M_S (a conserved quantity for a single-domain magnetostrictive

layer at a constant temperature). The figure 2.1 shows the multiferroic nanomagnet being considered.

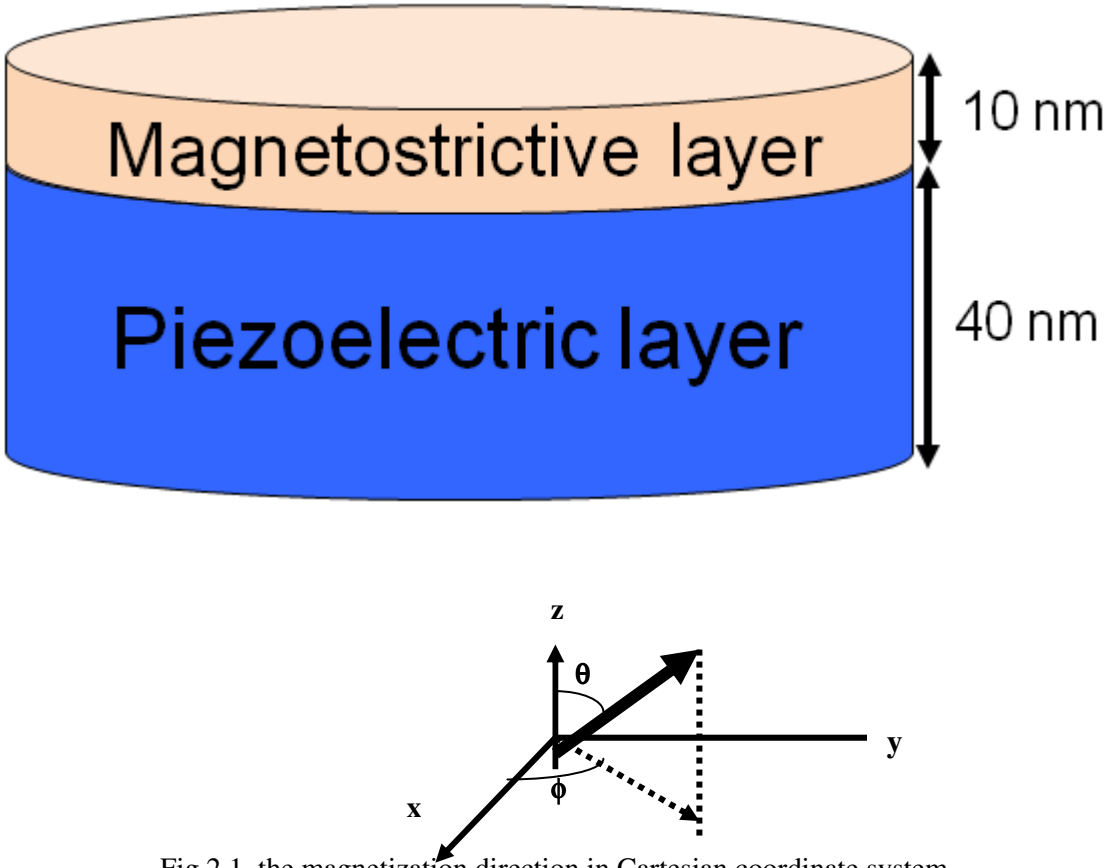

Fig 2.1. the magnetization direction in Cartesian coordinate system.

In this work, we consider the magnetostrictive layer as an ellipsoid whose major and minor axes diameters are **a** and **b** and its thickness is **t**. The demagnetization factors are:

$$N_{d\_yy} = \frac{\pi}{4}\left(\frac{t}{a}\right)\left[1-\frac{1}{4}\left(\frac{a-b}{a}\right)-\frac{3}{16}\left(\frac{a-b}{a}\right)^2\right]$$
$$N_{d\_xx} = \frac{\pi}{4}\left(\frac{t}{a}\right)\left[1+\frac{5}{4}\left(\frac{a-b}{a}\right)+\frac{21}{16}\left(\frac{a-b}{a}\right)^2\right]$$
$$N_{d\_zz} = 1-\frac{\pi}{4}(\frac{t}{a})\left[2+\left(\frac{a-b}{a}\right)+\frac{18}{16}\left(\frac{a-b}{a}\right)^2\right] \quad (2.22)$$

The equation 2.18 (for the nanomagnet in Fig 2.1) can be written as:

$$E_{ms} = -\frac{1}{2}\mu_0 \Omega M_S^2 (N_{d-XX}(\sin(\theta)\cos(\varphi))^2 + N_{d-yy}(\sin(\theta)\sin(\varphi))^2 + Nd_{d-zz}(\cos(\theta))^2) \quad (2.23)$$

Where the N_{d_xx}, N_{d_yy} and N_{d_zz} are given by equation 2.22.

The equation 2.23 represents magnetostatic energy of a single-domain nanomagnet.

2.5 Magnetoelastic energy (stress anisotropy)

The magnetoelastic energy of a magnetostrictive material has an improvement originating from the interaction between the magnetization and the strain ε_{ij} or mechanical stress σ. The magnetoelastic energy is the increase in anisotropy energy of a magnetic solid subjected to a stress. Its expression for a cubic crystal is given by [22]:

$$E_{me} = \oint [C_1(\alpha_1^2\varepsilon_{xx} + \alpha_2^2\varepsilon_{yy+}\alpha_3^2\varepsilon_{zz}) + C_2(\alpha_1\alpha_2\varepsilon_{xy} + \alpha_2\alpha_3\varepsilon_{yz} + \alpha_3\alpha_1\varepsilon_{zx})]\, d\Omega \quad (2.24)$$

The C-factors are the magnetoelastic coupling constants and α_i are the direction cosines.

Magnetostriction is the change in dimensions of a solid when subjected to a change in its magnetic state. It is measured by the relative linear deformation (strain) ε :

$$\varepsilon = \frac{\delta d}{d_0} \quad (2.25)$$

Where $\delta d = d - d_0$ is the change in linear dimension of the solid due to change in magnetization. The saturation magnetostriction λ_S is related to the strain generated when the magnetization is

changed from saturation magnetization in a perpendicular direction to saturation magnetization along a given direction. In the case of stress σ , the stress anisotropy energy E_{me} is given by:

$$E_{me} = \iiint \frac{3}{2} \lambda_S \sigma \alpha_i d\Omega \tag{2.26}$$

The α_i is defined as cosine direction of the applied stress.

2.6 Dipole coupling energy

Consider Fig.2.2 , with two adjacent multiferroic elements in the chain labeled as the i_{th} and j_{th} element.

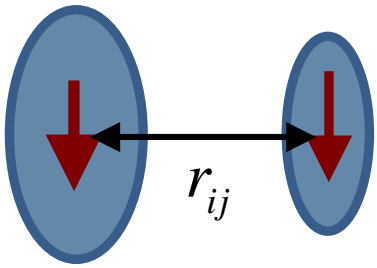

Fig 2.2 a dipole-coupled nanomagnet with r_{ij} separation between them.

These magnets have magnetizations that subtend polar and azimutal angles of θ_i, ϕ_i and θ_j, ϕ_j , respectively, with the positive Z direction and direction of the X-Y plane.

The dipole-dipole interaction energy is [22]:

$$E^{i-j}_{dipole-dipole} = \frac{\mu_0 M_S^2 \Omega_i \Omega_j}{4\pi \left|\vec{r}_{i-j}\right|^3} [(\vec{m}_i(t).\vec{m}_j(t)) - \frac{3}{\left|\vec{r}_{i-j}\right|^2} (\vec{m}_i(t).\vec{r}_{i-j})(\vec{m}_j(t).\vec{r}_{i-j})] \tag{2.27}$$

Where $\vec{r}_{i-j}$ is the vector distance between the i_{th} and j_{th} magnet and $\vec{m}_K$ is the magnetization of the K_{th} magnet normalized to M_S .For two neighboring magnets whose in-plane hard axes are

collinear with the line joining their centers, the dipole coupling energy of i_{th} magnet due to its dipole interaction with j_{th} neighbors is:

$$\sum_{j\neq i} E^{i-j}_{dipole-dipole}(t) = \frac{\mu_0 M_s^2 \Omega^2}{4\pi r^3} \sum_{j\neq i} \begin{bmatrix} -2\left(\sin\theta_i(t)\cos\phi_i(t)\right)\left(\sin\theta_j(t)\cos\phi_j(t)\right) \\ +\left(\sin\theta(t)_i \sin\phi_i(t)\right)\left(\sin\theta_j(t)\sin\phi_j(t)\right) \\ +\cos\theta_i(t)\cos\theta_j(t) \end{bmatrix} \quad (2.28)$$

If the line joining the centers subtends an angle γ with their hard axes as shown in the Figure 2.3, the dipole coupling energy is:

$$\sum_{j\neq i} E^{i-j}_{dipole-dipole}(t) = \frac{\mu_0 M_s^2 \Omega^2}{4\pi r^3} \sum_{j\neq i} \begin{bmatrix} \left(\sin\theta_i(t)\cos\phi_i(t)\right)\left(\sin\theta_j(t)\cos\phi_j(t)\right)\left(-2(\cos\gamma)^2+(\sin\gamma)^2\right) \\ +\left(\sin\theta_i(t)\sin\phi_i(t)\right)\left(\sin\theta_j(t)\sin\phi_j(t)\right)\left(-2(\sin\gamma)^2+(\cos\gamma)^2\right) \\ +\left\{\left(\sin\theta_i(t)\cos\phi_i(t)\right)\left(\sin\theta_j(t)\sin\phi_j(t)\right)+\left(\sin\theta_j(t)\cos\phi_j(t)\right)\left(\sin\theta_i(t)\sin\phi_i(t)\right)\right\} \\ \times\left(-3\sin\gamma\cos\gamma\right)+\cos\theta_i(t)\cos\theta_j(t) \end{bmatrix} \quad (2.29)$$

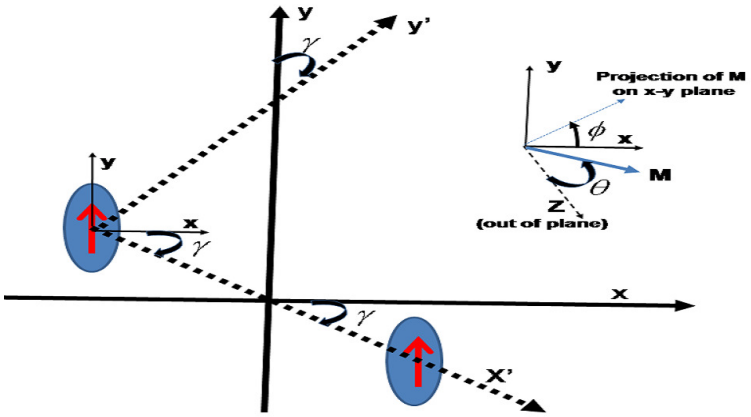

Fig 2.3 .Two nanomagnets whose hard axes are at an angle γ to the line joining their centers.

2.7Energy terms in nanomagnetic structures.

For studying the behavior of a nanomagnet, it is necessary to consider the relevant energy terms such as the exchange energy, magnetocrystalline and stress anisotropy, dipole coupling, external magnetic field and thermal noise.

The total energy is

$$U_i(t) = E_{ex} + E_{magnetostatic} + E_{magnetocrystalline} + E_{stress-anisotropy} + E_{ext\text{-}field} + E_{dipole-dipole} + E_{thermal} \quad (2.30)$$

In this research, the magnetocrystalline anisotropy is neglected as the sample is assumed to have random polycrystalline orientation. Further, the exchange coupling energy is not explicitly added as it is assumed that this term is strong enough to produce a coherent rotation of magnetization. This is the reason macro-spin approximation is used. The equation can be written as:

$$U_i(t) = \underbrace{+\left(\frac{\mu_0}{2}\right)\left[M_s^2\Omega\right]\left(N_{d\_xx}\left[\sin\theta_i(t)\cos\phi_i(t)\right]^2 + N_{d\_yy}\left[\sin\theta_i(t)\sin\phi(t)_i\right]^2 + N_{d\_zz}\left[\cos\theta_i(t)\right]^2\right)}_{E_{shape-anisotropy}\,(OR\ \text{magneto-static energy})}$$
$$\underbrace{-\left(\frac{3}{2}\lambda_s\sigma_i\Omega\right)\sin^2\theta_i(t)\sin^2\phi_i(t)}_{E_{stress-anisotropy}} \underbrace{-\mu_0\Omega\vec{M}.\vec{H}_{ext}}_{E_{external-magnetic\ \text{field}}} + \underbrace{\sum_{j\neq i} E^{i-j}_{dipole-dipole}(t)}_{E_{dipole}} \underbrace{+E_{thermal}}_{E_{Thermal\ \text{Noise}}} \quad (2.31)$$

To minimization of the energy functional leads to the situation that $\vec{M}(\vec{r})$ has to eventually be parallel to the effective magnetic field acting at the point $\vec{r}$.

It should be considered that this effective field $\vec{H}_{eff}$ exerts a torque on the magnetization of each magnet. If the direction of this field be parallel to magnetization, the exerted torque has zero effect on magnetization as it is already in the minimum energy state.

$$\vec{m}\times\vec{H}_{eff} = 0 \quad (2.32)$$

The effective field $\vec{H}_{eff}$ acting on $\vec{M}(\vec{r})$ is obtained by taking partial derivation of the total energy with respect of the magnetization vector [28], and is given by:

$$\vec{H}_{eff}^{\,i}(t) = -\frac{1}{\mu_0 \Omega}\frac{\partial U_i(t)}{\partial \vec{M}_i(t)} = -\frac{1}{\mu_0 M_s \Omega}\nabla_{\vec{m}} U_i(t) \tag{2.33}$$

From equation.2.31 in equation 2.33, we have:

$$\vec{H}_{eff} = \vec{H}_{Magnetostatic} + \vec{H}_{Stress-Anisotropy} + \vec{H}_{external} + \vec{H}_{dipole} + \vec{H}_{Thermal} \tag{2.34}$$

In the Cartesian coordinate system this turns out to be:

$$\begin{aligned}
H^i_{eff-x}(t) &= \sum_{j\neq i} -\frac{1}{\mu_0 M_s \Omega}\frac{\partial E^{i-j}_{dipole-dipole}(t)}{\partial m_x(t)} - M_s\left(N_{d-xx}\right)\sin\theta_i(t)\cos\phi_i(t) + H_{X-Thermal} \\
H^i_{eff-y}(t) &= \sum_{j\neq i} -\frac{1}{\mu_0 M_s \Omega}\frac{\partial E^{i-j}_{dipole-dipole}(t)}{\partial m_y(t)} - M_s\left(N_{d-yy}\right)\sin\theta_i(t)\sin\phi_i(t) + \left(\frac{3}{\mu_0 M_s}\lambda_s\right)\sigma_i(t)\sin\theta_i(t)\sin\phi_i(t) + H_{bias} + H_{Y-Thermal} \\
H^i_{eff-z}(t) &= \sum_{j\neq i} -\frac{1}{\mu_0 M_s \Omega}\frac{\partial E^{i-j}_{dipole-dipole}(t)}{\partial m_z(t)} - M_s\left(N_{d-zz}\right)\cos\theta_i(t) + H_{Z-Thermal}
\end{aligned} \tag{2.35}$$

The effect of thermal fluctuation is modeled with a random field ($\vec{H}_{Thermal}$) in the manner of [29-31]. The field $\vec{H}_{Thermal}$ has the following statistical properties:

$$< \vec{H}_{Thermal}(t) >= 0 \tag{2.36}$$

$$< \vec{H}^i_{Thermal}(t)\vec{H}^j_{Thermal}(t') >= \delta_{ij}\delta(t-t')(VAR)^2 \tag{2.37}$$

$$VAR = \sqrt{\frac{2K_B T\alpha}{\mu_0 M_s \gamma \Omega \Delta t}} \tag{2.38}$$

Thus, the effective magnetic field due to thermal noise is modeled as:

$$\vec{H}_{ThermalNoise} = \sqrt{\frac{2K_B T\alpha}{\mu_0 M_s \gamma \Omega \Delta t}}(\vec{G}(t)) \tag{2.39}$$

where $\vec{G}(t)$ is a Gaussian random distribution with mean of 0 and variance of 1 in each Cartesian coordinate axis; Δt is time step at simulation and is proportional to the inverse of the attempt frequency with which thermal noise perturbs the magnetization; and K_B is the Boltzmann constant.

2.8 Magnetization dynamics and Landau-Lifshitz-Gilbert (LLG) equation.

The equation for dynamics of the magnetization $\vec{M}$ in an applied effective magnetic field is determined by the fact that the electrons, responsible for the magnetism of the atoms have angular momentum. Their magnetization $\vec{M}$ precesses in an applied effective magnetic field, and the torque exerted by this field is :

$$\tau = -\gamma_e \vec{M} \times \mu_0 \vec{H}_{eff} \tag{2.40}$$

Where γ_e is the electron gyromagnetic ratio. Thus, the equation of motion for the magnetization, in the absence of damping is given by:

$$\frac{d\vec{M}(t)}{dt} = -\gamma_e \vec{M}(t) \times \mu_0 \vec{H}_{eff}(t) = -\gamma_G \vec{M}(t) \times \vec{H}_{eff}(t) \tag{2.41}$$

The constant γ_G is the gyromagnetic ratio and proportional to the electron gyromagnetic ratio γ_e. The latter in the SI system of units is given by $\gamma_e = \frac{2\mu_e}{\hbar} = 1.760 \times 10^{11} s^{-1} T^{-1}$. The Gilbert gyromagnetic ratio is therefore:

$$\gamma_G = \mu_0 \gamma_e = 2.2127606 \times 10^5 \, mA^{-1} s^{-1} \tag{2.42}$$

The equation 2.41 just describes a motion of precession of $\vec{M}$ around the direction of $\vec{H}_{eff}$. To correctly model the magnetization dynamics, the damping term should be included to the equation (2.41), therefore; The magnetization dynamics of any nanomagnet under the influence of an effective field $\vec{H}_{eff}$ acting on it is described by the vector Landau-Lifshitz-Gilbert (LLG) equation [28]:

$$\frac{d\vec{M}(t)}{dt} = -\gamma \vec{M}(t) \times \vec{H}_{eff}(t) - \frac{\alpha\gamma}{M_s}\left[\vec{M}(t) \times \left(\vec{M}(t) \times \vec{H}_{eff}(t)\right)\right] \tag{2.43}$$

M_s is the saturation magnetization of the magnetostrictive layer and α is the Gilbert damping factor [32] associated with internal dissipation in the magnet when its magnetization rotates. We can simplify equation (2.43) by normalizing the magnetization with respect to M_s(saturation magnetization) which is a conserved quantity (constant) for a single domain magnetostrictive layer at a constant temperature.

This yields:

$$\vec{m} = \frac{\vec{M}}{M_s};\ m_x^2 + m_y^2 + m_z^2 = 1. \tag{2.44}$$

Here, m_x, m_y and m_z are respectively the *x*-, *y*- and *z*-components of the normalized magnetization vector $\vec{m}$. Thus, in terms of the individual components in Cartesian coordinates system, equation 2.43 becomes:

$$\frac{dm_x(t)}{dt} = -\gamma\left(H_{eff-z}(t)m_y(t) - H_{eff-y}(t)m_z(t)\right) - \alpha\gamma\left(H_{eff-y}(t)m_x(t)m_y(t) - H_{eff-x}(t)m_y^2(t) - H_{eff-x}(t)m_z^2(t) + H_{eff-z}(t)m_x(t)m_z(t)\right)$$

$$\frac{dm_y(t)}{dt} = -\gamma\left(H_{eff-x}(t)m_z(t) - H_{eff-z}(t)m_x(t)\right) - \alpha\gamma\left(H_{eff-z}(t)m_y(t)m_z(t) - H_{eff-y}(t)m_z^2(t) - H_{eff-y}(t)m_x^2(t) + H_{eff-x}(t)m_x(t)m_y(t)\right) \quad (2.45)$$

$$\frac{dm_z(t)}{dt} = -\gamma\left(H_{eff-y}(t)m_x(t) - H_{eff-x}(t)m_y(t)\right) - \alpha\gamma\left(H_{eff-x}(t)m_z(t)m_x(t) - H_{eff-z}(t)m_x^2(t) - H_{eff-z}(t)m_y^2(t) + H_{eff-y}(t)m_y(t)m_z(t)\right)$$

Where H_{eff-j} is the *j*-th component of $\vec{H}_{eff}$.

The Landau-Lifshitz-Gilbert (LLG) equation allows one to describe how the magnetization evolves with time. The time evolution of the magnetization of the nanomagnet is given by solving a set of coupled LLG equations of equation.2.45. The solution of the LLG equation is carried out numerically. In this work, both Runge-Kutta and Euler method are used to solve this coupled nonlinear ODE equation.

It should be Noted that $m_x(t)$, $m_y(t)$ and $m_z(t)$ are not independent of each other as they are related through equation (2.44) and we can use the parametric representation:

$$m_x(t) = \sin\theta(t)\cos\phi(t)\ ;\ m_y(t) = \sin\theta(t)\sin\phi(t)\ ;\ \mathrm{m}_z(t) = \cos\theta(t) \quad (2.46)$$

This simplifies equation (2.45) to two coupled equations for the magnetization orientation θ_i , ϕ_i for the *i*-th nanomagnet:

$$\frac{dm_x^i(t)}{dt}=\cos\phi_i(t)\cos\theta_i(t)\frac{d\theta_i(t)}{dt}-\sin\theta_i(t)\sin\phi_i(t)\frac{d\phi_i(t)}{dt}=\gamma(H^i_{eff-z}(\sin\theta_i(t)\sin\phi_i(t))-H^i_{eff-y}\cos\theta_i(t))-$$
$$\alpha\gamma(H^i_{eff-y}(\sin\theta_i(t)\cos\phi_i(t))(\sin\theta_i(t)\sin\phi_i(t))-H^i_{eff-x}(\sin\theta_i(t)\sin\phi_i(t))^2-H^i_{eff-x}(\cos\theta_i(t))^2+$$
$$H^i_{eff-z}(\sin\theta_i(t)\cos\phi_i(t))(\cos\theta_i(t))$$
$$\frac{dm_y^i(t)}{dt}=\sin\phi_i(t)\cos\theta_i(t)\frac{d\theta_i(t)}{dt}+\sin\theta_i(t)\cos\phi_i(t)\frac{d\phi_i(t)}{dt}=\gamma(H^i_{eff-x}\cos\theta_i(t)-H^i_{eff-z}\sin\theta_i(t)\cos\phi_i(t))- \quad (2.47)$$
$$\alpha\gamma(H^i_{eff-z}(\sin\theta_i(t)\sin\phi_i(t))(\cos\theta_i(t))-H^i_{eff-y}(\cos\theta_i(t))^2-H^i_{eff-y}(\sin\theta_i(t)\cos\phi_i(t))^2+$$
$$H^i_{eff-x}(\sin\theta_i(t)\cos\phi_i(t))(\sin\theta_i(t)\sin\phi_i(t))$$

The above result show that there are two independent degrees of freedom θ_i , ϕ_i for each nanomagnet and they are influenced by their coupling to their neighboring nanomagnets whose magnetization orientations θ_j, ϕ_j that is accounted by the dipole contribution to the H_{eff} in equation(2.35).

2.9 Energy dissipation

The energy dissipated in flipping a bit has two components:

i) Energy dissipated while applying, reversing and removing a voltage on the piezoelectric layer for generating stress. This is the energy dissipated in the clocking circuit and is given by [6]:

$$E_{clock}=\frac{1}{2}CV^2\frac{\omega RC}{1+(\omega RC)^2} \quad (2.48)$$

where C is the capacitance of the piezoelectric layer, R is the resistance of the wires and V is the voltage applied across it. We assume that the voltage waveform is sinusoidal with a period $2\pi/\omega$. However, the problem with this RC circuit is that the $\frac{1}{2}(CV^2)$ energy stored in the capacitor (piezoelectric layer), when it is fully charged, minus the dissipation in the resistor, will be dissipated in the power source in each cycle. A better scheme is to use an LCR circuit where

energy is merely transferred between the capacitive and inductive elements and the only energy lost per cycle is the energy dissipated in the resistive element [6]. In such a clocking circuit, the energy dissipated is:

$$E_{clock} = \pi \frac{V^2}{R} \omega (RC)^2 \tag{2.49}$$

ii) Internal energy dissipated in the magnet during magnetization rotation [28]. This energy E_d is calculated as:

$$\frac{dE_d(t)}{dt} = -\mu_0 \int_{\Omega} \vec{H}_{eff} . \frac{d\vec{M}}{dt} \, d\Omega \tag{2.50}$$

By substituting equation (2.43) for $\frac{d\vec{M}}{dt}$ in equation (2.50) and integrating one obtains:

$$E_d(\tau) = \int_0^{\tau} -\left(\frac{dE_d}{dt} \right) dt = \int_0^{\tau} \frac{\alpha \mu_0 \nu \Omega}{(1+\alpha^2) M_s} | \vec{H}_{eff}(t) \times \vec{M}(t) |^2 \, dt \tag{2.51}$$

This expression clearly shows that this dissipation is associated with damping in the magnet because it disappears when $\alpha = 0$.

Chapter 3

Bennett clocking with strain in multiferroic nanomagnets for unidirectional logic propagation in a nanomagnetic “wire” and a universal logic (NAND) gate

The multiferroic nanomagnetic logic element, consisting of a magnetostrictive layer elastically coupled to a piezoelectric layer, implements unidirectional propagation of information using nearest-neighbor dipole field coupling between neighboring nanomagnets while being clocked by a "stress cycle" that lowers and restores the shape anisotropy barrier. The nanomagnets are designed to be elliptical to provide enough uniaxial shape anisotropy to be stable against switching spontaneously under thermal noise. These nanomagnets have bistable magnetization orientation and prefer to be magnetized up ”1” or down “0”. Thus, this bistability provides the basis for encoding information in a nanomagnet based device.

In this chapter, we will discuss: (i) The static energy landscape of the multiferroic nanomagnetics. (ii) The magnetization dynamics of dipole coupled multiferroic nanomagnets in a logic "wire" in which individual nanomagnets are clocked (their magnetization can be rotated by a large angle) with a tiny voltage of few tens of mV applied to the piezoelectric layer). (iii) The switching dynamics of a multiferroic nanomagnetic NAND gate with fan-in/fan-out. While (i) involves plotting the energy profiles, (ii) and (iii) are simulated by solving the Landau-Lifshitz-Gilbert (LLG) equation while neglecting thermal noise.

3.1 The energy landscape and static behavior of nanomagnet

Before starting a study of the magnetization dynamics of the multiferroic nanomagnetic logic, it is necessary to understand the energy landscape (profile of energy vs. orientation of magnetization) of both single nanomagnet and dipole-coupled nanomagnets. The static energy profile of nanomagnets is essential to determine the effective field that drives the magnetization dynamics. We first study a single isolated nanomagnet and then extend our discussion to dipole-coupled nanomagnets.

Fig. 3.1 shows energy landscape of a single nanomagnet versus its in-plane angle φ (Deg). There are 2 minimum stable energy orientations at angles $\phi = -90^0 \ \& \ 90^0$, at which the nanomagnet naturally prefers to be directed and is stable while there is also a maximum energy level at $\varphi = 0^0 \ and \ 180^0$, at which the magnetization in the nanomagnet is unstable. These two stable directions are called "**Easy axis**" and the unstable direction is considered as "**Hard axis**". At the hard axis, the magnetization of nanomagnet is unstable and it would rather not be in this direction.

The difference in energy level between the hard axis and the easy axis of a nanomagnet is called "energy barrier of nanomagnet" and the clocking field (or stress in our case) is needed to remove this barrier. Thus, the nanomagnet should be designed to have sufficient energy barrier that the magnetization orientation is stabilized against the effect of thermal noise.

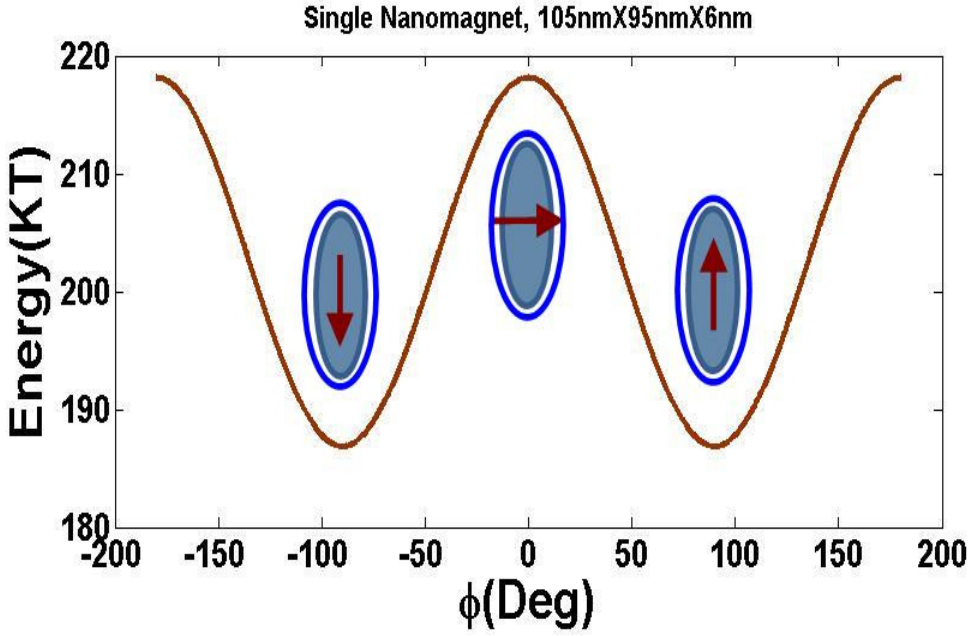

Fig 3.1. Energy Landscape of a single domain nanomagnet.

The energy barrier of a nanomagnet is similar to a wall, which resists changing the state of the magnetization in the nanomagnet. Therefore, it is necessary to apply an external field/stress to remove this barrier and allow magnet to start rotating. Figure.3.2 shows the energy barrier of a single domain nanomagnet.

The energy barrier of a nanomagnet can be calculated through the difference between two states of nanomagnet at $\phi = -90^0$ & 90^0 and $\phi = 0^0$. Equation 2.24 gives the total energy of a single nanomagnet. Therefore, by considering $\theta = 90^0$. We have:

$$E_b = E_{me}(\phi = -90 or 90, \theta = 90) - E_{me}(\phi = 0, \theta = 90) \quad (3.1)$$

For a nanomagnet with a=105nm ~ b=95nm~ t=6n, its energy barrier is about ~32(KT) ~0.75 eV, which is the energy that must be applied to lower this barrier and rotate the magnetization to the easy axis.

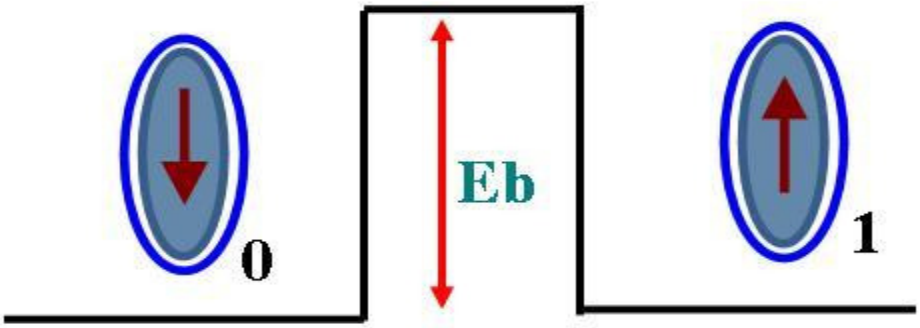

Fig 3.2. Energy barrier prediction for a single nanomagnet.

The dipole-coupled nanomagnet can be considered as 2 nearest nanomagnets so that the stray magnetic field affects the other. The initial orientation of these magnets and their magnetization direction has dominant influence on their magnetization dynamics under stress (when clocked)..

The figures 3.3 and 3.4 show energy landscape of a dipole-couple nanomagnet with $\gamma = 0^0$ (the angle between two magnets) and $\gamma = 90^0$. This implies that the nanomagnets position relative to each other plays an important role in behavior of dipole coupled nanomagnets. If the $\gamma = 0^0$ (the line joining the centers is coincides with the hard axis), they like to be anti-ferromagnetic. On the other hand, if the $\gamma = 90^0$ (the line joining the centers is coincides with the easy axis), they prefer to be ferromagnetic. These different configurations are useful for implementing the universal NAND logic gate.

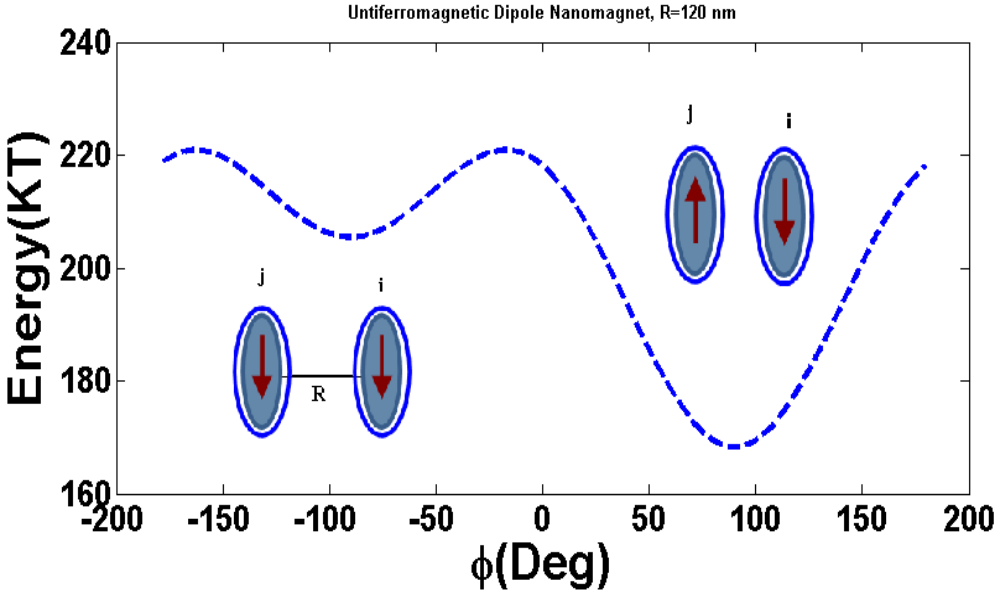

Fig 3.3. Energy landscape of an antiferromagnetic dipole nanomagnet.

For performing nanomagnetic computation or for propagation of nanomagnetic logic two things are essential: (i) Clocking field to remove the barrier and reset the nanomagnet and (ii) directed bias field during withdrawal of stress (dipole coupling). Fig 3.3, shows the dipole magnets has down direction and magnet j is considered as stiff magnet. Due to dipole coupling energy, the magnet i is under the effect of this additional field and prefers to be in the opposite direction. The dipole effect reduces the energy barrier of the magnet i and the minimum stress needed for rotating it should remove this reduced barrier.

The same scenario can be described for Fig 3.4, however in this configuration the nanomagnets would rather to be ferromagnetic and the effect of dipole coupling is about two times more than previous configuration.

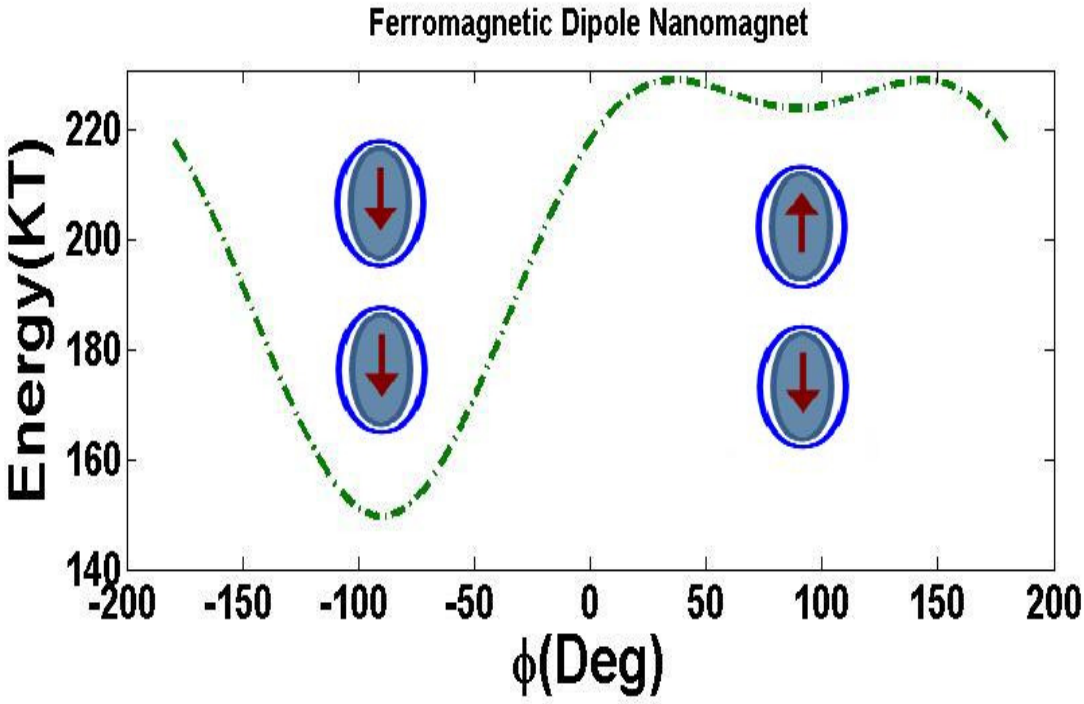

Fig 3.4. The energy configuration of a ferromagnetic dipole nanomagnet.

3.2 Critical stress

To start rotating a nanomagnet, it is typically necessary apply sufficient stress to beat the shape anisotropy barrier and rotate the magnet to its hard axis so the correct state under influence of nearest nanomagnet (dipole-coupling) can be achieved when this stress is withdrawn. So, it is interesting to know the minimum stress for starting the rotation of the nanomagnet in the absence of thermal noise. This minimum stress is known as the critical stress and when dipole coupling is not considered it is given by:

$$E_{Stress-anisotropy} = E_{Shape-anisotropy} \Rightarrow -\frac{3}{2}\lambda_S \sigma_{Critical}\Omega = [N_{d-xx} - N_{d-yy}](\mu_0/2)M_S^2\Omega \tag{3.2}$$

$$\sigma_{Critical} = \left| \frac{[N_{d-xx} - N_{d-yy}](\mu_0/2)M_S^2}{-\frac{3}{2}\lambda_S} \right|$$

3.3 The multiferroic nanomagnetic logic "wires".

To propagate a bit of information a nanomagnetic chain "wire" is needed. This is achieved by pattering a line of identical single domain nanomagnets next to a stiff input bit (a nanomagnet with higher energy barrier) and resetting them individually to have their magnetizations pointing along their hard axis. This is achieved with strain, which is generated in the PZT layer upon applying an electrostatic potential across it. This strain is elastically transferred to the magnetostrictive layer and rotates its magnetization by ~ 90^0 to implement Bennett clocking in nanomagnetic logic chains. Due to the small voltage needed, this clocking method is far more energy-efficient than those that would employ spin transfer torque or magnetic fields to rotate the magnetization. In order to assess if such a clocking scheme can be also reasonably fast, we have studied the magnetization dynamics of a multiferroic logic chain and universal NAND gate with nearest neighbor dipole coupling using the Landau-Lifshitz-Gilbert (LLG) equation in this chapter.

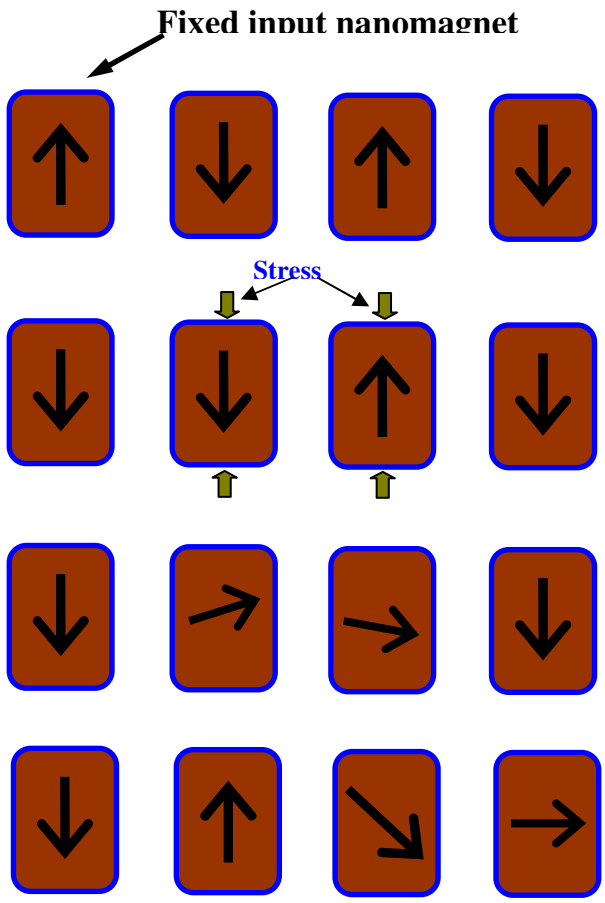

Fig 3.5. A schematic showing how a magnetic chain can be used to transfer information from input to another point and propagate a logic bit through a chain of four dipole coupled multiferroic nanomagnets with Bennett clocking implemented with stress. (First row) a chain of elliptical nanomagnets in the ground state with magnetization orientation indicated by arrows. (Second row) Magnetization of the first magnet is flipped with an external agent and the second magnet finds itself in a tied state where it experiences no net dipole interaction. (Third row) The second and the third magnet are subjected to electrically induced stresses that rotate their magnetizations close to the hard axis. (Fourth row) The second magnet is freed from stress so that its magnetization relaxes to the easy axis as a result of shape anisotropy, and it switches to the desired "up" state rather than the incorrect "down" state since the dipole interaction from the left neighbor is now stronger than that from the right neighbor so that the tie is resolved.

We have used 4th order *Runge-Kutta* method to solve the system of coupled differential equations in Equations (2.45) and (2.47) for the linear chain of four coupled multiferroic elements shown in fig.3.6 The solution yields the orientation $\theta_i(t)$, $\phi_i(t)$ of the magnetization vector in any multiferroic element in the chain at any instant of time *t*.

In this study, we have assumed that the magnetostrictive layers are made of polycrystalline Terenol-D which has the following parameters: $(3/2)\lambda s=9\times10^{-4}$, M_s = 0.8×10^6A/m [22,33], and average Young's modulus $Y = 8\times10^{10}$ Pa [34]. We assume that the Gilbert damping constant for Terfenol-D is $\alpha = 0.1$ based on high $[\alpha > 0.1]$ values for heavier elements such as dysprosium [32]. The dimensions of each nanomagnet are ~ 101.75 nm × 98.25 nm × 10 nm and the center-to-center separation between neighboring elements (or pitch) is 200 nm. The above parameters were chosen to ensure that: (i) the shape anisotropy energy of the elements is sufficiently high (~0.8 eV or ~32*kT* at room temperature) so that the equilibrium bit error probability due to spontaneous magnetization flipping is very low ($\sim e^{-32} \approx 10^{-14}$), (ii) the dipole interaction energy is limited to 0.26 eV which is significantly lower than the shape anisotropy energy to prevent spontaneous flipping of magnetization, but is still large enough to ensure that the magnetization of the multiferroic elements always flips to the correct orientation when stress is released, even under the influence of random thermal fluctuations. We recognize however that quantifying the relationship between switching speed, temperature, dipole coupling and error probability is beyond the scope of this section since that would need solving the stochastic LLG equation [11] or Fokker-Plank equations [28].

In all our simulations, the initial magnetizations of the multiferroics always corresponds to the ground state of the array where the four magnetizations are anti-ferromagnetically ordered, i.e. each multiferroic magnetization is along the major axis (which is the easy axis) and nearest neighbors

have anti-parallel magnetizations as shown in the first row of Fig. 3.5 At time t = 0, the first multiferroic (far left) has its magnetization flipped abruptly (second row of Fig.3.5). We then consider the time evolutions of the magnetizations of every multiferroic nanomagnet in various cases when stress is applied to the second and third nanomagnets in arbitrary time sequences.

The maximum value of stress that we have considered is 40 MPa which can be generated by a voltage of ~ 200 mV applied across the PZT layer. We calculate this as follows: The PZT layer can transfer up to 500×10^{-6} strain to the Terfenol-D layer. This strain generates a stress of 40 MPa in the Terfenol-D layer, which is found by multiplying the strain with the average Young's modulus of Terfenol-D, assuming linearity. Since the piezoelectric coefficient of PZT $d_{31} \approx -10^{-10}$ m/V , the voltage required to induce this strain in the PZT layer that is 40 nm thick is 200 mV. The corresponding maximum stress-anisotropy energy is $\frac{3}{2}[\lambda_s \sigma \Omega]$ = 682kT, which is much more than the shape anisotropy energy barrier of 32 kT, and is therefore more than adequate to turn the magnetization to the hard axis from the easy axis. The excess energy of 650kT (682kT - 32kT) is consumed to speed up the rotation.

The local effective field on each nanomagnet $\vec{H}_{eff}(t)$ is calculated at each time step from Equation (2.33 , 2.35). We also assume that stress is applied instantaneously and removed instantaneously. The rationale for this assumption is that **t**he capacitance of a 40 nm-thick PZT layer of surface area 101.75 nm × 98.25 nm is 1.74 fF, if we assume the relative dielectric constant of PZT to be 1000. We also assume that the PZT layer is electrically accessed with a silver wire of resistivity ~2.6 μΩ-cm [36] so that an access line of length 10 μm and cross section 50 nm × 50 nm has resistance ~100 Ω. Therefore, the RC time constant associated with charging the capacitor is 0.174 picoseconds while the magnetization switching time is always more than 0.5 nanoseconds.

This allows us to consider the onset and removal of stress as instantaneous. Furthermore, the mechanical resonance frequency of such as system can be approximately calculated as $f = \frac{1}{4L}\sqrt{Y/\rho}$, where ρ is the density and L is the long dimension. Since, the PZT layer is much thicker than the Terfenol-D layer, we assume average ρ = 7,500 Kg/m^3 [37], average Young's modulus dominated by PZT is Y=60 GPa [37] and L~100 nm. Consequently, the resonance frequency turns out to be 7 GHz. We may be able to scale the size to L ~50 nm to increase the resonance frequency to ~ 14 GHz (that corresponds to a time period of 70 ps), which is shorter than 0.5 ns. Hence, it is a very good approximation to consider the stress to be applied instantaneously. This analysis shows that ultimately the Bennett clock rate of multiferroic logic is likely to be limited by the magnetic and then mechanical response of the structure! In this section, we discuss two illustrative cases, with the first case being the simplest, in which the logic chain in fig.3.6 is Bennett clocked by applying only compressive stress of 5.2 MPa to the second and third nanomagnets. The voltage required to generate this stress is 26 mV (the voltage scales linearly with stress; hence, if 200 mV generates 40 MPa, then 26 mV will generate 5.2 MPa).

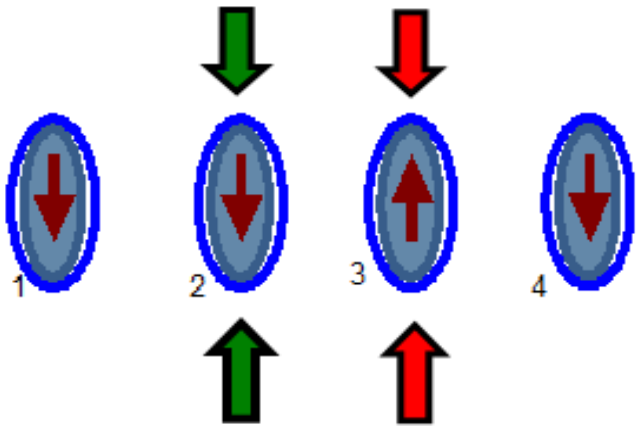

Fig 3.6.The second and third nanomagnet is stressed simultaneously.

The second and third nanomagnets are stressed instantaneously at times t = 0 and t = 0.02 ns respectively, assuming that the first nanomagnet's magnetization has been flipped by some external agent at t = 0 to provide input data to the chain. Once stress has rotated the second and third nanomagnets' magnetizations by nearly 90^0 (i.e. their projections on the plane of the magnets have undergone a 90^0 rotation to align along the common hard axis), it is removed abruptly from the second nanomagnet while still being held constant on the third. The relaxed second nanomagnet then gradually settles down to the correct magnetization state anti-parallel to that of the first because of the influence of its shape anisotropy and dipole interaction from its neighbors. This is shown in the fourth row of Fig. 3.5. The input bit, provided to the first nanomagnet, has now successfully propagated to the second, which means that Bennett clocking has been successfully implemented.

The simulation result in Fig.3.7 shows that complete switching of the second multiferroic's magnetization vector (from "down" to "up") takes ~ 1 ns. Note that the switching corresponds to the azimuthal angle ϕ_2 of the second magnet changing from -90^0 to + 70^0. After the second nanomagnet has switched, we can release the stress on the third. Therefore, the stress on the third magnet needs to be maintained for a total duration of ~ 1 ns, which means that the maximum clock rate achievable in this case is 1/(1 ns) = 1 GHz.

In the second case, we apply a larger 40 MPa compressive stress on the second and third multiferroics until their magnetizations align along the hard axis (i.e. ϕ_2 becomes 0^0). We then reverse the stress on the second multiferroic from compressive to tensile, which aids it to relax faster from the hard axis to the easy axis. As a result, the total switching time to switch the second multiferroic's magnetization vector reduces to ~ 0.5 ns as can be seen in Fig.3.10. However, in this

case, the high stress causes significant "out of plane" excursion of the magnetization vector. We discuss the two cases below.

3.3.1 Case 1: Compressive stress of 5.2 MPa is applied instantaneously on multiferroic nanomagnets 2 and 3 by applying a potential of 26 mV, followed by instantaneous removal of stress from multiferroic nanomagnet 2 after its magnetization aligns close to the in-plane hard axis.

We apply a compressive stress of 5.2 MPa on the second and third multiferroic nanomagnets as a step function in time at t=0 and t=0.02 ns respectively. Since, Terfenol-D has positive magnetostriction, this tends to rotate their magnetizations to a direction perpendicular to the direction of the applied stress. It should be noted that we assume that both magnetization orientations rotate to the right to simplify the numerical analysis. The analysis would be identical if both magnetizations rotated to the left, because of the symmetry. By "phasing" our clock so that stress is applied on the second nanomagnet slightly before it is applied on the third, we ensure that the x-component of $\vec{H}_{dipole}$ due to the initial rotation of the second nanomagnet favors lining up the third nanomagnet's magnetization in the same direction (parallel). Ultimately, the second magnet's magnetization turns anti clockwise from $\phi_2 = -90^o$ to nearly 0^o and third multiferroic's magnetization rotates clockwise from $\phi_3 = +90^o$ to nearly 0^o, so that they both align close to the hard axis and are mutually parallel. As shown in Fig 3.7, the time taken for this 90^o rotation to occur, which orients the second and third multiferroics along the hard axis, is ~0.4 ns. At this point, the nearest-neighbor dipole coupling makes the first and fourth multiferroics' magnetizations rotate slightly away from the "down" orientation to the "down and slightly right" orientation so that

their orientations are $\phi_1 \approx -82^0$, $\phi_4 \approx -66^0$. This is shown in Fig. 3.7 These peripheral multiferroic elements rotate because of dipole coupling even though no stress is applied on them. However, the dipole coupling is not strong enough to make them overcome their shape anisotropy energy, so they do not switch or flip their magnetizations.

After ~0.4 ns have elapsed and both the second and third multiferroics have their magnetizations oriented close to the in-plane hard axis, stress is removed abruptly from the second multiferroic, while the third is still held at 5.2 MPa compression. As shown in Fig.3.7, the magnetization of the second multiferroic now gradually relaxes to the nearly "up" state due to dipole interactions with its two neighbors and shape anisotropy. This shows successful execution of Bennett clocking, but this last relaxation takes another ~0.6 ns. Thus, the switching process that flips the second multiferroic's magnetization from "down" to nearly "up" takes a total time of ~ 0.4 ns + 0.6 ns = ~1.0 ns Hence, a bit propagates through one unit of the logic chain in ~ 1 ns, which makes the maximum allowed clock rate 1 GHz.

Let us now focus on the peripheral elements in the chain (nanomagnets 1 and 4). After t~ 0.4 ns, the first element's magnetization begins to rotate back towards $\phi_1 = -90^0$ once stress in removed from the second element. However, it can never quite reach $\phi_1 = -90^0$ because the second element's magnetization does not rotate beyond $\phi_2 \approx 70^0$ owing to the strong x-component of $\vec{H}_{dipole}$ caused by the magnetization of the third element. This dipole field also causes the fourth element's magnetization to settle at $\phi_4 \approx -66^0$. Since we had ensured that the dipole energy is much smaller than the shape anisotropy energy, the peripheral elements cannot rotate beyond $\sim -65^0$.

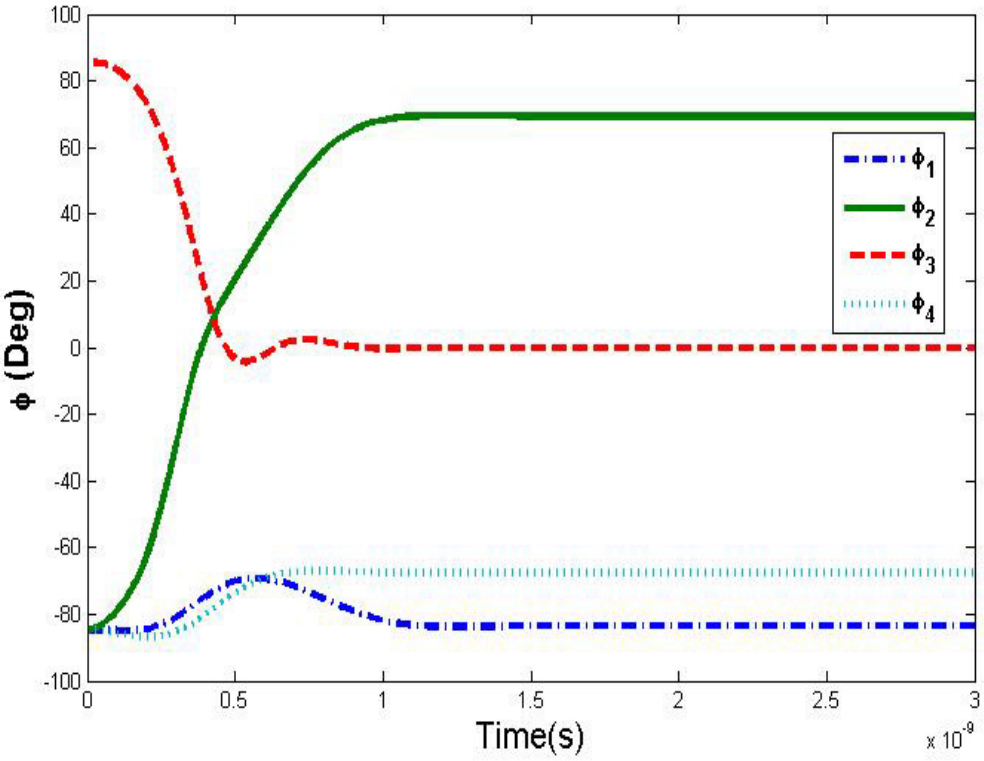

Fig.3.7.Magnetization angles ϕ [which are the projections of the magnetization vector on the magnet's plane] versus time plotted for the four multiferroic nanomagnets (PZT/Terfenol-D) in the chain shown in Fig. 2 when compressive stresses of 5.2 MPa are applied abruptly to the second and third nanomagnets at time t = 0 and t=0.02 ns, respectively. Stress is removed abruptly from the second nanomagnet after 0.386 ns when it assumes an orientation along the in-plane hard axis while the third nanomagnet remains stressed throughout this time interval. Note that even though magnets 1 and 4 are unstressed, their magnetizations rotate slightly because of dipole interaction with their stressed neighbors.

As already stated, the voltage required to generate a stress of 5.2 MPa in the PZT layer is ~ 26 mV. Hence, the energy dissipated in the clocking cycle is $(1/2)CV^2$ = 140 kT at room

temperature during the turn-on phase of the voltage and another $(1/2)CV^2$ = 140 *kT* during the turn-off phase. Thus, by dissipating 280 *kT* of energy *in the clocking circuit*, we can achieve ~ 1 GHz clock rate.

There is however some additional energy dissipated in the magnet itself when it reverses magnetization [38]. This energy is calculated as [5]

$$E_d = \int_0^{\tau} \frac{\alpha \mu_0 \gamma \Omega}{(1+\alpha^2) M_s} \left| \vec{M} \times \vec{H}_{eff} \right|^2 dt \qquad (3.3)$$

where $\vec{M} \times \vec{H}_{eff}$ is the effective torque acting on a nanomagnet due to the combined effects of shape anisotropy, stress and dipole interaction [5]. This energy is calculated numerically for all four magnets following the prescription of ref. [5] and then added up. It turns out to be another ~ 150 *kT*. Thus, the total energy dissipated per clock cycle per bit flip in this case is ~ 430 *kT*.

The magnetization vector of any magnet of course need not be constrained to the plane of the magnet under stress. It can lift out of the plane and the out-of-plane excursion is measured by the polar angle θ. Fig. 3.8 shows the extent of the out-of-plane excursion of the magnetization vector. The polar angles θ_2, θ_3 deviate by no more than 3^0 from 90^0, which is the magnet's plane, when the stress is 5.2 MPa. Thus, as long as the stress is small, the magnetization vector barely lifts out of the magnet's plane and virtually all the rotation takes place in the plane.

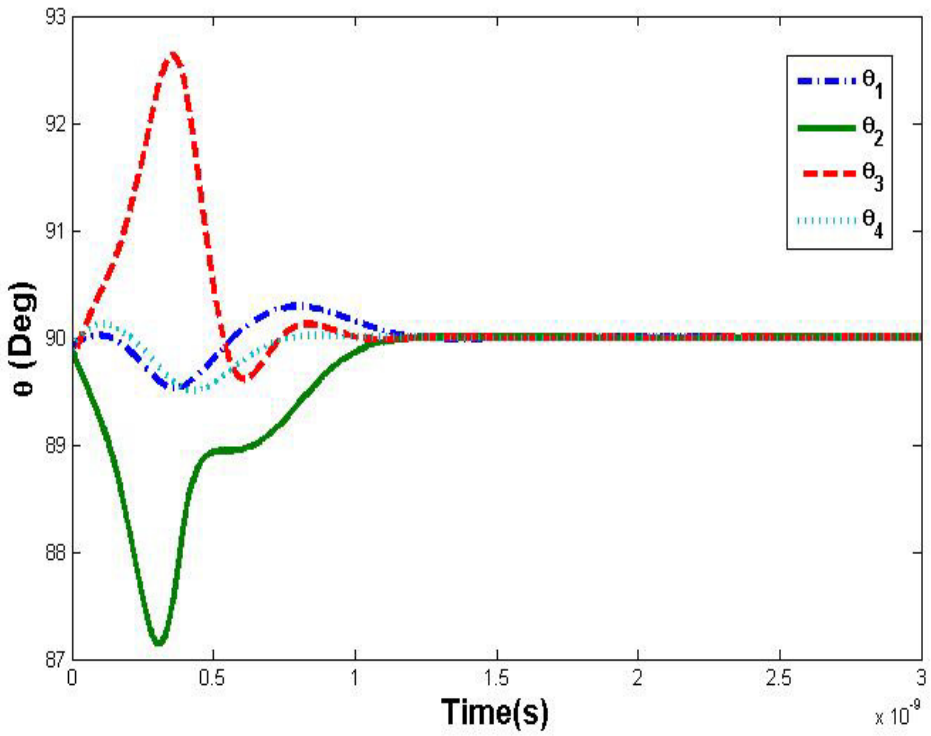

Fig 3.8. Out-of-plane excursion of the magnetization vector. Polar angles θ versus time plotted for the four nanomagnets in the chain shown in Fig.3.6 when the second and third nanomagnets are subjected to the stress cycle.

The complex motion of the tip of the magnetization vector in three-dimensional space is shown in Fig 3.9. Note that the tip always resides pretty much in the *x-y* plane which is the plane of the magnet. However, even the small out-of-plane excursion has a significant effect on the switching delay. It speeds up the switching because the "out-of-plane" magnetization leads to a significant H_{eff}along the z-direction due to the large out-of-plane shape anisotropy (demagnetization factor N_{d_zz}). Interestingly, this out of plane H_{eff} provides a large torque $\left(\vec{M} \times \vec{H}_{eff}\right)$ that speeds up the

in-plane rotation because switching via the precessional mode is faster than switching via the damped mode.

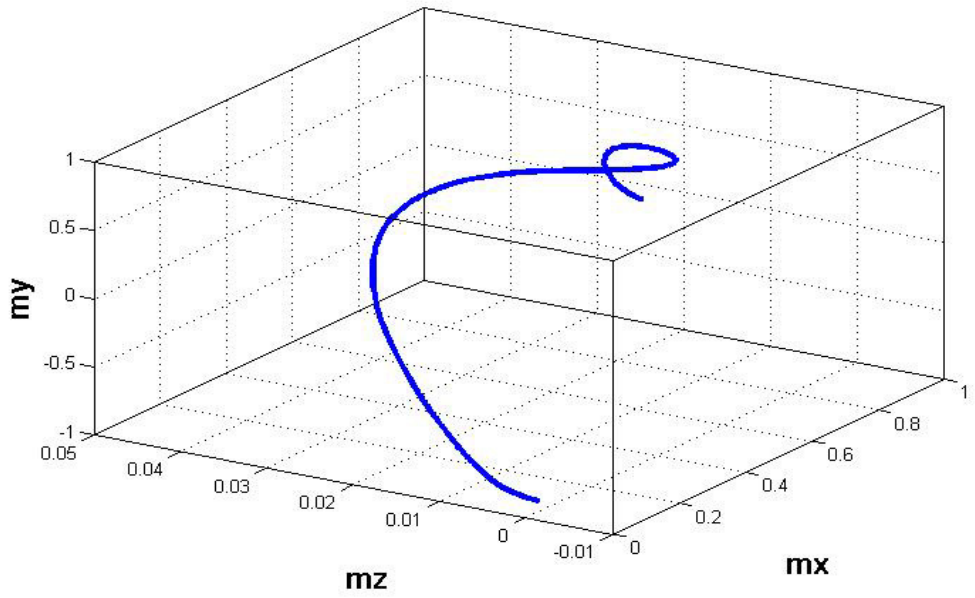

Fig 3.9 Three dimensional plot of magnetization components of nanomagnet 2 showing the spatial excursion of the tip of the magnetization vector. The stress cycle on all magnets is the same as in Figs. 3.7 and 3.8 .

3.3.2 - Case 2: Compressive stress of 40 MPa is applied on multiferroic nanomagnets 2 and 3 to align their magnetizations along the hard axis, followed by applying a tensile stress of 40 MPa on multiferroic nanomagnet 2 to help it relax to its easy axis faster and in the process flipping its magnetization.

The lessons learned from Case I tell us that we can make the switching process faster if we:

(i)Increase the magnitude of stress on the nanomagnets since that will result in a larger "effective field" $\vec{H}_{eff}$, and (ii)Make the relaxation from the hard to the easy axis faster for the second nanomagnet. This relaxation is slow since the only "driving force" on the nanomagnet after stress is removed comes from the effective field produced by the shape anisotropy and dipole coupling. Consequently, application of a tensile stress that drives the magnetization away from the hard axis could increase the "driving force" and make the relaxation faster. This would require that we reverse the stress from compressive to tensile on the second nanomagnet (by reversing the polarity of the voltage) after its magnetization vector reaches the hard axis.

Fig. 3.10 shows that merely increasing the compressive stress on the second and third nanomagnets from 5.2 MPa to 40 MPa decreases the time it takes to align both nanomagnets along the hard axis to about ~ 0.1 ns from the ~0.5 ns found in Case I. Once nanomagnets 2 and 3 line up along their common hard axis, we reverse the sign of the stress on the second nanomagnet from 40 MPa compression to 40 MPa tension, which then makes the magnetization relax to the nearly "up" state in only another ~0.5 ns, after all the ripples and ringing die down to around ~5º from the easy axis. Thus, by increasing the magnitude of stress and by aiding the relaxation process with stress reversal, we can shorten the total switching time from 1 ns to about 0.5 ns. This increases the maximum clock rate from 1 GHz to 2 GHz.

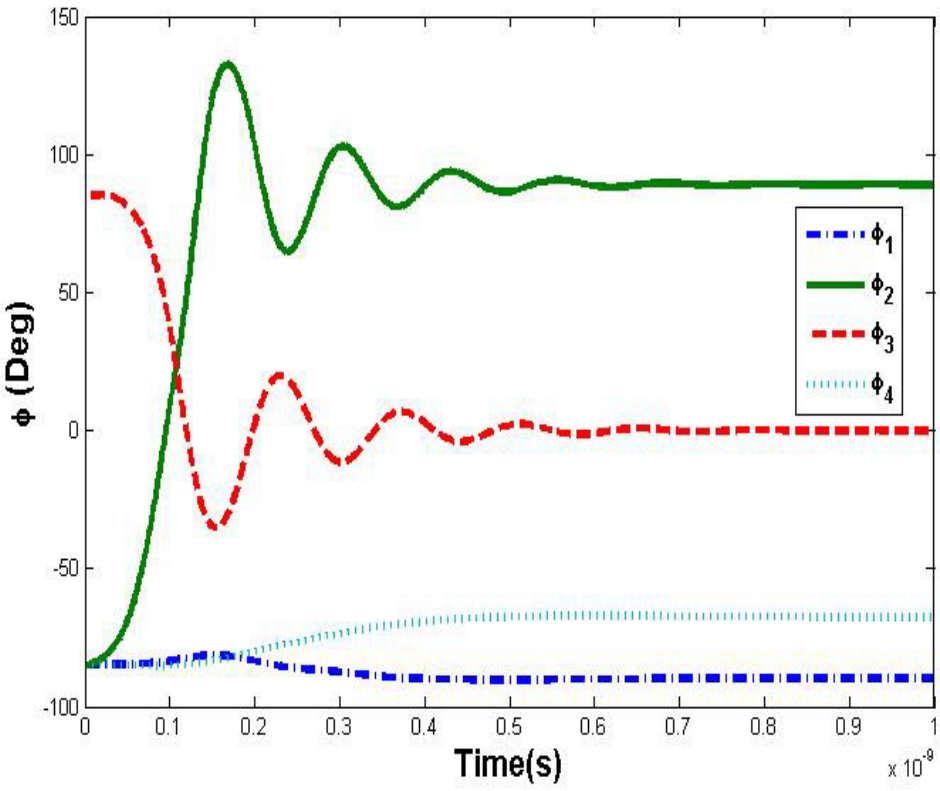

Fig 3.10 Magnetization angle ϕ versus time plotted for the four nanomagnets in the chain of Fig.3.5. A compressive stress of 40 MPa is applied abruptly on the second and third nanomagnets at time t = 0 and t=0.02 ns respectively with a voltage of 0.2 V. Stress on the second nanomagnet is reversed from compression to tension by switching the polarity of the voltage after 0.095 ns (i.e. after the nanomagnets come close to the hard axis) while the third nanomagnet is held at 40 MPa compression.

Here again, the dipole coupling is not strong enough to overcome the shape anisotropy energy; therefore, the magnetizations of first and the fourth nanomagnets do not rotate beyond ~ -65^0. The magnetization of the first nanomagnet reaches ~-83^0 around 0.15 ns but then rotates back to -90^0 (as the second nanomagnet settles close to the $+90^0$ state due to application of a high tensile

stress). The x-component of the $\vec{H}_{dipole}$ due to the magnetization of the third nanomagnet makes the magnetization of the fourth rotate further and settle at~ -66^0.

The energy dissipated in the clocking circuit is computed as follows: When the compressive stress is turned on, we will dissipate energy of $(1/2)CV^2$ in the clock line attached to either nanomagnet 2 or nanomagnet 3. When stress is reversed, we will dissipate an additional energy of $(1/2)C(2V)^2$ in the clock line attached to magnet 2. Finally, when stress is removed, we will dissipate energy of $(1/2)CV^2$ in the lines attached to either magnet. Thus, the total energy that we will spend to flip the magnetization of the second magnet is $3CV^2$, which is 50,000 kT since V = 200 mV and C = 1.74 fF.

To this energy we must add the energy dissipated in all four magnets during magnetization reversal. This additional energy is calculated numerically following the method of ref. [5] and it turns out to be another ~ 2000 kT at room temperature. Hence the total energy dissipated per clock cycle per bit flip is ~ 52,000 kT.

Fig. 3.11 shows the out-of-plane excursion of the magnetization vector. In this case, θ_2, θ_3 deviate by $\pm 15^0$ from the 90º position, showing that the magnetization vector lifts out of the magnet's plane by $\pm 15^0$.

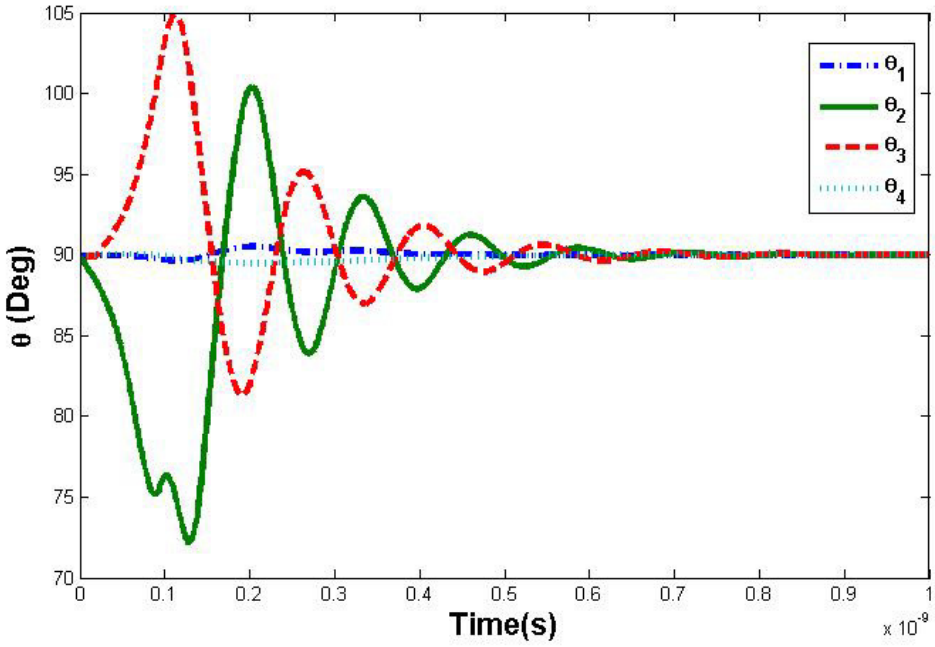

Fig 3.11. Out-of-plane excursion of the magnetization vector. Polar angle θ versus time plotted for the four nanomagnets in the chain of Fig3.5 . The stress cycle is the same as in Fig. 3.10.

This produces a large out-of-plane H_{eff} as explained earlier, which produces a large torque $\left(\vec{M} \times \vec{H}_{eff}\right)$ that speeds up the switching by causing significant processional motion of the magnetization vector. Fig. 3.12 shows the complex dynamics of the tip of the magnetization vector in three-dimensional space. This complex dynamics is responsible for all the ripples we see in Fig. 3.9 and 3.12.

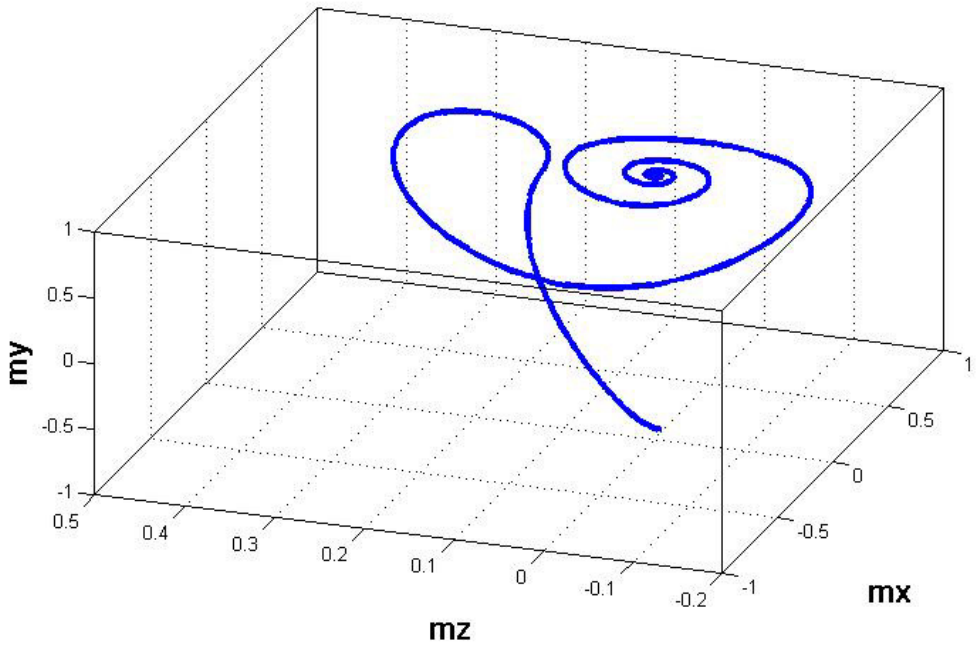

Fig 3.12. **:** Three dimensional plot of magnetization components of nanomagnet 2 showing the spatial excursion of the tip of the magnetization vector. The stress cycle on all magnets is the same as in Figs 3.10 and 3.11.

3.3.3 Conclusion for multiferroic nanomagnetic logic

In this section, we have discussed the magnetization dynamics associated with Bennett clocking of multiferroic logic by formulating and solving the appropriate LLG equations. Our results show that clock rates of 2 GHz are achievable with proper design if we use common materials like Terfenol-D and lead zirconium titanate (PZT) to construct the multiferroic logic switches. For a clock rate of 2 GHz, the energy dissipated per clock cycle per bit flip can be 1-2 orders of magnitude smaller than in transistor circuits [39] and at least 3 orders of magnitude smaller than in NML clocked with spin transfer torque. On the other hand, if we are willing to settle for a clock

rate of 1 GHz, then the energy dissipated is potentially 3 orders of magnitude smaller than in transistor circuits [39] and 6 orders of magnitude smaller than in NML driven with spin transfer torque. Moreover, transistors tend to have a leakage current and hence encounter significant standby power dissipation, which NML does not. Therefore, NML employing multiferroic nanomagnets can emerge as a very viable candidate for the next generation of computers and signal processors.

3.4 The universal multiferroic nanomagnetic logic gate

In this section, the switching dynamics of a multiferroic nanomagnetic NAND gate with fan-in/fan-out (Fig 3.13) is simulated by solving the Landau-Lifshitz-Gilbert (LLG) equation while neglecting thermal fluctuation effects. The gate and logic wires are implemented with dipole-coupled 2-phase (magnetostrictive/piezoelectric) multiferroic elements that are clocked with electrostatic potentials of ~50 mV applied to the piezoelectric layer generating 10.1 MPa stress in the magnetostrictive layers for switching. We show that a pipeline bit throughput rate of ~ 0.5 GHz is achievable with proper magnet layout and sinusoidal four-phase clocking. The gate operation is completed in 2 ns with a latency of 4 ns. We will show that the total (internal + external) energy dissipated for a single gate operation at this throughput rate can be achieved to be near ~ 500 kT in the gate and ~1250 kT in the 12-magnet array comprising two input and two output wires for fan-in and fan-out. This makes it respectively 3 and 5 orders of magnitude more energy-efficient than complementary-metal-oxide-semiconductor-transistor (CMOS) based and spin-transfer-torque-driven nanomagnet based NAND gates respectively. Finally, we show that the dissipation in the external clocking circuit can always be reduced asymptotically to zero using increasingly slow adiabatic clocking, such as by designing the RC time constant to be 3 orders of magnitude smaller

than the clocking period. However, the internal dissipation in the device must remain and cannot be eliminated if we want to perform fault-tolerant classical computing.

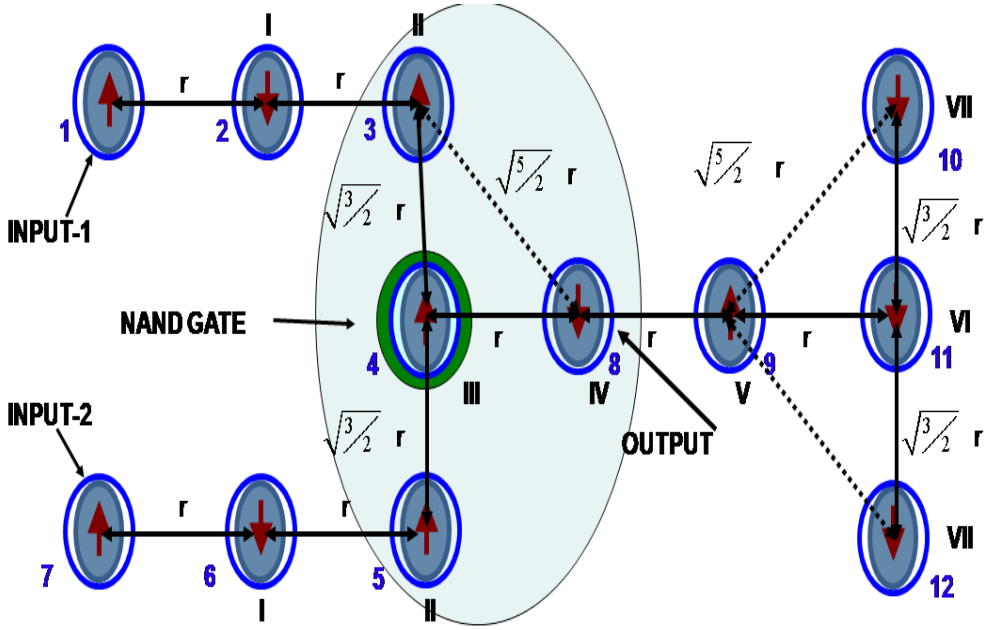

Fig 3.13. Schematic view of the Design of all multiferroic NAND gate with input "logic wires" and fan-out. The magnetization directions shown depict the correct initial (ground) state corresponsing to input-1 = 1 and input-2 = 1.

3.4.1 **Magnet switching schemes**

The nanomagnet's advantage over the transistor will be wasted if the method employed to switch the nanomagnet becomes so energy-inefficient that the energy dissipated in the switching circuit vastly exceeds the energy dissipated in the nanomagnet. In the end, this can make magnetic architectures less energy-efficient than transistor based architectures, thereby defeating the entire purpose of using magnetic switches. Therefore, the switching scheme is vital.

Magnets are typically switched with either a magnetic field generated by a current [40], or with spin transfer torque , or with domain wall motion induced by a spin polarized current. In the first approach, a local magnetic field is generated by a local current based on Ampere's law that leads to large I^2R losses in the circuit There is also another disadvantage; the magnetic field cannot be confined to small spaces, which means that individual magnets cannot be addressed unless the magnet density is sparse (magnet separation $\geq$ 0.5 μm). That not only reduces device density, but might make dipole interaction between magnets so weak as to make magnetic quantum cellular automata inoperable. Therefore, this method is best adapted to addressing not individual magnets, but groups of (closely spaced) magnets together. However, that approach makes magnetic quantum cellular automata architecture *non-pipelined* and hence very slow [17]. In the end, this is clearly not an optimal method of switching magnetic switches.

Spin transfer torque (STT) is better adapted to addressing individual magnets since it switches magnets with a spin polarized current passed directly through the magnet. It dissipates about 10^8kTof energy to switch a single-domain nanomagnet in ~ 1 ns, even when the energy barrier within the magnet is only ~ 30 kT [92]. Thus, it is not better than the first approach in terms of energy efficiency. A more efficient method of switching a magnet is by inducing domain wall motion by passing a spin polarized current through the magnet. There is at least one report of switching a multi-domain nanomagnet in 2 ns by this approach while dissipating 10^4kT– 10^5kT of energy [93]. This makes it 1-2 orders of magnitude more energy-efficient than a transistor in a circuit.

Recently, we devised a much more efficient magnet switching scheme. We showed that a 2-phase multiferroic nanomagnet, consisting of a piezoelectric layer elastically coupled with a magnetostrictive layer, can be switched by applying a small voltage of few mV to the piezoelectric layer [4], [7]. This voltage generates uniaxial strain in the piezoelectric layer that is transferred

almost entirely to the magnetostrictive layer by elastic coupling if the latter layer is much thinner than the former. Uniaxiality can be enforced in two ways: either by applying the electric field in the direction of expansion and contraction (d_{33} coupling) or by mechanically clamping the multiferroic in one direction and allowing expansion/contraction in the perpendicular direction through d_{31} coupling when the voltage is applied *across* the piezoelectric layer. The substrate is assumed to be a soft material (e.g. a polymer) that allows uniaxial expansion/contraction. The uniaxial strain/stress will cause the magnetization of the magnetostrictive layer to rotate by a large angle. Such rotations can be used for Bennett clocking of NML gates for logic bit propagation [4]. In ref. [5-7], we showed that the energy dissipated in the magnet and clock together is a few hundreds of kT for a switching delay of 1 ns or less. This makes it one of the most energy-efficient magnet switching schemes.

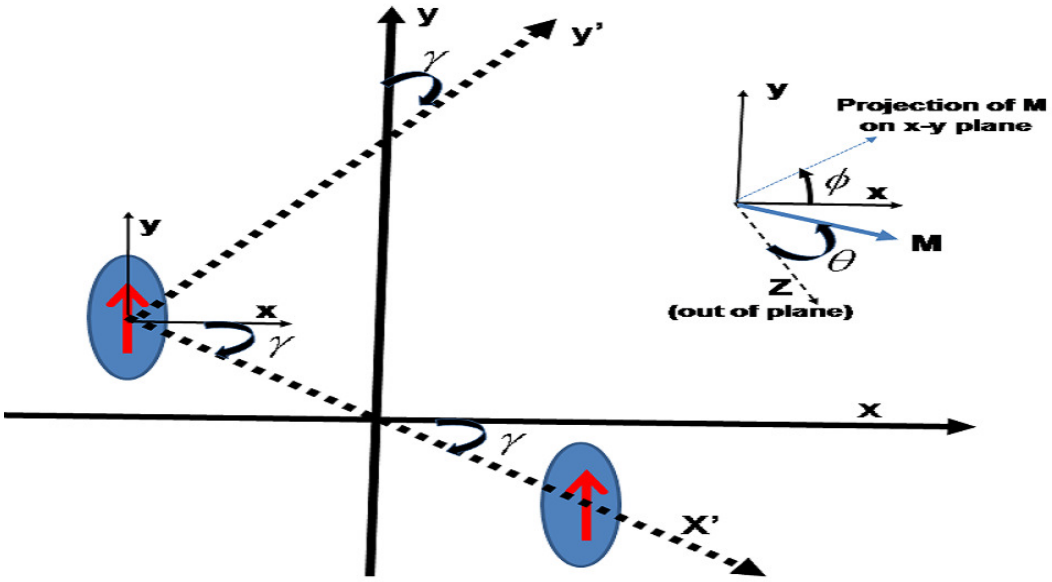

Fig 3.14. Two nanomagnets whose hard axes are at an angle γ to the line joining their centers

.

In this work, we will study the switching dynamics of a NAND gate with fan-in/fan-out wires implemented with multiferroic elements with dimension of 105nm~95nm~6nm and will calculate the energy dissipation in the entire block assuming low enough temperature when effects of thermal fluctuations can be neglected. At room temperature, thermal fluctuations will act as a random magnetic field that will increase the switching error probability and mandate higher stress levels or dipole coupling (along with larger energy dissipation) for reliable gate operation. This study is deferred to next chapters.

3.4.2 Results and discussions

In this section as in the last one, we have used 4^{th} order *Runge-Kutta* method, to solve the system of 24 coupled ordinary differential equations for a specific geometric pattern of twelve dipole coupled multiferroic elements shown in Fig. 3.13. These 12 magnets comprise the NAND-gate and wiring for fan-out. The stress applied on the four nanomagnets comprising the actual gate follows a 4-phase sinusoidal clocking scheme shown in Fig 3.14 . The magnets are grouped into 7 groups I through VII. The sinusoidal clocks applied to each group and the relative phase lags between the clock signals for different groups is shown in Fig. 3.15 .

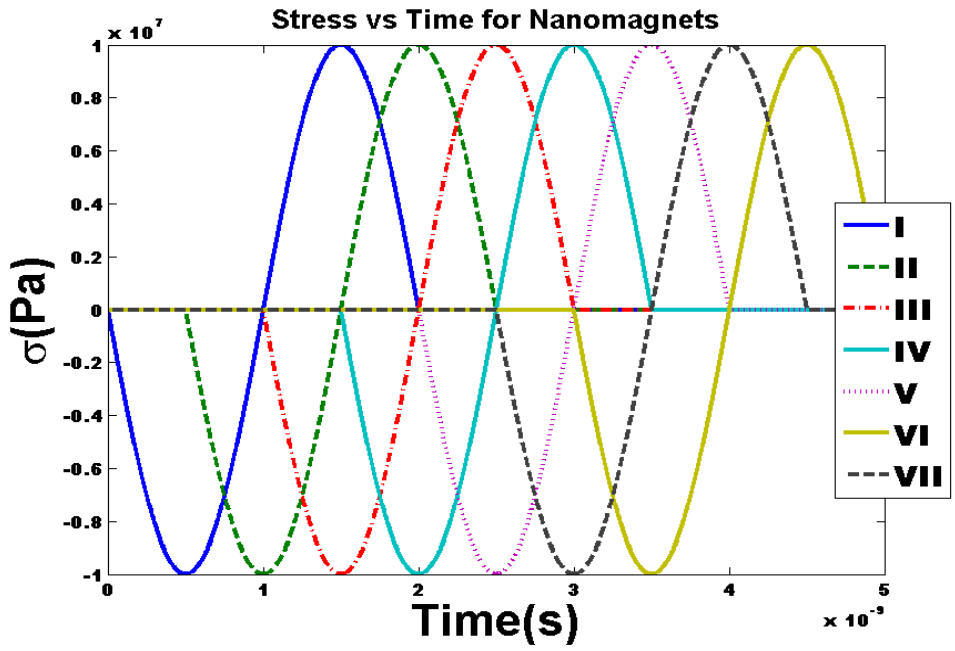

Fig 3.15 . A 4 phase clock showing sinusoidal stress applied to the nanomagnets.

Clearly, a 4-phase clock is required. When the phase for the clock on magnets marked "I" goes past 90º so that the compressive stress on these magnets begins to decrease, the compressive stress on magnets marked II just begins to increase. Thus, when the stress on magnets "I" has decreased to $\sqrt{1/2}$ of the maximum applied compression, the magnets marked "II" are at a state of $\sqrt{1/2}$ of the maximum compression and have been sufficiently rotated away from the easy direction. Consequently, as compressive stress decreases to a point where the shape anisotropy begins to dominate and therefore the magnetizations of magnets marked "I" rotate towards their easy axes, their orientation is influenced strongly and ultimately uniquely determined by the orientations of the "input" magnets ensuring uni-directionality of information propagation [5].

From the time-dependent voltages on any magnet, we derive the time-dependent stresses and hence the time dependent effective fields $\vec{H}_{eff}^{i}(t)$ on each magnet. These are used to solve the LLG

equation (24 coupled ODEs). The solutions yield the orientation $\theta_i(t)$, $\phi_i(t)$ of each element. The in-plane magnetization orientation ($\phi_i(t)$) of each of the 12 nanomagnets (Fig 3.14) is plotted to demonstrate: (i) successful NAND operation for any arbitrary input combination [(1,1), (0,0), (1,0), (0,1)] starting with the initial input state (1, 1), and (ii) the complete magnetization dynamics showing that the primitive gate operation is always completed in 2 ns and the latency is 4 ns.

In this study, we assumed that the magnetostrictive layers were made of polycrystalline Terfenol-D with material properties and dimensions given in Table3.1. The piezoelectric layer is assumed to be lead-zirconate-titanate (PZT) that has a reasonably large d_{31} coefficient (10^{-10}m/V[28]), albeit also a large relative dielectric constant of 1000. Terfenol-D was chosen for its high magnetostriction [32] .

Table.3.1 Material parameters and geometric design for Terfenol-D

$(3/2)\lambda_s$	9×10^{-4} [33]
M_s	0.8×10^{6} A m^{-1}
Young's modulus	8×10^{10} Pa [34]
α	0.1 [32]
Dimension $a\times b\times t$	$105nm\times95nm\times5.8nm$
r	200 nm

The geometric parameters for the individual magnets and the array were chosen to ensure: (i) The shape anisotropy energy of the elements was sufficiently high (~0.8 eV or ~32kT at room temperature) so that the bit error probability due to spontaneous magnetization flipping was very low ($\sim e^{-32} \approx 10^{-14}$). Further, this large shape anisotropy would need magnetic fields ~120 Oe to

flip the magnetization, making it robust to stray magnetic fields. (ii) The dipole interaction energy was limited to 0.11 eV which was significantly lower than the shape anisotropy energy to prevent spontaneous flipping of magnetization, but large enough to ensure that the magnetization of the multiferroic elements always flipped to the correct orientation when stress was applied, even under the influence of random thermal fluctuations, and (iii) the maximum applied stress of 10.1 MPa corresponded to a stress-anisotropy energy $\frac{3}{2}[\lambda_s \sigma \Omega] =$ ~100 kT that was significantly larger than the shape anisotropy energy barrier of 32 kT.

The reason why such large stress was required are: (1) some magnets (for example the magnet marked "III") had to overcome significant amount of dipole coupling from interaction with multiple neighbors to rotate close to the hard axis; (2) the stress anisotropy is least effective close to $\Phi=0$ and hence the stress had to be large to ensure fast magnetization rotation for angles close to the hard axis.

In all our simulations (Fig 3.16-3.19), the initial magnetizations of the nanomagnets always correspond to the ground state of the array corresponding to input bits “1” and “1”. When a new input stream arrives, the input bits are changed to conform to the new inputs. Thus, at time t = 0, the magnetizations of input-1 and input-2 are respectively set to (1, 1) [Fig 3.17],(0, 0) [Fig3.17] , (1, 0) [Fig 3.18], (0, 1) [Fig3.19].

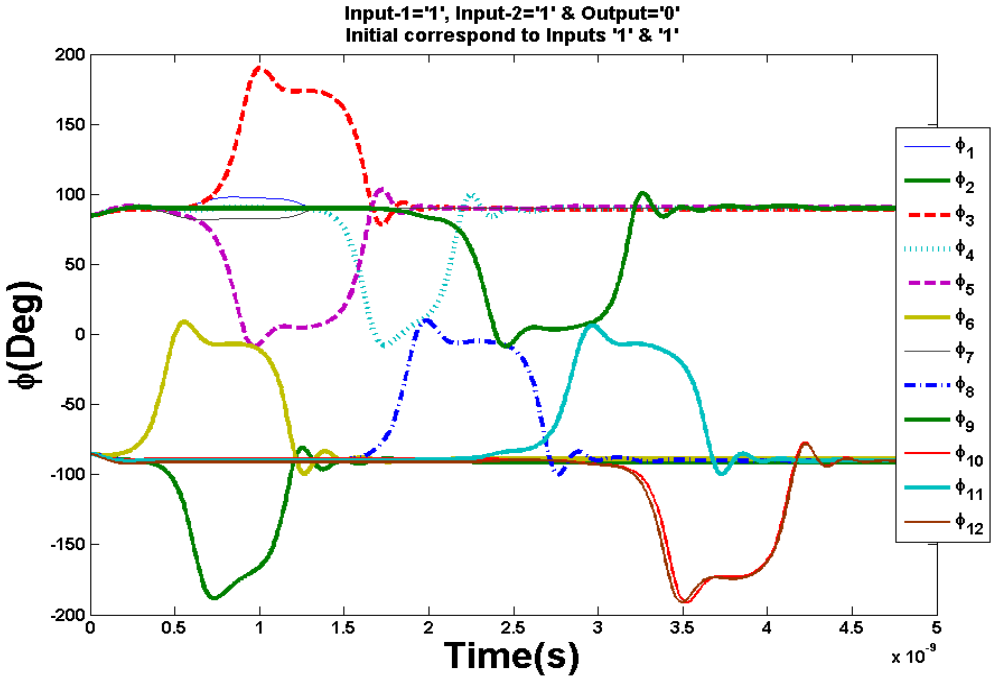

Fig.3.16. LLG simulation of magnetization dynamics of all magnets in the chain with initial (ground) states corresponding to the input-1=1 and input-2=1.

We then consider the time evolution of the in-plane magnetization orientations of every multiferroic nanomagnet when a 4-phase stress cycle is applied, as shown in Fig3.15 ,to clock the array. In Fig 3.16, the inputs are unchanged as input-1 = 1 and input-2 = 1. This is a trivial case as the ground state already corresponds to the correct output. But it is still important to simulate the magnetization dynamics to verify that the gate works correctly. As seen in Fig3.16, all magnetizations rotate through ±90º to the hard axis under compressive stress and then rotate back to their initial (correct) orientations under the influence of dipole coupling as the stresses are reversed to tensile. This results in a logical NAND output of "0". As expected there is a phase (and time) lag between instants when the compressive stress reaches a maximum and the magnetization is closest to the hard axis. This is because magnetization takes a finite time to respond to the applied stress, as is evident from the LLG equations.

In Fig 3.17, the inputs are both changed so that input-1 = 0 and input-2 = 0. Therefore, all the magnets in the input wire, gate and output wire flip through 180º, rotating first through ±90º on application of a compressive stress and then further rotating through ±90º under the influence of dipole coupling. The phasing of the clock not only ensures the correct logical NAND output of "1" is reached but that the information is propagated *unidirectionally* through the input branches as well as the three output branches. The 4-phase clock achieves the following: As the compressive stress on a magnet is lowered to a point where the shape anisotropy barrier is about to be restored, the compressive stress on its right (subsequent) neighbor has already rotated it towards its hard axis. Therefore, the state of its left (previous) neighbor determines the easy direction towards which the stressed magnet will relax as the stress in lowered. This ensures unidirectional logic bit propagation as in the case of Bennett clocking [28].

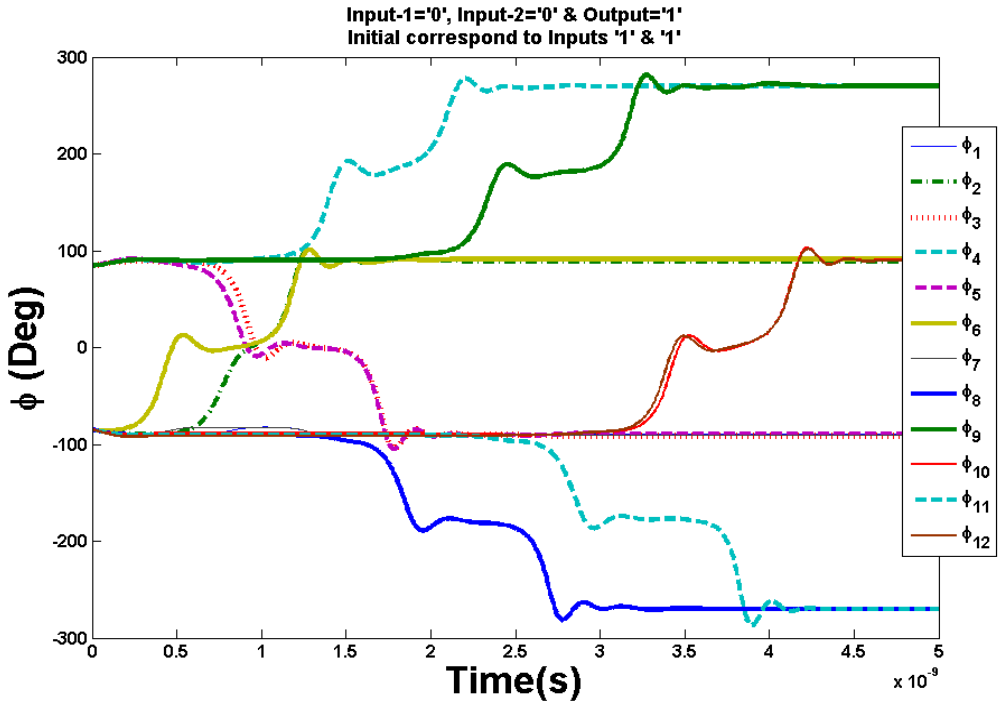

Fig.3.17, Input-1=0 and input-2=0 followed by applying 4-phase clock, which results in 1.

Finally, Figs.3.18 and Fig 3.19 show magnetization dynamics for the cases when one of the inputs is set to "1" while the other is set to "0". Here again the correct logical NAND output of "1" is achieved and propagated to the three fan-out branches.

In summary, we have proved through simulation that the NAND gate, fan-in and fan-out work correctly for all four input combinations for a given initial state of the nanomagnets. This was repeated for different initial ground states – (0, 0), (0, 1) and (1, 0) – in order to be exhaustive.

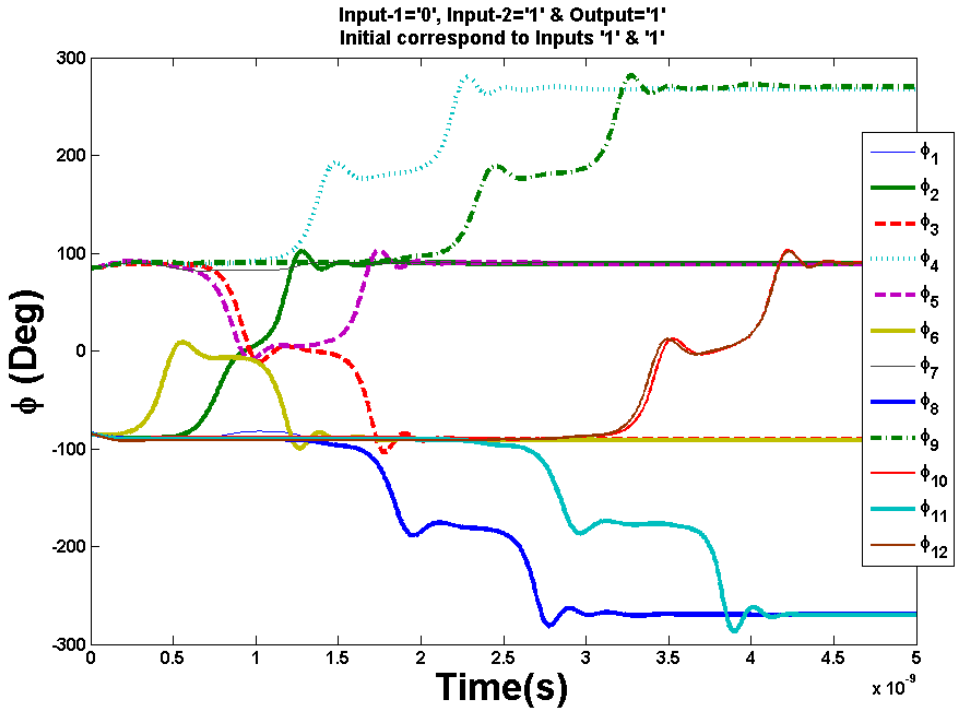

Fig 3.18. Input-1=0 and input-2=1 followed by applying 4-phase clock, which results in output=1.

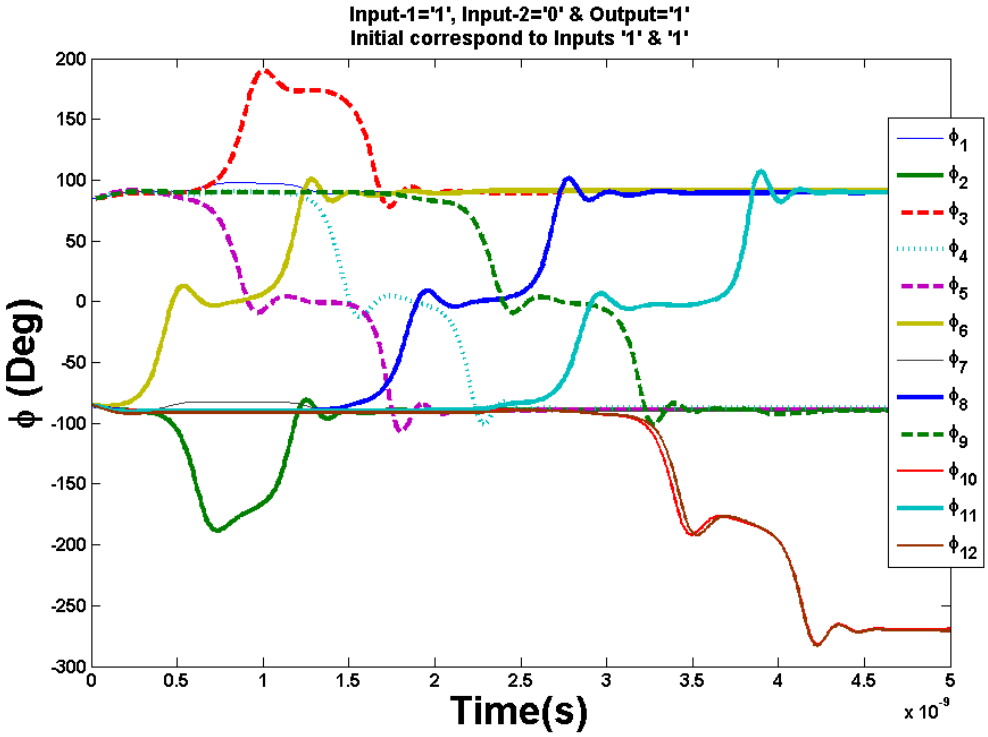

Fig 3.19. Input-1=1 and input-2=0 followed by applying 4-phase clock, which results in output=1

3.4.3 Energy considerations: power dissipated internally in the magnets and externally in the clock

There are two important sources of energy dissipation: (i) internal energy dissipated in the magnets due to Gilbert damping and (ii) external energy dissipated in the clock while charging the capacitance of the PZT layer that can be modeled as a parallel-plate capacitor.

(i) Internal energy dissipation

The internal energy E_d dissipated in the magnets during magnetization rotation under stress was estimated using equation (2.51). The energy dissipated in the 4 nanomagnets (magnets 3, 4, 5 and

8) that comprise the NAND gate over one clock cycle varied depending on the operation performed. For example, when both inputs were "1" (Fig 3.13) the internal energy dissipated for a NAND operation was 479.16 kT while when both inputs were set to "0" (Fig 3.17), the internal energy dissipated for a NAND operation increased to 517.46 kT. On the average, the energy dissipated in these four nanomagnets over one clock cycle is ~500 kT. When all 12 nanomagnets are considered, the average energy dissipated over one clock cycle is ~1250 kT for a NAND operation including fan-in/fan-out. Ultimately, this energy (~100kT/nanomagnet/bit) is well over the Landauer limit of *kTln(2)*[47] but considerably less than that dissipated in a transistor , or a nanomagnet switched with spin transfer torque[19], or domain wall motion [20] or current-generated magnetic field [18] when the gate operation is completed in 2 ns. The extremely low energy dissipation of ~1250 kT per gate operation that we theoretically demonstrate with multiferroic logic may be achievable with domain wall logic as well [100] (internal energy dissipation ~2000kT/operation) but at considerably lower clocking speeds than the 0.5 GHz frequency achievable with multiferroic logic. More importantly, the energy dissipated in the external circuit that drives spin polarized current to migrate domain walls (which we call the external energy dissipation or energy dissipated in the clock circuit) would be many times higher [100] than that dissipated in the clocking circuit for multiferroic logic employing straintronics. Thus, the present scheme offers unmatched energy efficiency.

The internal energy dissipation is governed by the (i) strength of dipole coupling needed to ensure the nanomagnets switch to the correct state with low dynamic error [51] under thermal noise and (ii) the large stress anisotropy needed to ensure that the switching is accomplished in ~ 2 ns. Thus, the internal dissipation depends on the error tolerance and the computational speed, as always.

(ii) Energy dissipated in the clock circuit (external dissipation)

The energy dissipated in the clocking circuit is governed by the electrostatic potential that must be applied across the PZT layer to generate the stress (10.1 MPa) needed to overcome shape anisotropy and flip the magnetization of the Terfenol-D layer fast enough to complete the gate operation in 2 ns. In this work, we assume that the PZT layer is 40 nm thick (so that most of the strain generated in it is transferred to the much thinner Terfenol-D layer). On application of an electrostatic potential of ~50 mV across the PZT layer, an electric field of 1.25 MV/m is generated in it. Since the d_{31} coefficient of PZT is ~ -10^{-10}m/V [37], this results in a strain of ~1250×10^{-6} in the PZT layer, which is transferred to the Terfenol-D layer. That produces a stress of ~10.1 MPa in the Terfenol-D layer since its Young's modulus is 8×10^{10} Pa.

Next, we estimate the capacitance of the ~40 nm thick PZT layer of surface area 105 nm × 95 nm and thickness 40 nm as 1.74 fF (relative dielectric constant ~ 1000 [37]). Thus the energy dissipated in applying first 50 mV across the PZT layer, then switching it to -50 mV and discharging to zero (to generate the stress cycle shown in Fig 3.16) is ~ 3200 kT per nanomagnet if this is done abruptly. The energy dissipated in charging the capacitor abruptly with a square wave pulse is $\frac{1}{2}CV^2$ so that charging it up to $+V$ from 0, reversing it to $-V$, and then discharging it back to 0 dissipates an energy of $3CV^2$.In contrast, driving an RC circuit with a sinusoidal source dissipates energy of $E_{clock} = \pi \frac{V^2}{R} \omega (RC)^2$, resulting in an energy saving by a factor $\frac{\pi \omega RC}{3}$. Abrupt (non-adiabatic) switching with a square wave pulse will cause a total energy dissipation of ~ 40,000 kT in the clocking circuit (or more than 10 times the internal energy dissipated in the nanomagnets). However, if the RC circuit is driven with a sinusoidal voltage of low frequency ($1/RC$), then clocking becomes quasi-adiabatic. This reduces dissipation considerably because of

the large energy saving factor. In our case, we assume that the PZT layer is electrically accessed with a silver wire of resistivity 2.6 μΩ-cm [36] so that an access line of length 10 μm and cross section 50 nm×50 nm has resistance ~100 Ω. Hence, the *RC* time constant is ~0.174 ps. The clock period is 2 ns, so that the reduction factor $\frac{\pi\omega RC}{3} = 5.47\times10^{-4}$. This makes the dissipation in the clock only about 22 kT, which is negligible compared to the internal energy dissipation of 1250 kT. The external dissipation can be eliminated altogether by replacing the RC circuit with an RLC circuit with the capacitor and inductor in parallel and the resistor in series. In this circuit, both the active dissipation and the reactive dissipation are zero if we drive the circuit at the resonant frequency $\omega_r = 1/\sqrt{LC}$. With an inductor of 5-6 mH, a resonant frequency of 0.5 GHz can be achieved.

3.5 Conclusions

In this chapter, we have modeled the nonlinear magnetization dynamics of an all-multiferroic nanomagnetic logic wire and a NAND gate with fan-in/fan-out and shown that a throughput of ~ 1 bit per 2 ns and latency ~4 ns can be achieved, so that the clock rate can be 0.5 GHz. Such a four dipole nanomagnets chain can dissipate near to 100kT/ bit and the gate circuit is estimated to dissipate ~ 1250kT/clock cycle internally in the 12 nanomagnets combined and much less energy (20 kT/clock cycle) in the external access circuitry for the clock signal, if we use a 4-phase clocking scheme with a sinusoidal voltage source driving an LCR circuit.

All this begs the question as to whether it is possible to reduce the internal energy dissipation by some appropriate scheme. This was discussed in ref. [3]. Imagine a magnet made of a material that has no Gilbert damping $(\alpha = 0)$. If we remove the shape anisotropy barrier and make the

magnet isotropic (circular disk), then a magnetic field applied perpendicular to the magnet's plane will make the magnetization vector precess around it without any damping in accordance with the first term in the right hand side of equation (2.45). There is now no internal dissipation. The magnetic field however must be removed *precisely* at the juncture when the magnetization completes 180^0 rotation if we wish to flip the bit. This requires exact precision; otherwise, the magnet will either not have completed 180^0 rotation, or overshot, resulting in more than 180^0 rotation. This error will continue to build up with time and finally become too large to endure. In other words, there is no fault tolerance. This is a well-known problem that has been discussed by numerous authors starting from the Fredkin billiard ball computer which can compute without dissipating energy [55], but cannot tolerate any error. Clearly, if we require fault tolerance, we must have damping, and hence some internal dissipation. In the presence of damping, fluctuations can deviate the magnetization from the desired orientation (minimum energy state), but the latter will return to the correct orientation (minimum energy state) by dissipating energy. Therefore, the dissipation in the clocking circuit can be eliminated by adiabatic approaches (increasingly slow switching), but the internal dissipation must remain for the sake of fault tolerance.

The internal energy dissipated in the magnet must be provided by the power source driving the clock. This source need not dissipate any energy to raise and lower the barrier separating the logic bits as long as we raise and lower the barrier adiabatically, but it must dissipate some energy internally in the logic device to maintain fault tolerance.

Chapter 4

Behavior of multiferroic nanomagnetic logic in the presence of thermal noise

4.1 Overview

The stress-induced switching behavior of a pair of dipole-coupled multiferroic nanomagnets in the presence of thermal noise at room temperature is numerically studied by solving the stochastic Landau-Lifshitz (LL) equation for a single domain macro-spin state. Different factors were found to affect the switching probability: (i) dipole coupling strength (ii) stress levels ;(iii) stress withdrawal rates (ramp rates), (iv) different stress profiles (Sinusoidal or pulse shaping), and (v) higher dipole coupling due to increasing of nanomagnet volume. We report that the thermal broadening of the magnetization distribution causes large errors in switching. This could become the bane of nonmagnetic logic schemes that rely on dipole coupling to perform Boolean logic operations.

4.2 Introduction

Dipole coupled shape-anisotropic nanomagnets with bistable magnetization are a popular platform for implementing logic circuits [1-2]. Because single domain nanomagnets flip by coherent spin rotation [3,25], they should dissipate very little energy (< 1 aJ) which ought to make nanomagnetic logic (NML) far more energy-efficient than traditional transistor-based logic. However, Bennett clocking is required to steer bits unidirectionally from one stage to another [15] and energy-inefficient Bennett clocking schemes may offset any possible energy advantage that magnets have. We have devised an extremely energy efficient clocking scheme employing strain-

induced switching of multiferroic nanomagnets which may result in superior nanomagnetic logic [4-6],[9,10,11,12] and memory [7,8]. It uses two-phase multiferroic nanomagnets consisting of a piezoelectric layer elastically coupled to a magnetostrictive layer (Fig 4.1 a). A voltage pulse applied across the piezoelectric layer generates a strain pulse which is transferred to the magnetostrictive layer and flips its magnetization because of the generated stress.

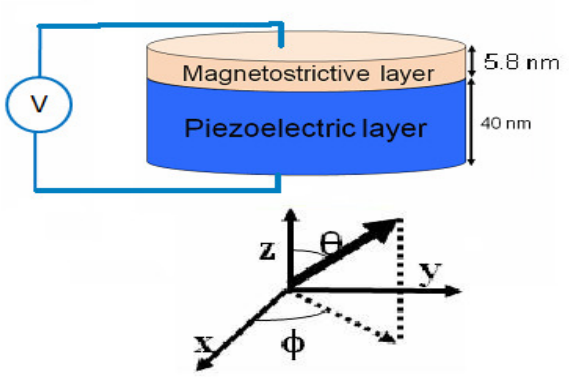

(a)

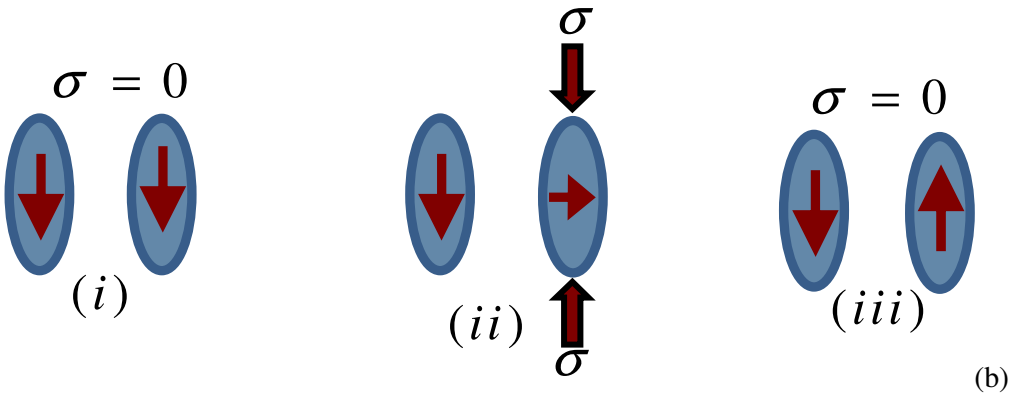

(b)

Fig 4.1 (a) An elliptical multiferroic nanomagnet consisting of a piezoelectric layer in intimate contact with a magnetostrictive layer. (b) A dipole-nanomagnet system comprising a hard magnet with large shape anisotropy and a soft multiferroic magnet with smaller shape anisotropy whose shape anisotropy energy barrier is modulated with stress. (i) The magnetizations are parallel (ii) Upon application of stress to the second nanomagnet, the shape anisotropy barrier is eroded to a point that the magnetization rotates close to the hard axis (iii) upon removal of stress the magnetization of the second magnet settles to a state anti-parallel to the first.

In an isolated magnet acting as a memory element, simple magnetization flipping is needed to write bits, but in a logic circuit that computes and produces an output depending on the inputs, conditional flipping conditioned on the state of other magnets is required. This is accomplished by dipole coupling the output magnet to the input magnet. The output magnet switches when it receives the appropriate clock (voltage) pulses. There is limited reliability analysis for such dipole coupled nanomagnetic logic in the presence of thermal noise [30,31].

In this chapter, we systematically study the influence of (i) dipole coupling strength,(ii) stress levels (clock amplitude),(iii) stress withdrawal rates (clock ramp rate), (iv) sinusoidal stress profile and (v) higher nanomagnet volume, which cause more dipole coupling on the switching probability of a dipole coupled nanomagnet pair in the presence of thermal noise. We further report that dipole coupled nonmagnetic computing is likely to be error-prone enough to make it unacceptable for Boolean logic. A more detailed study of error probability when "pulse shaping", (the use of different clock waveforms) is employed has been presented elsewhere[12].

4.3 Modeling magnetization dynamics in the presence of thermal noise.

We consider a pair of shape-anisotropic nanomagnets spaced far enough apart that in the ground state the magnetizations of the two magnets are mutually anti-parallel. This system is shown in Fig. 4.1(b). It is assumed that the magnetization of the left nanomagnet is stiff while that of the right nanomagnet rotates under the influence of both the dipole field exerted by the left nanomagnet and the clock-induced stress. We note that the "stiffness" condition imposed on the left nanomagnet is only an artificial condition introduced here to avoid simulation of the

entire array while still capturing the essential physics of switching with dipole coupling in the presence of thermal noise. Each nanomagnet has the shape of an elliptical cylinder as shown in Fig 4.1 (a-b) with a magnetostrictive layer ~5.8 nm thick deposited on a ~40nm thick PZT layer. This ensures that most of the strain generated in the PZT layer is transferred to the magnetostrictive layer through elastic coupling. It is further assumed that the PZT layer is mechanically constrained from expanding in the x-direction so that it generates a uniaxial strain along the major axis (y-direction) through d_{31} coupling when an electric field is applied across the PZT layer (in the z-direction). The nanomagnets dimensions are assumed to be 105 nm × 95 nm × 5.8 nm in all cases, so that the in-plane shape-anisotropy energy barrier between the two orientations along the easy axis (major axis of the ellipse) is ~ 0.75 eV (or ~ 32 kT at room temperature). This barrier prevents spontaneous switching of magnetization between the two stable orientations along the easy axis in the presence of thermal noise [4]. The magnet dimensions also ensure that the magnet has but a single ferromagnetic domain at equilibrium. The first step is to derive the potential energy of the single-domain soft nanomagnet on the right with uniform magnetization $\vec{M}(t)$.

A point dipole assumption is made to calculate the dipole coupling between the two single domain magnets. The total energy [4] is composed of the energy due to dipole coupling with the stiff left nanomagnet [22], shape-anisotropy [22] and stress-anisotropy caused by the clock pulse [22]:

$$U_i(t) = \underbrace{\frac{\mu_0 M_s^2 \Omega^2}{4\pi R^3}\left[(-2(\sin\theta_i\cos\phi_i)(\sin\theta_j\cos\phi_j)+(\sin\theta_i\sin\phi_i)(\sin\theta_j\sin\phi_j)+\cos\theta_i\cos\theta_j\right]}_{E_{dipole}}$$
$$+\underbrace{\left(\frac{\mu_0}{2}\right)\left[M_s^2\Omega\right]\left(N_{d\_xx}\left[\sin\theta_i(t)\cos\phi_i(t)\right]^2+N_{d\_yy}\left[\sin\theta_i(t)\sin\phi(t)_i\right]^2+N_{d\_zz}\left[\cos\theta_i(t)\right]^2\right)}_{E_{shape-anisotropy}}$$
$$-\underbrace{\left(\frac{3}{2}\lambda_s\sigma_i\Omega\right)\sin^2\theta_i(t)\sin^2\phi_i(t)}_{E_{stress-anisotropy}} \tag{4.1}$$

The effective magnetic field $\vec{H}_{eff}^{\,i}(t)$ acting on the right nanomagnet at any instant of time *t* is given by the gradient of the $U_i(t)$ with respect to its magnetization ($\vec{M}_i$).

$$\vec{H}_{eff}^{\,i}(t) = -\frac{1}{\mu_0\Omega}\frac{\partial U_i(t)}{\partial \vec{M}_i(t)} + \vec{H}_{thermal} = -\frac{1}{\mu_0 M_s \Omega}\nabla_{\vec{m}} U_i(t) + \vec{H}_{thermal} \tag{4.2}$$

In equations (4.1) and (4.2), M_S is the saturation magnetization of the magnetostrictive layer of the right nanomagnet; μ_0 is the permeability of vacuum; γ is the gyromagnetic ratio; Ω volume of the magnetostrictive layer; α is the Gilbert damping factor; N_{d_kk} is the demagnetization factor in the kth direction; λ_s is the saturation magnetostriction and *R* is the separation between two magnets. All model parameters including material constants and geometric details are summarized in Table-4.1 .

Table 4.1. Material parameters and geometric design for Terfenol-D

M_s	0.8×10^6 A m^{-1}
Young's modulus	8×10^{10} Pa
α	0.1
Dimension $a\times b\times t$	$105nm\times95nm\times5.8nm$

The effect of thermal fluctuation is modeled with a random field ($\vec{H}_{Thermal}$) with statistical properties in the manner of ref [29,30,34]and is modeled as:

$$\vec{H}_{ThermalNoise} = \sqrt{\frac{2K_B T\alpha}{\mu_0 M_s \gamma \Omega \Delta t}} (\vec{G}(t)) \tag{4.3}$$

Where $\vec{G}(t)$ is a Gaussian random distribution with mean of 0 and variance of 1 in each Cartesian coordinate axis; Δt is time step at simulation and is proportional to the inverse of the attempt frequency with which thermal noise disrupts magnetization; and K_B is the Boltzmann constant.

The effective magnetic field given by equation (4.2), which represents the effect of dipole coupling, stress anisotropy, shape anisotropy as well as random thermal noise, is used in the vector stochastic Landau-Lifshitz equation.

$$\frac{d\vec{M}(t)}{dt} = -\gamma \vec{M}(t) \times \vec{H}_{eff}(t) - \frac{\alpha\gamma}{M_s}\left[\vec{M}(t) \times \left(\vec{M}(t) \times \vec{H}_{eff}(t)\right)\right] \tag{4.4}$$

to compute the temporal evaluation of magnetization vector $\vec{M}(t)$ of the right multiferroic nanomagnet under the simultaneous actions of the dipole interaction with its stiff left neighbor, its own shape anisotropy, stress and random thermal noise.

A simulation for a simple case with constant stress is shown in Fig 4.2 Since the magnitude of the magnetization vector is invariant in time, we assume that in spherical coordinates, the orientation of this vector is completely described by the polar angle θ and azimuthal angle ϕ, as shown in Fig. 4.1 (a). We assume a single domain macro-spin approximation here, following Reference [25], but non equilibrium dynamics may produce some deviations from this assumption [60].

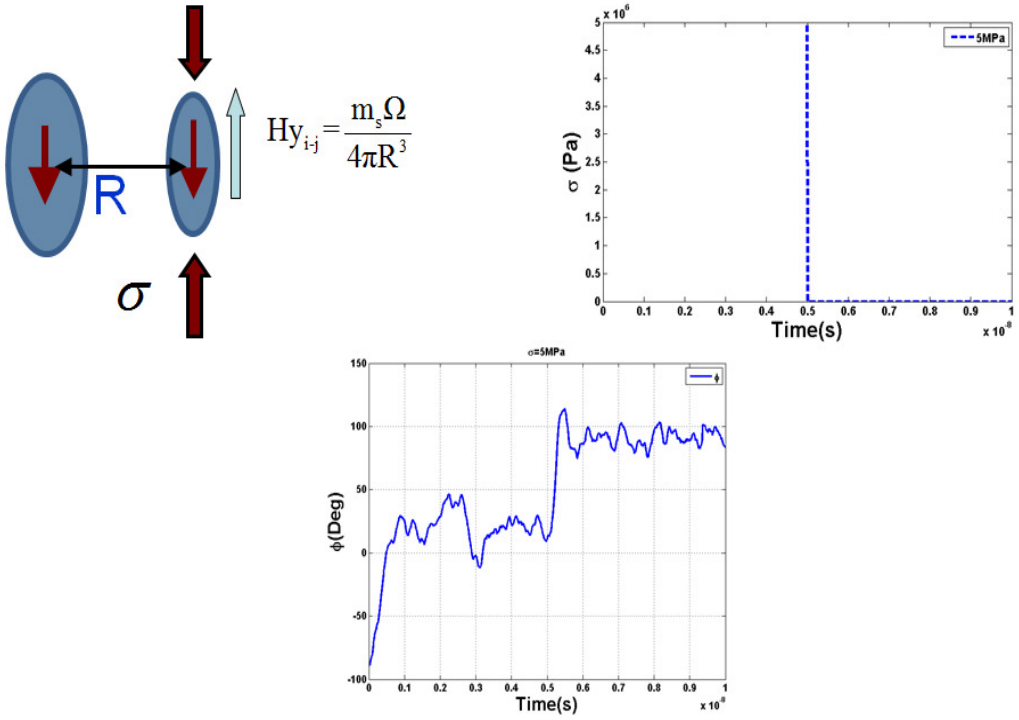

Fig 4.2. Dynamic fluctuation for a coupled nanomagnet system under 5(MPa) stress.

We assume that the magnetization vector of the right nanomagnet is initially aligned along a stable state, i.e. one of two possible orientations along the easy (major) axis of the magnetostrictive layer. An external agent flips the left stiff magnet and puts the system in a metastable state where the magnetizations of the two magnets become temporarily parallel. The right magnet is then clocked to generate stress, which will attempt to kick the system out of the metastable state into the ground state by flipping the magnetization and aligning it along the other stable orientation along the easy axis. If and when this happens, the two magnetizations become anti-parallel.

In order to simulate the different switching trajectories (under the random thermal field) by solving equation (4.4), each time we picked the initial angle randomly from the Boltzmann distribution, and ran 20,000 such simulations. The simulation is terminated when ϕ approaches

within $5^0$of $\pm 90^0$. If switching terminates near $\phi_i = -90^0$ (initial orientation), then we conclude that switching failed, whereas if it terminates near $\phi_i = +90^0$, we conclude that magnetization did flip and switching succeeded. Based on this, we found the switching error probability (fraction of switching trajectories that ended in failure) as well as the time evolution of the distribution of magnetization orientations during withdrawal of stress. In general, we hold the stress for long enough so the magnetization distribution reaches equilibrium before withdrawal of stress The key question we seek to answer is how the strength of dipole coupling, stress magnitudes, stress withdrawal rates (clock ramp rate) affect switching error probability.

4.4 Analysis of switching error in the presence of thermal noise

In this section, we analyze the influence of the following parameters on switching error probability:

(i) Dipole coupling strength (varying the spacing between the magnets) for different stress levels.

(ii)Stress withdrawal rate (ramp down time 1 ps to 5ns) for different levels of stress at an intermagnet spacing of *R*=200 nm.

(iii) The use of sinusoidal clocking at different stress levels by consideration of the stress frequency of 0.4 GHz and R=200nm.

(iv)Using of thick (~10 nm) and closely spaced nanomagnets to increase dipole coupling to see if the error can be decreased.

The error probability is the fraction of times the magnetization of the soft right magnet fails to switch from parallel to anti-parallel configuration upon application of stress, or erroneously switches from anti-parallel to parallel configuration upon application of stress. We do not consider the latter possibility here since that type of error has very similar probability if we wait long enough to reach equilibrium after application of stress.

4.4.1 Effect of dipole coupling at various stress levels.

The effect of dipole coupling on switching error at various stress levels is shown in Fig 4.3. It should be noted that the stress levels studied here are all above the critical stress defined as the stress at which the stress anisotropy energy equals the shape anisotropy. This is the minimum stress needed to overcome the shape anisotropy energy barrier and make it possible for the magnet to switch.

$$E_{Stress-anisotropy} = E_{Shape-anisotropy} \Rightarrow -\frac{3}{2}\lambda_S \sigma_{Critical}\Omega = [N_{d-xx} - N_{d-yy}](\mu_0/2)M_S^2\Omega \tag{4.5}$$

$$\sigma_{Critical} = \left| \frac{[N_{d-xx} - N_{d-yy}](\mu_0/2)M_S^2}{-\frac{3}{2}\lambda_S} \right| \sim 3.145 \text{ MPa (compressive)}$$

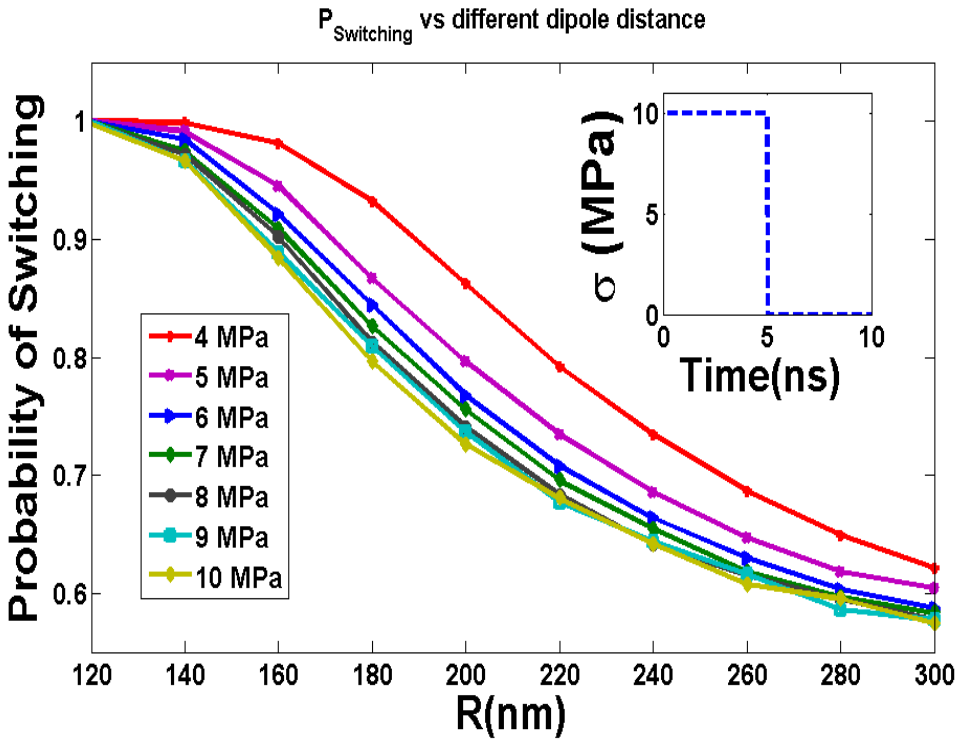

Fig.4.3. Probability of switching vs. pitch between the two nanomagnets (R) at different stress rates for sudden withdrawal of stress. Nanomagnet dimensions: 105×95×5.8 nm

In Fig 4.3 , the error probability decreases with increasing dipole coupling (smaller spacing R) independent of stress. Further, for any given dipole coupling strength, the error probability increases with increasing excess compressive stress (above the critical stress). Both these trends can be explained using the schematic shown in Fig 4.4.

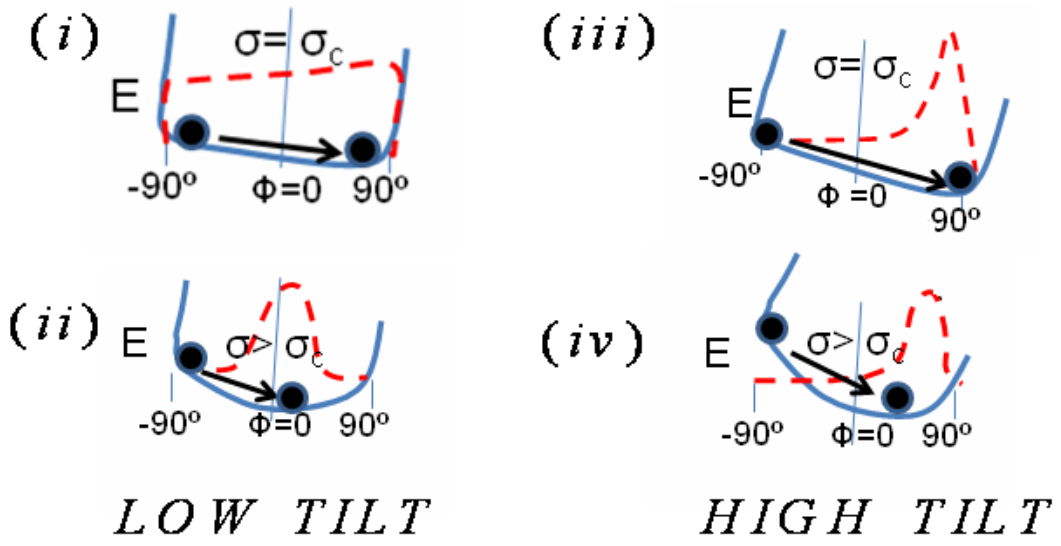

Fig 4.4.Schematic that shows the effect of dipole coupling (tilt/asymmetry) and stress on the energy profile and the magnetization distribution. This distribution affects the dynamic switching ultimately affects the dynamics error (that is minimum for critical stress and high dipole strength) NOTE: Blue thick line: shows energy profile. Red dotted line: corresponding probability distribution function for the magnetization orientation. (i) Low tilt (weak dipole coupling), critical stress (σ_C). (ii) Low tilt (weak dipole coupling), high stress ($>\sigma_C$). (iii) High tilt (strong dipole coupling), critical stress (σ_C). (iv) High tilt (strong dipole coupling, high stress ($>\sigma_C$)

Clearly, when the dipole coupling strength is greater (spacing is smaller), the energy landscape in Fig 4.4 is such that the magnetization distribution is greatly skewed towards the anti-parallel state and hence the probability that it would end up in the parallel (wrong) state upon stress withdrawal is smaller. Now, for a given dipole coupling strength, more excess stress makes the magnetization distribution less *skewed towards the anti-parallel state* since the energy profile is modified by stress (Fig 4.5) to *increase* the *likelihood* of the magnetization *aligning close to the hard axis*. This is why too much stress is undesirable and increases the error rate.

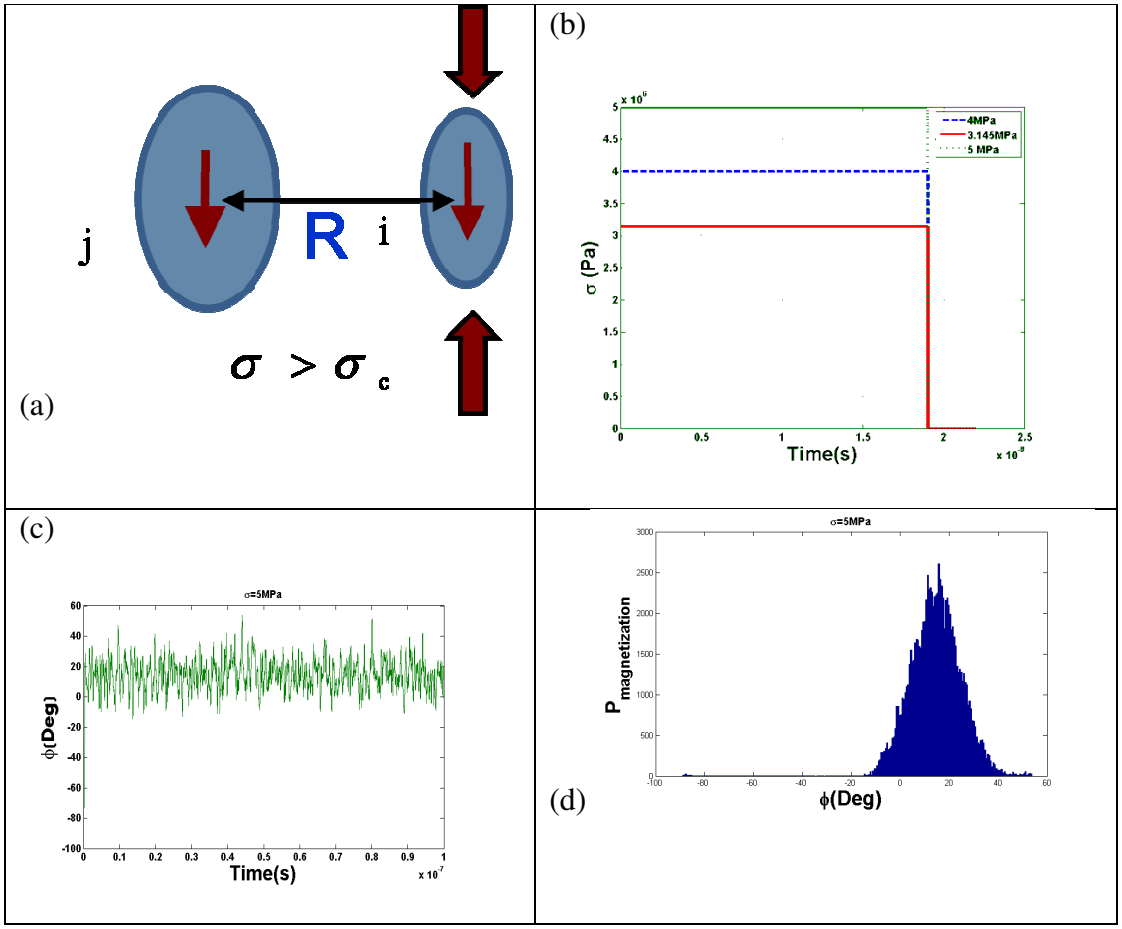

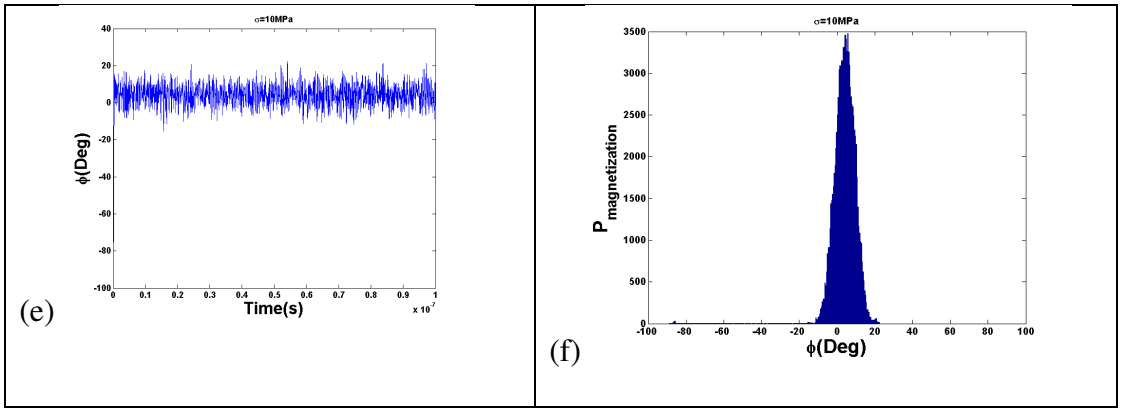

Fig 4.5(a-f). Schematic histogram behavior of a dipole nanomagnet under different stress profile

Fig 4.5 (a-f) explains the schematic histogram of the dipole-coupled nanomagnet under two different stresses that are both higher than the critical stress. When we apply higher stress, the magnetization direction of nanomagnet is confined more closely to the hard axis.

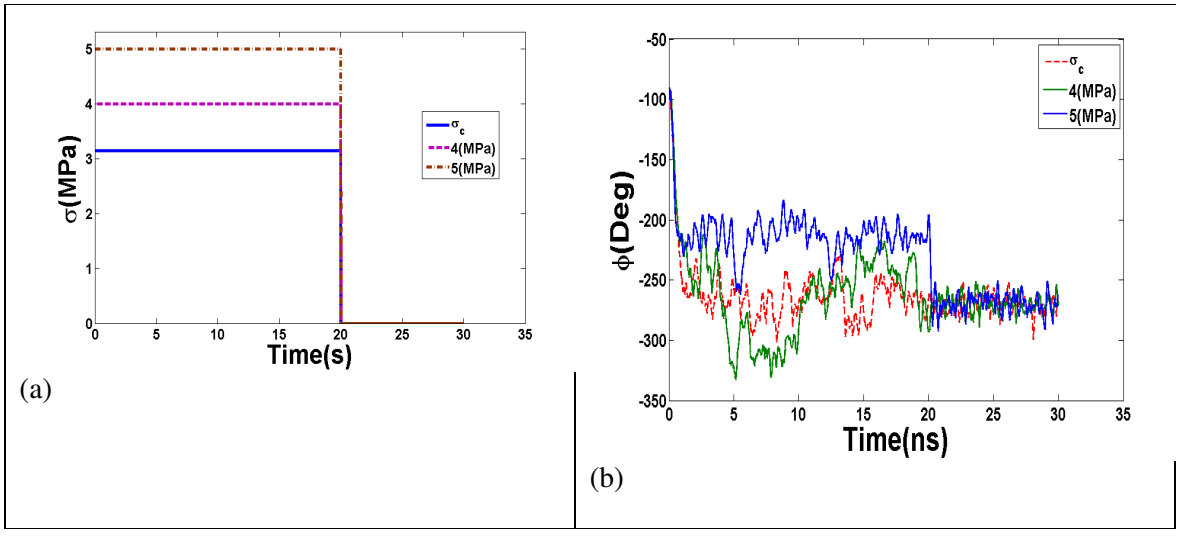

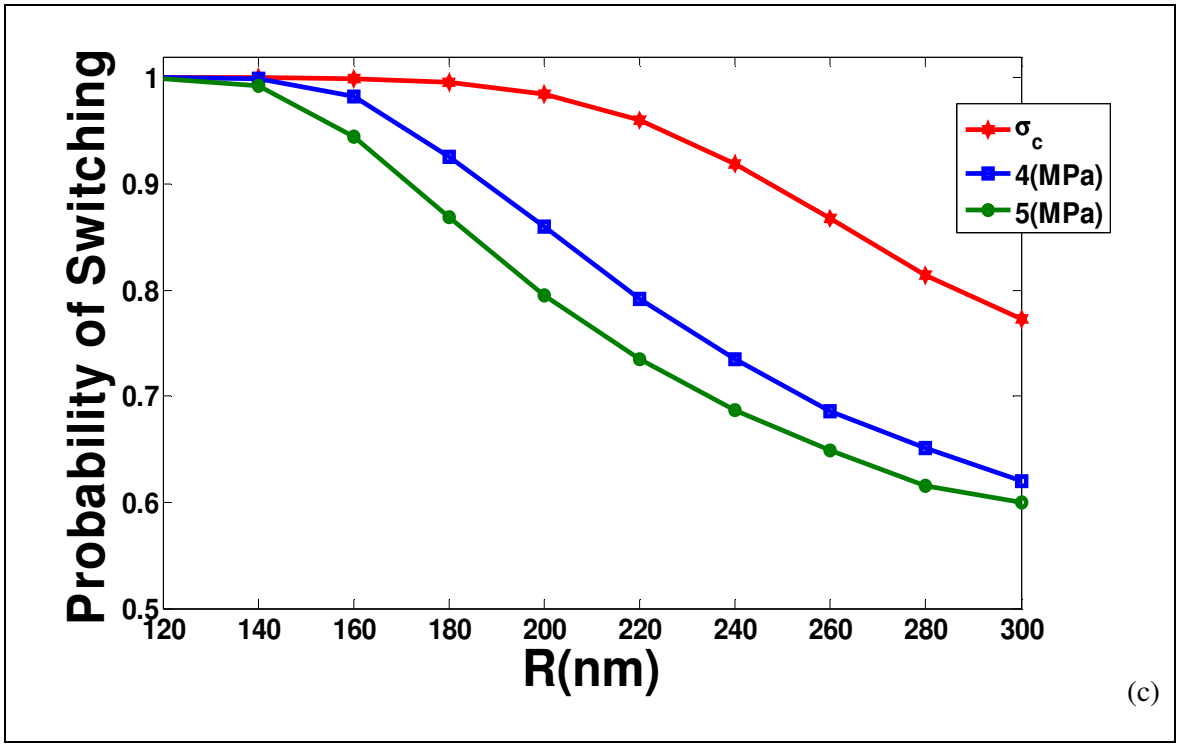

Fig 4.6.(a) Stress profile of 3.145MPa,4MPa and 5MPa are applied to the couple nanomagnet shown in Fig 4.5(a). (b) Dynamic behavior of a coupled nanomagnet with different stress and in the presence of thermal noise. (c) Probability of correct switching vs. the distance between nanomagnets for different stresses.

4.4.2Effect of stress withdrawal time (ramp rate) at various stress levels

The effect of stress withdrawal rate is less intuitive. Magnetization dynamics of a nanomagnet during slow withdrawal of stress is shown in Fig 4.7. We analyze the effect of stress withdrawal rate (ramp time of 1ps, 1 ns, 2 ns, 3 ns, 4 ns and 5 ns) in Fig 4.8 for a large range of stresses for a fixed dipole coupling strength corresponding to a spacing of 200 nm. The trends clearly show that for all stresses the error probability decreases with increasing stress withdrawal time (slow ramp). However, another important trend emerges: for fast stress withdrawal (~1ps) the error rate is strongly dependent on the stress level whereas for slower stress withdrawal rates (~5 ns), the error

rate depends less critically on the applied stress. All the above trends can be explained using the schematic in Fig 4.4 When the barrier (due to shape anisotropy) is suddenly raised (due to sudden stress withdrawal ~1 ps) [see Fig 4.4 b (ii) and (iii) that describe the process, and Fig 4.4, (ii) and (iv) that show the in-plane magnetization distribution], the magnetizations that are skewed towards the anti-parallel state will switch correctly while those (minority) skewed towards the parallel state have insufficient time to correct themselves and therefore switch to the wrong state.

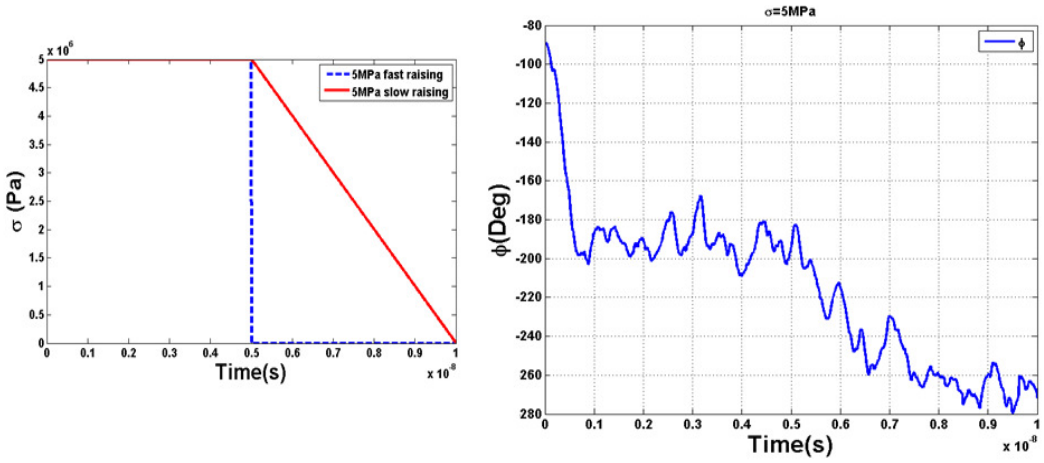

Fig 4.7 Schematic in-plane switching for 5MPa stress, which be removed in 5ns.

Now, if the stress is withdrawn slowly (~5 ns) despite an initially high stress [unfavorable magnetization distribution, Fig 4.4, (ii)] the energy profile has to gradually pass through the critical stress state [favorable orientation, Fig 4.4, (i)] before the barrier is finally restored. In this case, even if a larger fraction of magnetizations were originally skewed towards the parallel or wrong state [as in Fig 4.4, (ii),(iv)], they have ample time to correct themselves and switch to the anti-parallel (correct) state as the energy profile gradually changes to favor switching to this state [as in Fig , (i)]. However, even with slow stress withdrawal (~5 ns), moderate dipole (~200 nm pitch) and critical stress, the error rate is ~ 4%. With high dipole coupling (pitch of 120 nm, the minimum

allowed so the ground state is anti-ferromagnetic) and ~ 5ns stress withdrawal time, the error will still be ~ 0.0050 %.

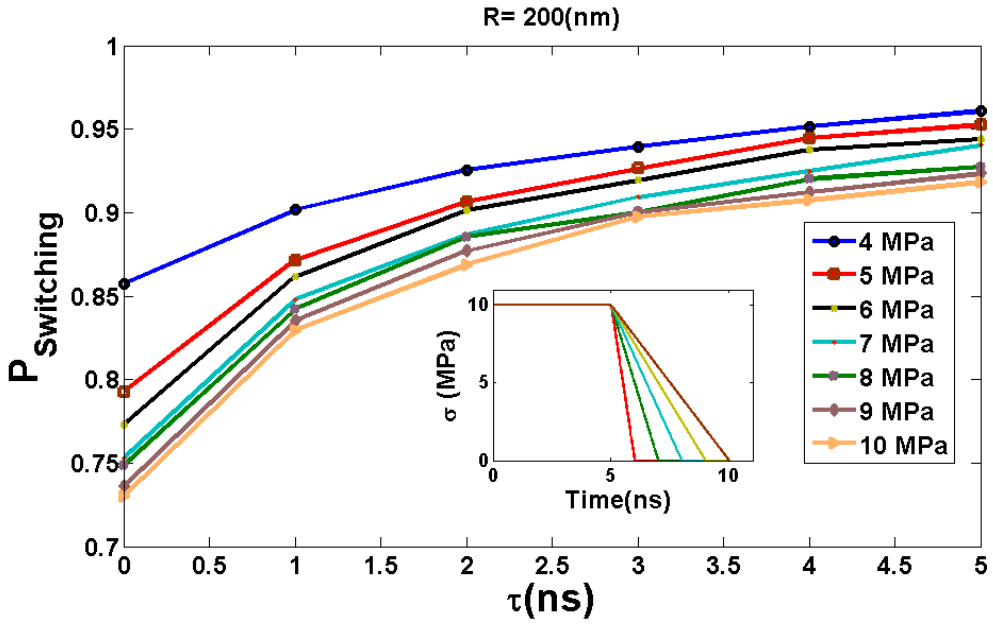

Fig 4.8 Probability of switching vs. τ (time for raising the energy barrier, i.e. time for withdrawal of stress) at fixed pitch =200nm and different stress levels. Nanomagnet dimensions: 105×95×5.8 nm.

4.4.3 The use of sinusoidal clocking at different stress levels

Finally, for practical clocking applications we also study sinusoidal stress profiles as these are more energy efficient (see LRC circuit implementation discussed in Ref [6]) and are better suited to multi-phase clocking (again see Ref [6] for multi-phase Bennett clocking of a NAND gate with fan-out). The results in Fig 4.10 (a) show switching probability vs. time-period (T).The switching error probability at the highest possible dipole coupling strength (spacing ~120nm) is going to be small at lower frequency (higher T) for both small stress (~ 4 MPa and 5 MPa, though both exceed the critical stress) and high stress (~10 MPa). For T ~2.5(ns), the amount of

stress(4MPa, 5MPa and 6 MPa) applied for ~1.25 ns (half the time period) by and large insufficient to even rotate most of the magnetization towards the hard axis, while the large stresses are sufficient for switching as shown in Fig 4.10 (a).

The details of these trends is shown in Fig 4.10 (a). There is a critical range of stresses ~(8-10) MPa where the error is lowest in even low T (high frequency) which is shown in fig 4.10 (a) as the dipole dominates the switching. With such optimal choice of stress, relatively slow clocking time (T~4(ns)) and highest possible dipole coupling strength (spacing ~120 nm), the error probability would reach $<10^{-4}$ for switching. Also, probability of switching vs. dipole distance for T=2.5ns is shown in Fig 4.10(b).

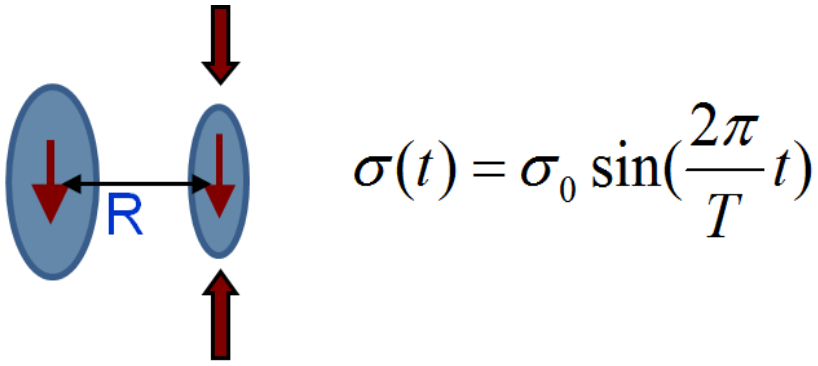

Fig 4.9. Sinusoidal stress is applied to a couple nanomagnet. With frequency of (1/T).

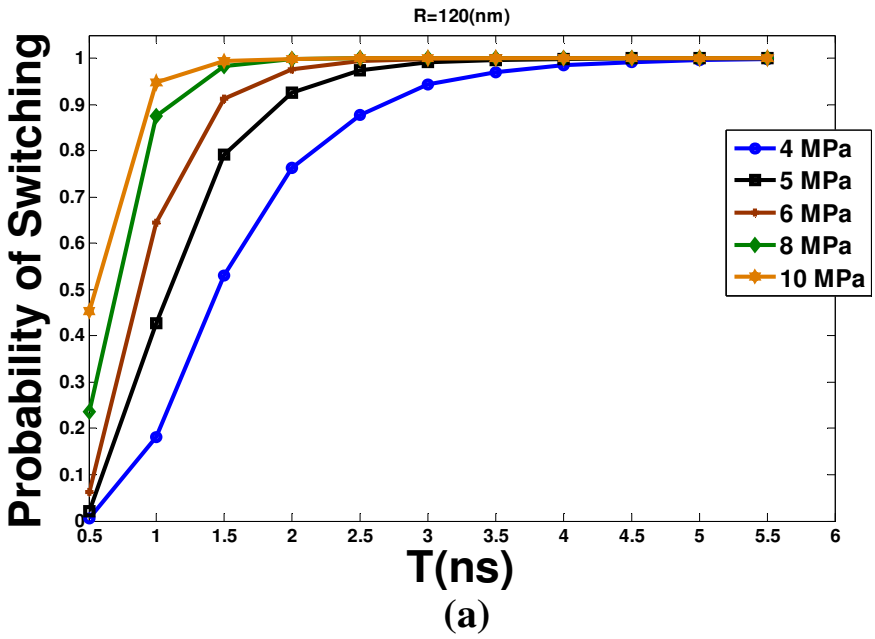

(a)

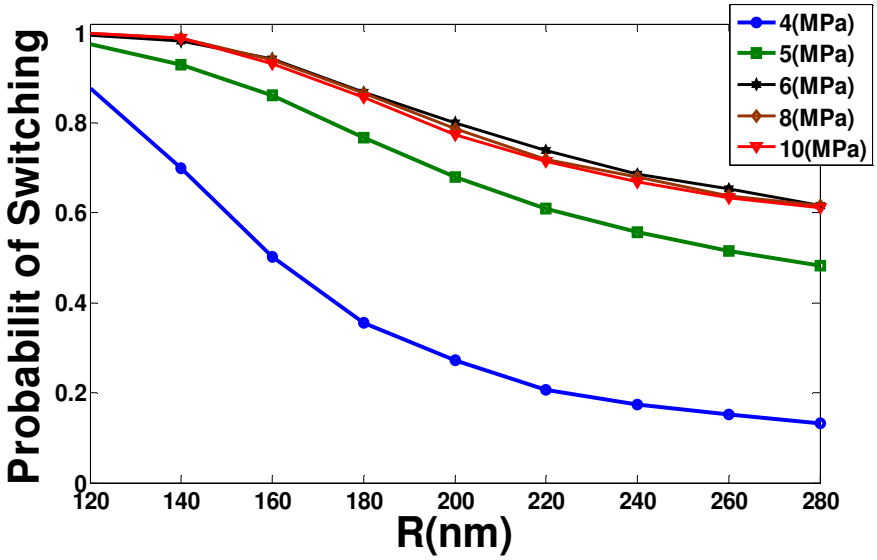

(b)

Fig 4.10 Probability of correct switching with sinusoidal stress vs. (a) T (ns) for high dipole coupling , and (b) vs. distance of nanomagnet(R) for T=2.5(ns).

4.4.4 Increased dipole coupling

All this begs the question whether it is possible to decrease the error probability to acceptable values by increasing the dipole coupling strength. This can be achieved by bringing magnets closer together but too short a distance may make the dipole coupling energy larger than the shape anisotropy energy, at which point the bistability of the magnets will be lost and all magnets will couple ferromagnetically with the same magnetization. Thus, there is a minimum allowable spacing between magnets. A second approach is to use thicker nanomagnets to increase the dipole coupling strength without decreasing the magnet density. Suppose the thickness was increased to ~10 nm, the low N_{d_zz} necessitates using lateral dimensions ~105×95 nm for the ellipse to keep $[Nd_{xx}\text{-}Nd_{yy}]$ low so that the in-plane shape anisotropy barrier remains at ~2 eV.
This is necessary so that the shape anisotropy barrier can be easily overcome by stress anisotropy generated by the low "clocking" stress. Such precise geometric tolerance may be feasible with current lithographic technology. But, more importantly, increasing the volume of dipole nanomagnet leads to improvement in magnetization switching even at lower stresses. The result for t=10nm is shown in Fig 4.11.

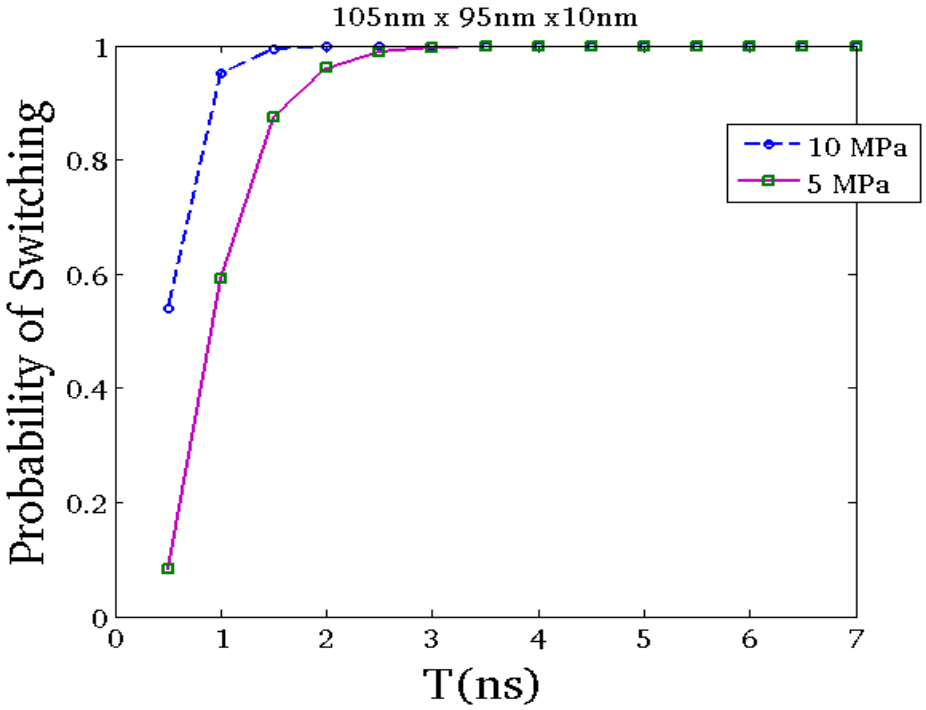

Fig 4.11 Probability of correct switching for a coupled nanomagnet with different thickness.

4.5 Multiferroic nanomagnetic NAND gate error

In order to assess the reliability of stress-induced switching behavior of a multiferroic nanomagnetic NAND gate in the presence of thermal noise, numerical studies has been performed by solving the stochastic Landau-Lifshitz-Gilbert (LLG) equation. A simple analysis is performed in the system of eight nanomagnets to estimate SML NAND gate reliability with 2 stiff inputs, as shown in Fig 4.12. Here, the input nanomagnets are assumed to be stiff while the others switches in the presence of thermal noise when clocked by four-phase sinusoidal stress on each group (I, II, III, and IV). This work could lead to an understanding of the reliability of more a complicated multiferroic nanomagnetic logic gate.

In Ref **[59],** they have studied effect of thermal noise on MQCA and its limitation due to it. They found that the error rate for such a gate at room temperature is high as more than >1% for most designs. Also, G.Csaba et al [56] have shown that longer nanomagnetic logic chain (n>5) have high error rates. However, they pointed out that such MQCA gate operating at 2ns, shows error rate of $P_{error} < 10^{-4}$.

In this work, we methodically explore how switching errors in the NAND gate is affected by (i) different frequency applied to "clock" the nanomagnets; (ii) different temperatures for a fixed center to center distance of 120 nm (maximum dipole couple possible). We note that each nanomagnet is designed to by 105 nm ×95 nm ×10 nm. In each case the simulation was performed for different clocking stress magnitudes while applying a four-phase sinusoidal stress. The results are shown in Figures 4.13 and 4.14 respectively.

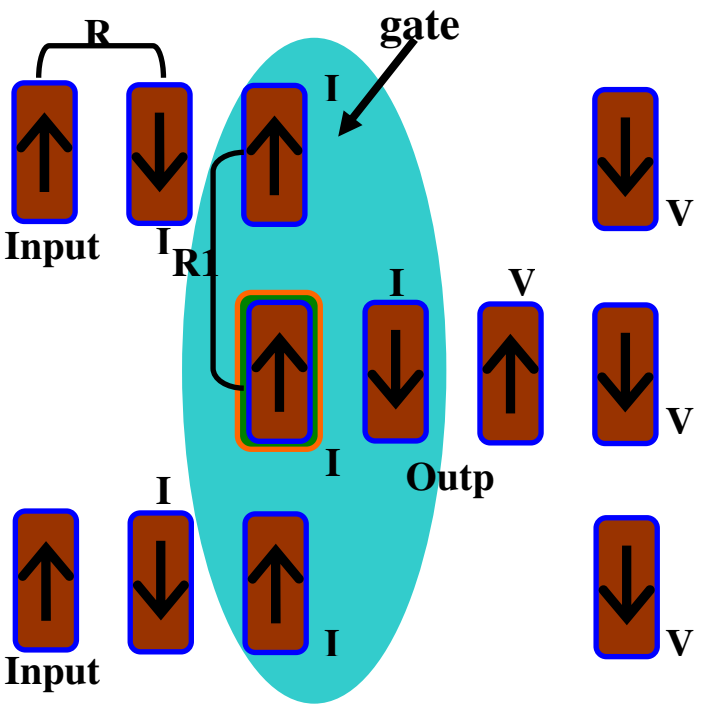

Fig.4.12. Schematic configuration of two inputs and output multiferroics NAND gate for calculating error rate in the presence of thermal noise.

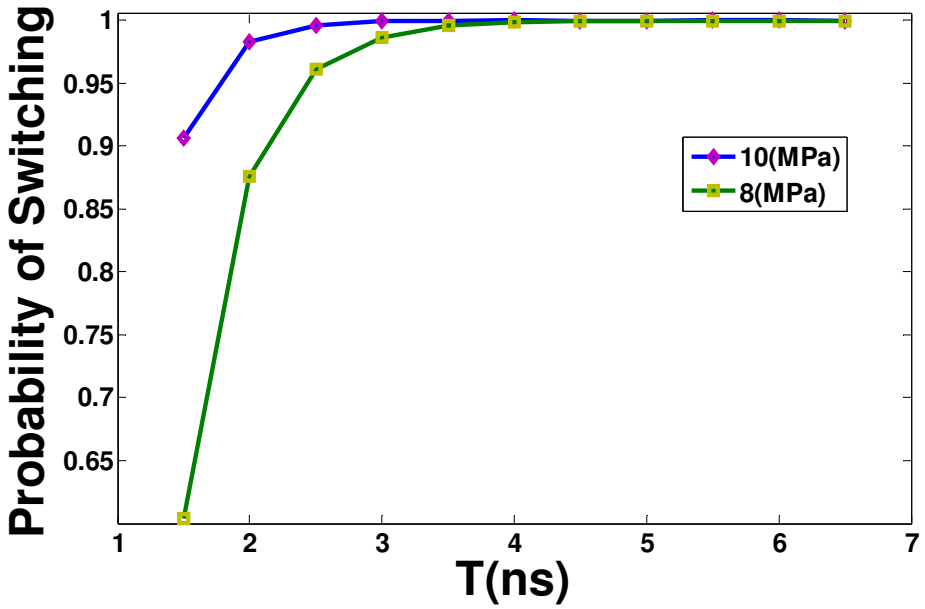

Fig 4.13. Show Probability of correct switching vs. time period of stress profile.

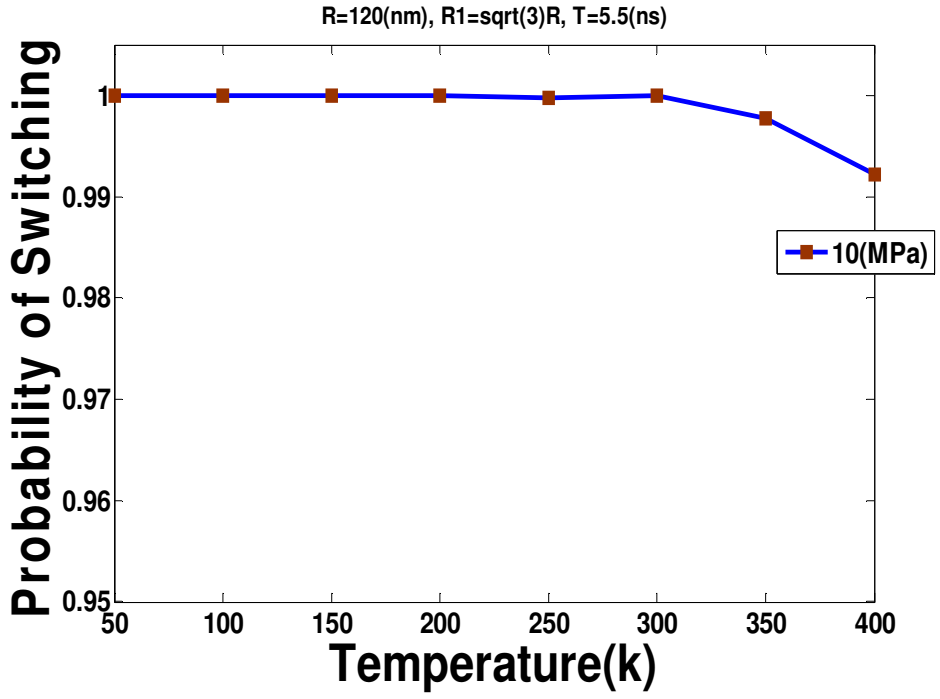

Fig 4.14. Probability of correct switching at different temperature.

4.6 Conclusions

We have modeled the magnetization dynamics of a strain clocked multiferroic nanomagnet under the action of dipole coupling from a neighboring magnet in the presence of thermal noise. We systematically study the effect of stress, dipole coupling, stress-withdrawal rate, sinusoidal stress profile and higher nanomagnet volume on the switching error and offer physical explanations of why this error is minimized at slow stress withdrawal rates, high dipole coupling and intermediate stress magnitudes. However, even with largest possible dipole coupling that would allow an anti-ferromagnetic ground state, the switching error probability is still ~ **0.005%** which is rather large. This magnitude of error probability is unacceptable for logic which needs to be much more robust and reliable than memory because error-correction is very difficult in logic circuits.

In summary, dipole coupled nanomagnetic logic seems to be quite error-prone and is not salvaged by increasing dipole coupling strength up to allowable limits. A similar message was conveyed in prior numerical [59]and recent experimental [61] work. Innovative pulse shaping schemes [12] and novel hardware error correction schemes may alleviate this problem to some extent, but it seems unlikely that stringent error requirements of $10^{-9}$to 10^{-12}error probability in conventional Boolean logic can be met. This does not mean that "magnetic computing" is doomed; it merely points to a serious shortcoming of dipole coupled architectures. Boolean logic schemes that do not rely on dipole coupling and non-Boolean computing schemes may still emerge as viable and energy efficient methods of computing.

Chapter 5

Limits to energy dissipation vs. error rate in practical nanomagnetic logic in the presence of thermal noise.

Overview

The potential energy profile of a binary switch is a symmetric double well. The standard method of switching it with no energy dissipation is to modulate the potential barrier separating the wells in time and tilting the profile towards the desired well just *at the precise juncture* when the barrier disappears. This demands perfect timing synchronization and is therefore fault-intolerant, even in the absence of noise. A fault-tolerant strategy that requires no time modulation of the barrier (and hence no timing synchronization) requires tilting the profile by an amount at least equal to the barrier height and dissipates that amount of energy. Here, we present a third strategy that requires a time modulated barrier but no timing synchronization. It is therefore fault-tolerant, in the absence of thermal noise and yet it dissipates arbitrarily small energy since an arbitrarily small tilt is required for slow and adiabatic switching. This case is exemplified with stress induced switching of a shape-anisotropic single-domain nanomagnet dipole coupled to a neighbor. We also show by examining various energy profiles and the corresponding probability distributions that in the presence of thermal noise, the minimum energy dissipated to switch in this scheme approaches the limit $2kTln(1/p)$ [p = switching error probability].

5.1 Introduction

The fundamental limits of energy dissipation in computing [3,47,50,51,52,53,55] are best understood by exploring the minimal energy dissipated to toggle a binary switch from one state to the other. The potential energy profile of the switch is a *symmetric* double well as shown in the far left sketch of Fig. 5.1, with the two degenerate minima corresponding to the two stable states.

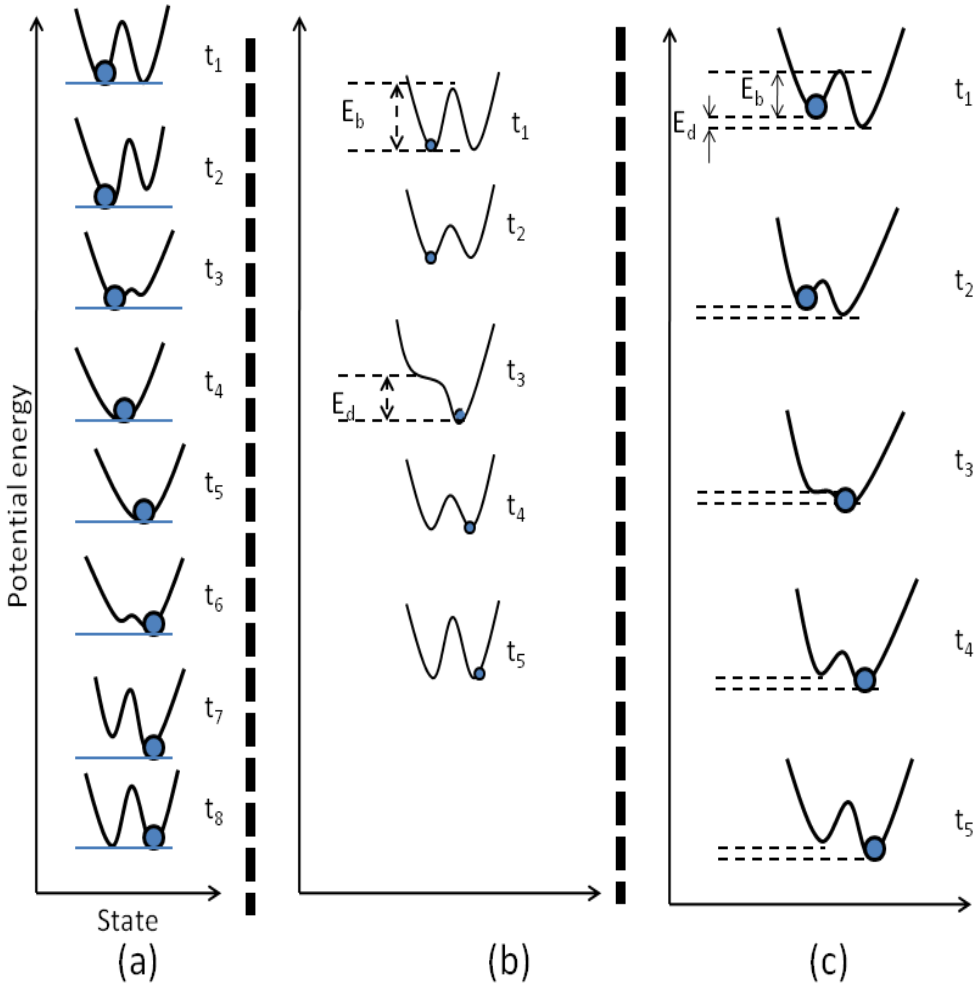

Fig.5.1 Switching stratergies involving: (a) infinitely precise synchronization but near zero energy dissipation [51] . (b) no synchronization needed but energy dissipation greater than or equal to energy barrier [50]. (c) the new stratergy proposed: no synchronization and arbitrarily small energy dissipation.

One scheme for switching between the states [50, 51] entails modulating the potential barrier between the wells periodically in time. As the barrier is gradually eroded, the symmetric double well profile is first tilted (fig 5.1(a)) towards the initial state to keep its potential energy constant. Just when the barrier is completely eroded and the well becomes monostable, it is translated horizontally in state space. The barrier then re-emerges on the opposite side of the well and therefore the system switches. This scheme results in vanishing dissipation because the system never acquires kinetic energy. However, it requires perfect timing synchronization between barrier modulation and the translation in order to switch accurately. That makes it fault-intolerant even in the absence of thermal noise.

The minimum stress for removing energy barrier of a single nanomagnet with 105nm~95nm~6nm dimension can be defined as critical stress σ_C and it can be estimated through the balancing of energy of shape anisotropy between the easy axis and hard axis with energy of stress anisotropy.

$$E_{Shape-Anistropy} \leq \mathrm{E}_{Stress-Anistropy}$$

$$\left| -\underbrace{\left(\frac{3}{2}\lambda_s \sigma_i \Omega\right)\sin^2\theta_i(t)\sin^2\phi_i(t)}_{E_{stress-anisotropy}} \right| \geq \left| E_{Shape}(\phi = 90^0) - E_{Shape}(\phi = 0^0) \right| \tag{5.1}$$

$$by\ consderation\ of\ \theta = 90^o\ \&\ \varphi = 90^o, 0^0 \Rightarrow \sigma_C = \left(\frac{\mu_0 M_s^2}{2}\right)\left|\frac{(N_{d-yy} - N_{d-xx})}{\frac{3}{2}\lambda_s}\right|$$

$$\sigma_C = 3.145MPa$$

Another scheme [50] that is dissipative but fault-tolerant is shown in Fig. 5.1(b). Here, the potential barrier is never modulated and hence no synchronization between two events is required.

Whenever switching is desired, the potential profile is tilted towards the desired well in such a way that the tilt is at least equal to the maximum barrier height. This ensures that the system will definitely switch to the desired well in the absence of noise, but the system now gains kinetic energy equal to the amount of tilt, which is dissipated when the system relaxes to the new ground state (desired well). Clearly, error-resilience has been purchased with dissipation – a trade-off that is well-known in the context of the Fredkin billiard ball model of computation [55].

5.2 Discussion

In this thesis, we propose a new scheme that captures the best of both worlds. The barrier is modulated in time, but an arbitrarily small tilt towards the final state is maintained in the potential profile *at all times* as shown in Fig. 5.1(c). When the barrier disappears, the system automatically tends to switch to the final state, which is the minimum energy state, with some probability *p*. We will show that at a finite temperature, the energy E_d dissipated in switching approaches ~$2kTln(1/p)$, based on equilibrium probability distribution prior to restoration of the barrier. The advantage of this (third) scheme over the first (dissipation less but error-prone) scheme is *error resilience without energy dissipation* at $T \to 0\,\mathrm{K}$, and the advantage over the second scheme (dissipative but error-resilient) is the much lower energy-dissipation ($E_d << E_{barrier}$) without any additional error vulnerability at $T \to 0\,\mathrm{K}$.

The third scheme that we propose here is also more practical to implement in nanomagnetic logic (NML) built with nanomagnetic binary switches [42] than the first. This is because NML chains consist of a linear array of nanomagnets where the first nanomagnet's state is propagated through all ensuing magnets by Bennett clocking [4]. Thus, the first magnet's state is set before the energy barrier separating the two stable states of the second magnet is modulated. Hence, the "tilt"

determined by the dipolar effect of the first magnet on the second magnet is fixed and cannot be varied synchronously with the raising/lowering of the barrier in the second magnet (see Fig.4. 2(b)).

In this thesis, we study this third scheme both in the absence (T =0K) and presence (T = 300 K) of thermal noise. The bistable switch chosen is a single-domain shape-anisotropic magnetostrictive nanomagnet shown in Fig 5.2(a) which is elastically coupled to a piezoelectric layer of thickness 40 nm, forming a 2-phase multiferroic. The magnetostrictive nanomagnet is shaped like an elliptical cylinder of dimensions ~ 105 nm × 95 nm × 5.8 nm. The two stable states of the magnetization vector are along the major axis of the ellipse which is the easy axis of magnetization.

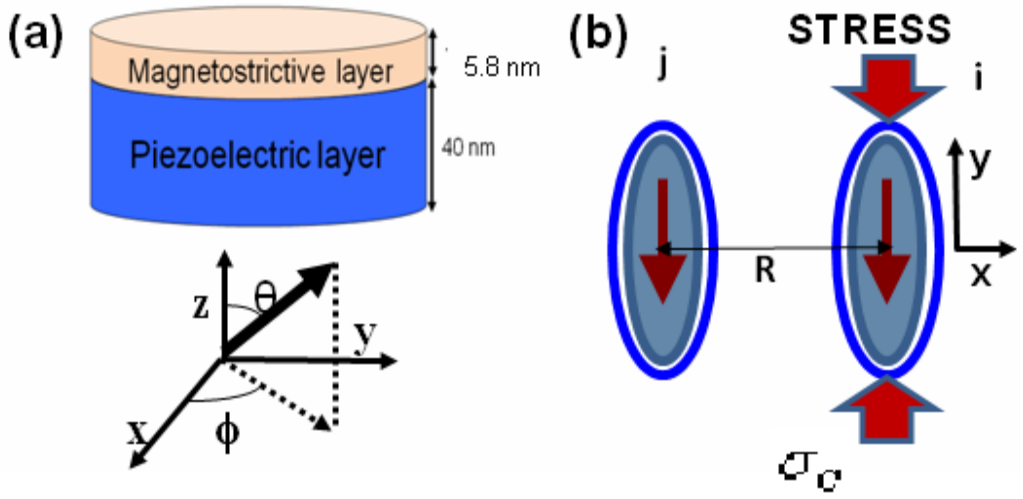

Fig5.2 **:** (a) An elliptical multiferroic nanomagnet consisting of a piezoelectric layer in intimate contact with a magnetostrictive layer. (b) A 2-magnet system comprising a hard magnet with large shape anisotropy and a soft multiferroic magnet with smaller shape anisotropy whose shape anisotropy energy barrier is modulated with stress.

Application of a voltage across the piezoelectric layer generates uniaxial mechanical stress along th axis via the d_{31} coupling in the piezoelectric material if mechanical clamps are placed on the magnet's prevent expansion/contraction along the minor axis. This uniaxial stress can rotate the magnetizatio provided the product of the magnet's magnetostrictive constant and stress (compressive stress is nega tensile positive) is negative. We will consider a 2-magnet system where the line joining their common aligned along the minor axis of the ellipse. This is shown in Fig.5.2(b). The dipole coupling betw magnets will favor anti-ferromagnetic ordering where the magnetizations of the two magnets will be r anti-parallel. Assume now that the *left magnet is a stiff magnet (larger shape anisotropy)* which is ma in the down direction. Also assume that an external agent had switched the magnetization of the right down, thus making the ordering temporarily ferromagnetic, which is an excited state.

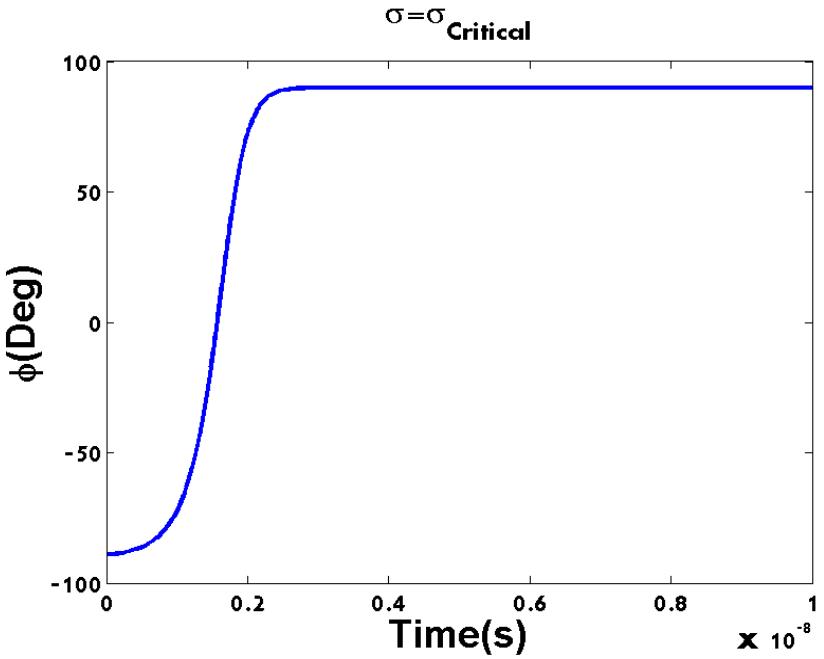

Fig 5.3. Dynamic behavior of a dipoled-nanomagnet under critical stress at T=0 (K).

One would expect that once the external agent is removed, the right magnet will spontaneously flip up to allow the system to relax to the ground state, but this may not happen. This is because the magnetization of the right magnet has to overcome an energy barrier caused by its own anisotropic shape before it can flip up. An applied uniaxial stress along the easy axis can depress the energy barrier and make the switching possible. Therefore, the right magnet is a physical embodiment of what is shown in Fig.5.1(c). The energy barrier between its two stable states (magnetization orientations "up" and "down") is provided by the shape anisotropy energy barrier which is modulated by stress, and the "tilt" is due to the dipole coupling caused by the left magnet.

The magnetization dynamics of the second magnet under stress is studied in the manner of Ref [5,6,11] (based on solution of the Landau-Lifshitz-Gilbert equation). When a critical stress of 3.145 MPa (induced by a voltage of only ~15 mV across the piezoelectric layer) is generated in the second magnet, the stress anisotropy energy equals the shape anisotropy energy barrier. At that point, the shape anisotropy energy barrier of ~ 0.75 eV separating the two stable magnetization states along the major axis of the ellipse is removed. Thus, at 0 K (or in the absence of thermal fluctuation), an arbitrarily small dipole interaction energy due to the first magnet, that tilts the potential profile of the second magnet barely, is sufficient to switch the second magnet to the desired state, given sufficient time (Fig 5.3).

The dynamic magnetization rotation of corresponding dipole coupled nanomagnets fig 5.2 under critical stress in the presence of thermal noise at room temperature T=300(K) is shown in fig 4.4. The magnetization does not get stuck at hard axis but rotates to the other easy axis as the stress anisotropy cancels the shape anisotropy and the dipole coupling helps the magnetization rotate completely. This shows the importance of applying a critical stress: the case for which we develop extensive analysis.

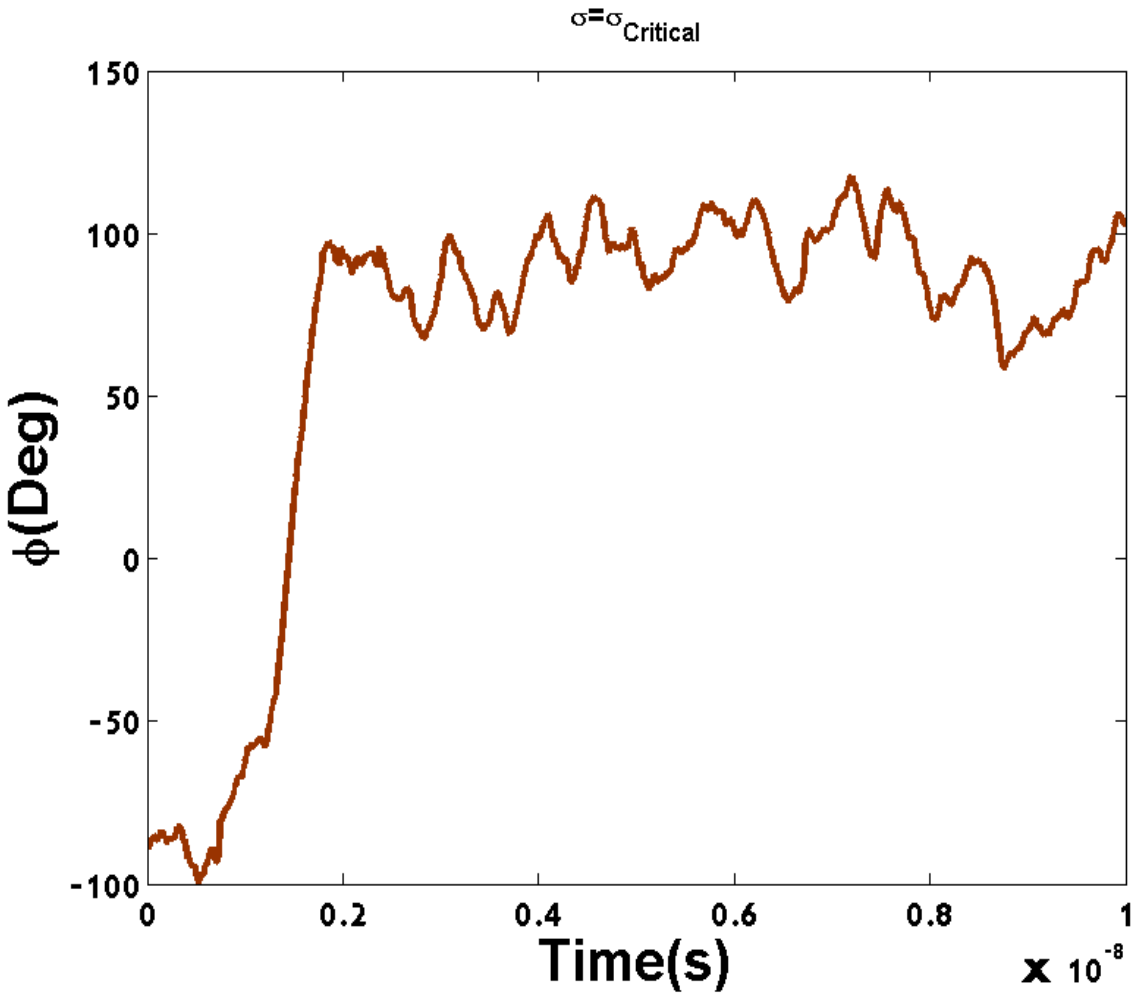

Fig 5.4. A dipole coupled nanomagnet where the magnetization rotates through 180 degrees to the correct state on applying stress close to critical stress.

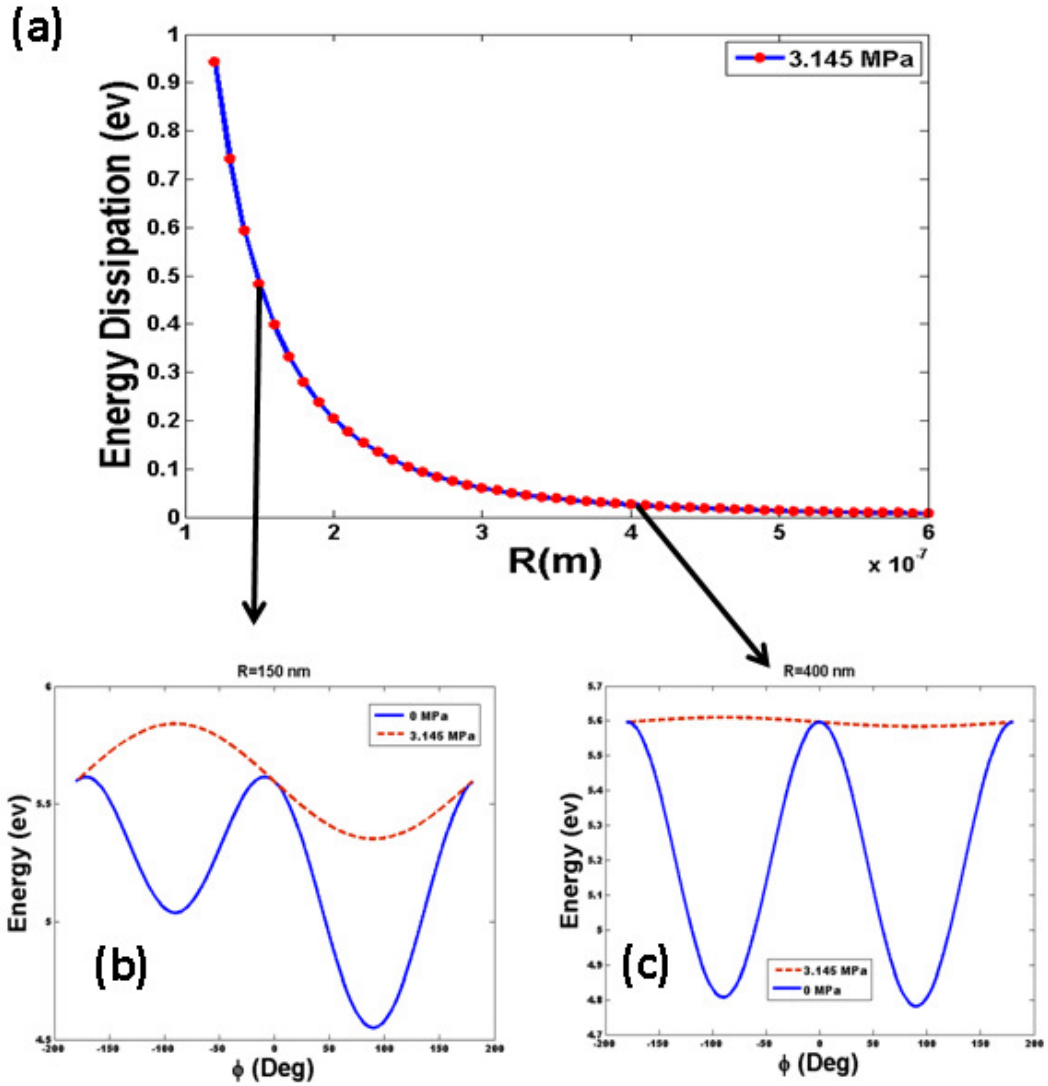

Fig 5.5(a) Energy dissipated in flipping (switching) the magnetization of the second nanomagnet as a function of the center-to-center separation between the two magnets (R). (b)The energy profile of the multiferroic nanomagnet discussed in the text in the relaxed (unstressed) state and the critically stressed state for large dipole coupling, R=150 nm (c) The energy profile of the multiferroic nanomagnet discussed in the text in the relaxed (unstressed) state and the critically stressed state for small dipole coupling, R=400 nm.

However, we first analyze the nanomagnet switching in the absence of thermal noise. Consider the potential energy profiles as a function of its magnetization orientation for both high (Fig 5.5 (b) and low (Fig5.5(c)) dipole coupling. Consider the case when the center-to-center separation between the magnets is R=150 nm as shown in Fig 5.5 (a). This separation causes a tilt of ~0.5 eV in the potential profile. When the barrier between the two states ~0.75 eV is removed by applying the critical stress, the magnetization rotates towards the correct (Φ=90º) state favored by the dipole coupling or tilt. Thereafter, the barrier can be restored. The energy dissipated is ~0.5 eV, which equals the tilt and has been verified by solving the LLG equations equation 2.51 and estimating the energy dissipated through the Gilbert damping term equation 2.55. If the dipole coupling is decreased by increasing the distance to R=400 nm, the tilt is reduced to a mere ~ 0.02 eV as shown in Fig 5.5(c). Again when the ~0.75 eV barrier is removed the magnetization gradually moves closer towards the correct (Φ=90º) state in ~100 ns (can be viewed as equivalent to a ball that would gradually move down a gentle slope). Again, the barrier can be restored but the energy dissipated this time is a mere ~0.02 eV (equal to the tilt).

Thus, in the absence of thermal fluctuations, the tilt and the resulting energy dissipation can be made vanishingly small, and yet switching always takes place without requiring any synchronization between the barrier modulation and the initiation of the tilt. It should be noted that raising and lowering the barrier does not dissipate any energy as this can be done with an adiabatic scheme as discussed in ref [6]. It is also critical to apply no more than the critical stress so that the barrier is just removed (see Fig 5.4). The reason for this is that the barrier needs to be "eroded", but not "inverted". If the barrier is inverted to create a monostable state, energy would be

dissipated in the process of the magnetization reaching this state during lowering of the barrier, and this dissipation is unnecessary.

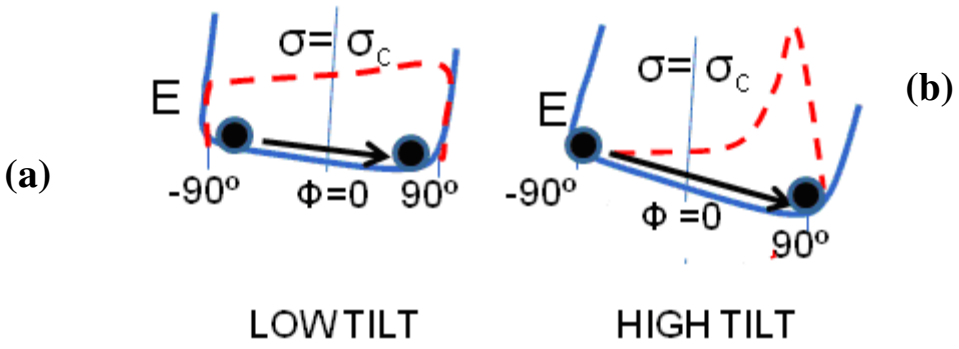

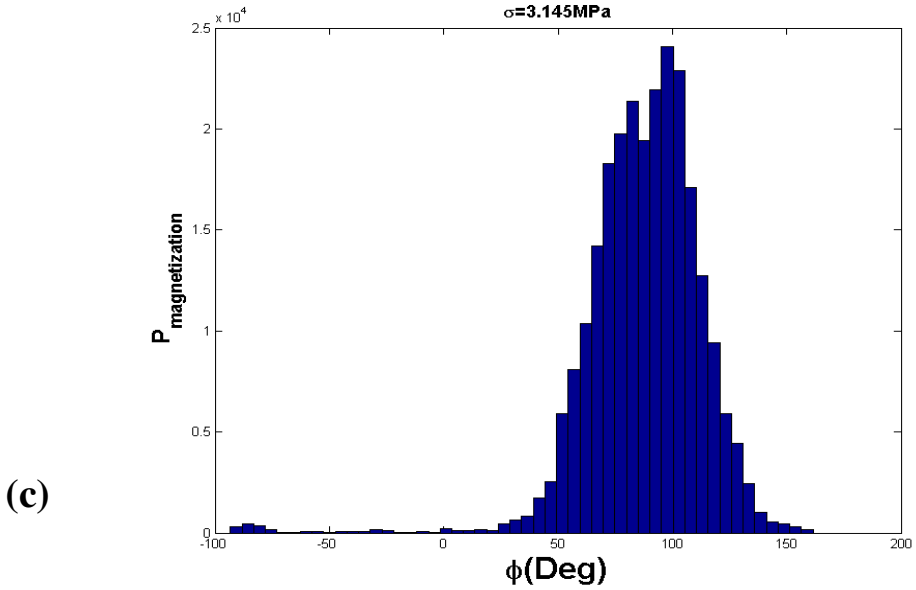

Fig 5.6 (a,b) Schematic that shows the effect of dipole coupling (tilt/asymmetry) and stress on the dynamic switching error. Energy profiles for critical stress for both low and high dipole coupling (tilt) are shown. Blue thick line: energy profile, red dotted line: corresponding probability distribution function. (c) Histogram graph of dipole magnet under critical stress at presence of room temperature thermal noise.

Next, we consider the trade-off between energy dissipated and dynamic switching error probability in the presence of thermal fluctuation at room temperature as depicted in Fig 5.6 for the

optimum case when $\sigma = \sigma_C$. We can derive an analytical relationship between $E_d$and theerror probability p under the following assumptions:

(i) The E vs. Φ is linear when critical stress is applied (this assumption is relaxed later to incorporate a sinusoidal profile as the dipole effect contains a sin(Φ) term which does not yield a closed form solution for relations between $E_{dissipated}$ and p_{error})

(ii) We apply the peak stress for long enough that it can be assumed that an equilibrium distribution (Boltzmann) is reached prior to withdrawal of stress. We further consider distribution Φ only and not (θ, Φ) as we assume the moments at equilibrium are mostly in-plane

(iii) We assume that when the stress is withdrawn suddenly (barrier restored) magnetizations that were in the [-pi/2, 0] half would settle to the "down" state while those in the [0, pi/2] half would settle to the "up" state. Extensive LLG analysis with thermal noise could show that dynamic effects in restoring the barrier typically increase the P_{error} compared that estimated from this distribution.) Nevertheless, this gives an estimate of the "minimum" energy that must be dissipated to limit the P_{error} to a certain value. Thus, the value of this analysis is to estimate a lower bound for energy dissipation which is certainly larger than the Landauer limit of kT ln(2) [52] where complex modulations of the barrier are permitted.

CASE I Now assuming that the energy of the down state (Φ = - 90^0) is E_1 and that of the up state (Φ = +90^0) is E_2, ($E_1 > E_2$) and linear variation in E with Φ, one can write the probability distribution function in Φ-space (assuming Boltzmann statistics) as:

$$\rho(\Phi) = Ae^{-\frac{(E_1-E_2)[\frac{\pi}{2}-\Phi]}{\pi kT}} \text{ where } A = \frac{(E_1-E_2)}{kTL}\left(\frac{1}{e^{(E_1-E_2)/kT}-1}\right) \tag{5.2}$$

The probability that the magnetization is oriented between Φ = -90^0 and 0^0, just before the barrier is raised, is the error probability p and can be found as:

$$p = \int_{-\pi/2}^{0} \rho(\Phi)\, d\Phi = \frac{e^{\frac{(E_{diss})}{2kT}} - 1}{e^{\frac{(E_{diss})}{kT}} - 1} \approx e^{\frac{-(E_{diss})}{2kT}} \quad \text{for } E_{diss} \geq 4kT \tag{5.3}$$

where the energy dissipated is given by

$$E_{diss} = E_{tilt} = E_1 - E_2 \tag{5.4}$$

equation (5.2) can be recast as:

$$E_{diss} \approx 2kT \ln(1/p) \tag{5.5}$$

Some of these issues of trade-off between dissipation and error probability were discussed in ref. [38, 56], but without deriving any analytical expression of the energy dissipated as a function of error probability by looking at magnetization distributions over phi-space**.** We also differ from Ref 16 as we do not allow any energy recovery scheme.

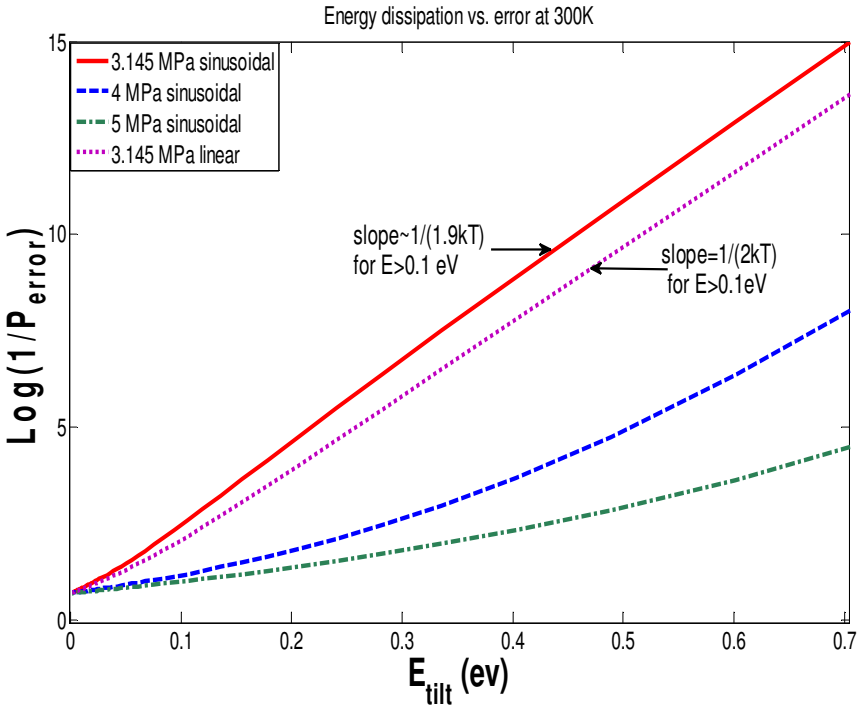

Fig 5.7.The Energy dissipated (energy of tilt) vs. static dynamic switching error for both case I and case II at critical stress and higher stresses.

Note that equation (5.5) is also counter-intuitive. Intuitively, one would expect that if Boltzmann statistics holds, then the relative probability of being in state E_1(wrong state) with respect to E_2 (correct state) would be $e^{\frac{-(E_1-E_2)}{kT}}$ and hence the *static* error probability would be $e^{\frac{-(E_1-E_2)}{kT}}$ [54, 56] which would result in $E_{diss} = E_1 - E_2 = E_{tilt} = kT\ln\left(1/p_{static}\right)$. Equating this with equation (4.5), we get that $p = \sqrt{p_{static}}$ when we switch with critical stress.

CASE II

Here we incorporate a sinusoidal profile as the dipole effect contains a sin(Φ) term. This represents a realistic energy profile for a multiferroic nanomagnet that is critically stressed so that the stress anisotropy exactly cancels the shape anisotropy. The probability distribution is now $\rho(\Phi) = Ae^{\frac{0.5(E_1-E_2)\sin(\phi)}{kT}}$ and has to be numerically integrated to find A and P_{error} unlike CASE I where an analytical result exists. When $\log(1/P_{error})$ is plotted against $E_{dissipated} = E_{tilt}$ (See Fig 5.2(b)) it can be approximated by an analytical result that for E>0.1 eV (or 4 kT at room temperature)

$$\Delta E_{dissipated}/\Delta \ln(1/P_{error}) = 1.9\ kT \quad (4.6)$$

This estimate is slightly less conservative than (5.5).

CASE III

Finally, we study the energy dissipation vs. dynamic error in a model nanomagnetic system shown in Fig 5.2 (b) by treating the second nanomagnet as a macro-spin. We run extensive stochastic LLG analysis in the presence of thermal noise in the manner of Ref [59], by incorporating a random field due to thermal noise in the effective field term. The results of this simulation are summarized in Fig5.8 where the $E_{dissipation}$ vs. P_{error} is compared to the analytical estimate.

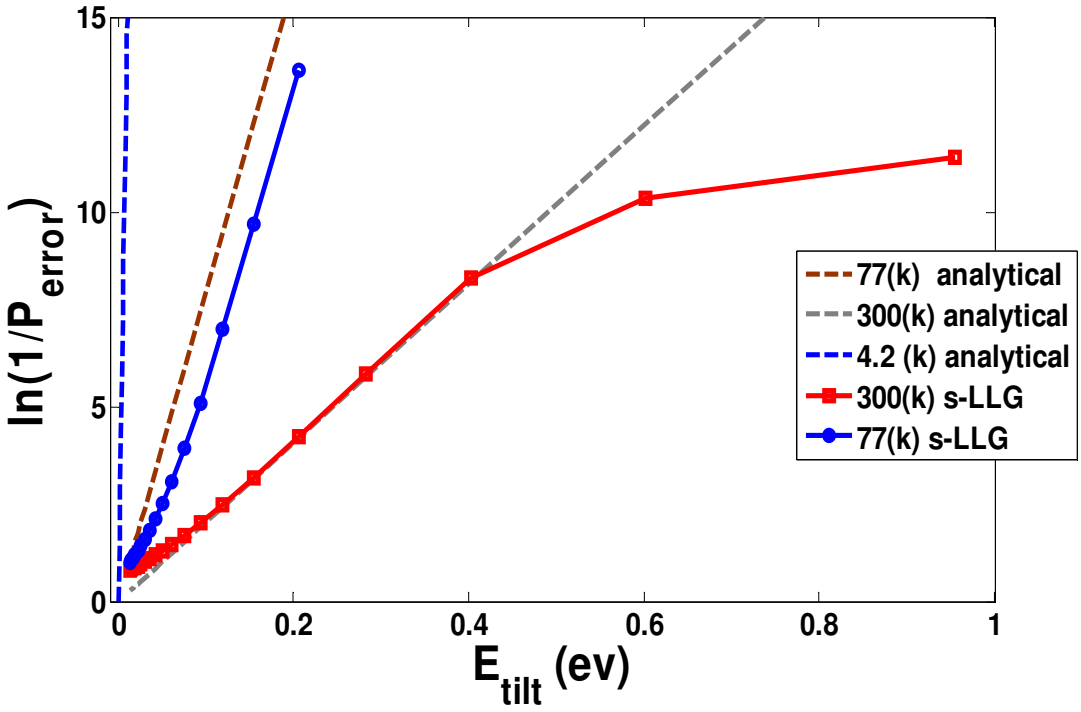

Fig. 5.8 Dynamics and analytical error probability are compared for different energy of tilt(energy dissipation) at the helium, nitrogen and room temperature.

The 3-D magnetization dynamics model typically shows higher $p_{error}$for given $E_{dissipation}$ but the extent of deviation is more for high $E_{dissipation}$(or low p_{error}). This is due to the out-of-plane distribution of magnetization as shown in Fig 5.9 where being above the plane can help the switching while being below the plane can hurt the switching by producing a precessional torque that that drives the magnetization to the wrong state. Clearly as the temperature increases, the out-of-plane distribution is more significant (large angles) and hence the switching error deviates from

the analytical result (trend in decrease in P_{error} with $E_{dissipation}$ saturates) at high values of P_{error}. The in-plane and out-plane magnetization distributions just prior to restoring the barrier (withdrawal of stress) are discussed.

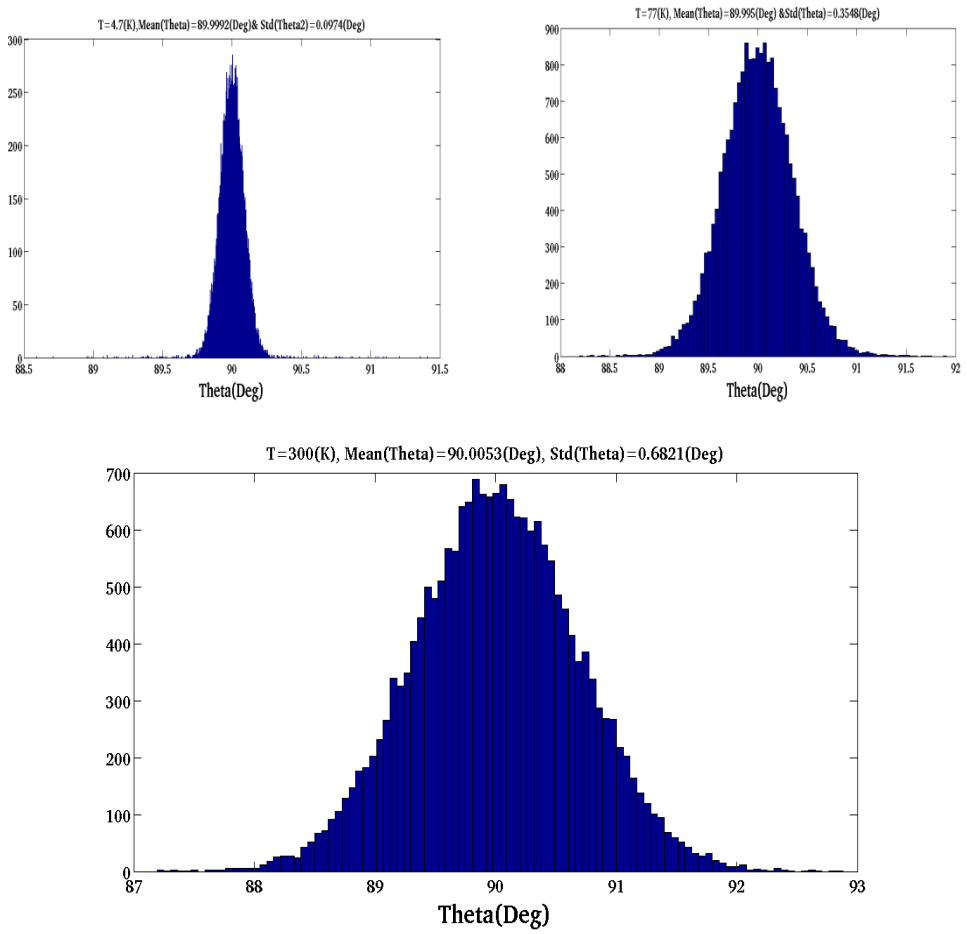

Fig 5.9. Schematic histogram of out off plane distribution for different temperature.

5.3 Conclusions

In this section, we have shown with a concrete example that in the absence of thermal fluctuations, we can switch a binary switch with 100% probability and arbitrarily small energy. When thermal fluctuations are present, there is a trade-off between energy dissipated and the dynamic switching error probability in this scheme. For a special case of switching a multiferroic magnet with critical stress, we have derived an analytical relationship between energy dissipated and the dynamic probability. We emphasize that for a practical logic switch *the minimum bound* for energy dissipated scales as ~$2kT \ln(1/p_{error})$ and can therefore be larger than the Landauer limit of $kT \ln(2)$ [52] where complex modulations of the barrier are permitted. We note even this is only a minimum bound and dynamic effects while raising the barrier and out-of-plane spread in magnetization can result in larger $E_{dissipation}$ requirement for a given $P_{error.}$

Chapter 6

Magnetization Dynamics with Surface Acoustic Waves (SAWs)

6.1 Overview

The control of the magnetization orientation in magnetostrictive materials using surface acoustic waves (SAWs) is of great interest not only from a fundamental point of view but also for potential applications in computing technology. In this chapter, the state of the art in theoretical work in the field of magnetization dynamics with SAWs is described, with emphasis on the dynamics (time evaluation) of magnetization in nanostructures strained by SAWs. The analysis of magnetization dynamics, transferring binary information in dipole coupled nanomagnets and nanomagnetic computation with NAND gates implemented with magnetostrictive nanostructures clocked with surface acoustic waves is developed and discussed in this chapter.

6.2 Introduction

The triggering of magnetization dynamics using surface acoustic waves (SAWs) can implement a low power dissipation switching methodology while reducing the burden of lithographic contacts to each nanomagnetic structure. However, the use of this method for nanomagnetic logic has remained largely unexplored.

The interface between strain and magnetization would be maximized when elastic and magnetic resonance frequencies match each other **[62]**. The excitation of spin wave modes in a (Ga, Mn)As

layer by picosecond strain pulse is studied by [63] in order to figure out dependence of the amplitudes of the excited spin waves on the clocking field and, consequently, on its frequency. They found that if the strain spectrum peaks be in range of 20-30 (GHz), it would be inefficient to trigger magnetization precession, which is normally in range of 0.5-10 (GHz). Surface acoustic waves (SAWs) in the low frequency range (<2GHz) has been explored for the elastic excitation and detection of ferromagnetic resonance in a ferromagnetic-ferroelectric (Ni/LiNbO3) device in [64]. The authors showed that SAWs can drive magnetization precession in thin Ni films. Also, the periodical magnetization switching between hard and easy axis of Co bars with SAWs have been studied in[65]. In high magnetostrictive material (Terfenol-D), it has been shown that a few picoseconds long acoustic pulse can reverse in plane magnetization of Terfenol-D [66]. In addition, an analytical and numerical approach was recently explored to pinpoint the perpendicular irreversible magnetization switching of Terfenol-D layer with a combination of two mechanism (i) small in-plane field and (ii) passage of SAW in order to trigger the magnetostrictive layer [67].

To excite and detect SAWs, interdigitated transducers (IDTs) are needed and just by applying few voltages to the comb of IDTs, SAWs would be produced that can potentially rotate the magnetization of magnetostrictive nanomagnets described in this work. The SAWs also have other advantages compared to picosecond acoustics pulse [67]: (i) low frequencies, and (ii) narrow bandwidth of surface acoustic wave.

In this work we numerically investigate the interaction of SAWs with in-plane nanomagnetic arrays of Terfenol-D ($Tb_x Dy_{1-x} Fe_2$) in order to show that the nanomagnetic devices such as nanomagnetic NAND gate can be clocked with SAWs provided their propagation speed is appropriately reduced. The simulation will be discussed by solving Landau-Lifshitz-Gilbert (LLG) equation in the manner described in chapter 3. The dipole coupling terms are written as follows:

$$E_{dipole-dipole}^{i-j}(t)=\frac{\mu_0 M_s^{\,2}\Omega^2}{4\pi\,|\,\vec{r}_{i-j}\,|^3}\left[\left(\vec{m}_i(t).\vec{m}_j(t)\right)-\frac{3}{|\,\vec{r}_{i-j}\,|^2}\left(\vec{m}_i(t).\vec{r}_{i-j}\right)\left(\vec{m}_j(t).\vec{r}_{i-j}\right)\right] \tag{6.1}$$

If the line joining the centers subtends an angle γ with their hard axes, the dipole coupling energy would be as:

$$\sum_{j\neq i}E_{dipole-dipole}^{i-j}(t)=\frac{\mu_0 M_s^2\Omega^2}{4\pi r^3}\sum_{j\neq i}\begin{bmatrix}\left(\sin\theta_i(t)\cos\phi_i(t)\right)\left(\sin\theta_j(t)\cos\phi_j(t)\right)\left(-2(\cos\gamma)^2+(\sin\gamma)^2\right)\\+\left(\sin\theta_i(t)\sin\phi_i(t)\right)\left(\sin\theta_j(t)\sin\phi_j(t)\right)\left(-2(\sin\gamma)^2+(\cos\gamma)^2\right)\\+\left\{\left(\sin\theta_i(t)\cos\phi_i(t)\right)\left(\sin\theta_j(t)\sin\phi_j(t)\right)+\left(\sin\theta_j(t)\cos\phi_j(t)\right)\left(\sin\theta_i(t)\sin\phi_i(t)\right)\right\}\\\times\left(-3\sin\gamma\cos\gamma\right)+\cos\theta_i(t)\cos\theta_j(t)\end{bmatrix} \tag{6.2}$$

where *r* is the separation between their centers.

We have studied the magnetization dynamics of a multiferroic logic chain with nearest neighbor dipole coupling using the Landau-Lifshitz-Gilbert (LLG) [28]:

$$\frac{d\vec{M}(t)}{dt}=-\gamma\vec{M}(t)\times\vec{H}_{eff}(t)-\frac{\alpha\gamma}{M_s}\left[\vec{M}(t)\times\left(\vec{M}(t)\times\vec{H}_{eff}(t)\right)\right] \tag{6.3}$$

We use Runge-Kutta method to solve the system of coupled differential equations in equations (6.3) for the linear chain of (i) coupled nanomagnets and (ii) NAND gate clocked with SAWs. All elements are shown in Fig 6.1, and Fig 6.2. The solution yields the orientation, $\phi_i(t),\theta_i(t)$ of the magnetization vector in any multiferroic element in the chain at any instant of time*(t)*.

6.3 Results

Fig 6.1.a shows a schematic view of a dipole coupled ferromagnetic (parallel magnetic orientation) nanomagnetic logic wire, in which we consider magnet#1 as a stiff input that SAW's strain would not be able to rotate it. So, by applying four-phase sinusoidal stress of 10 MPa with T= 1.5 ns and the center to center of nanomagnet is about 120 nm separation, we intend to simulate nanomagnets behavior with SAWs clocking the magnets. By solving coupled LLG equations for magnet 1to 4,

the time evolution of the magnetization orientation of nanomagnets in this system can be simulated as it is shown in Fig 6.1.b. It can be seen that each nanomagnet switches 90(Deg) in just 0.5(ns) and the total rotation from the "down" easy axis to the "up" easy axis just takes 1(ns) or the frequency of system is about 1(GHz). We consider T/4 delay in phase of applying stress for magnet #2 to 4 in order to simulating the SAW's delay in reaching each nanomagnet. Our simulation shows that if lower stress is applied to this system of ferromagnetic coupled nanomagnets at 0.66 (GHz) frequency, the information does not propagate along the chain. Thus, higher frequencies require more stress to implement successful propagation of information as the magnetization has less time to rotate from the easy to the hard axis. In this work the strain in z direction ε_{ZZ} is neglected and only strains in-plane strains are considered.

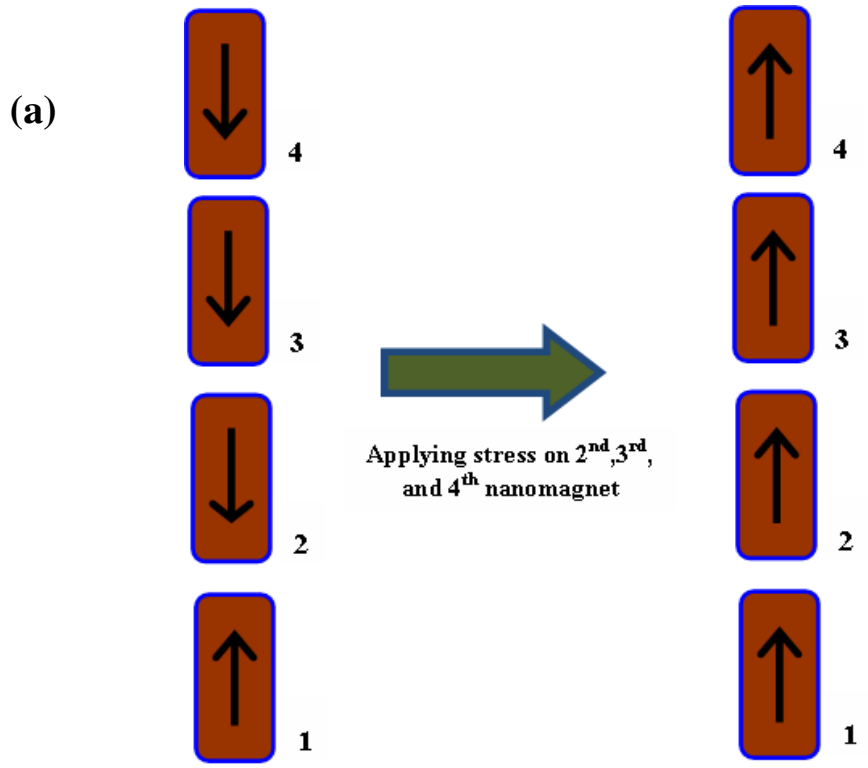

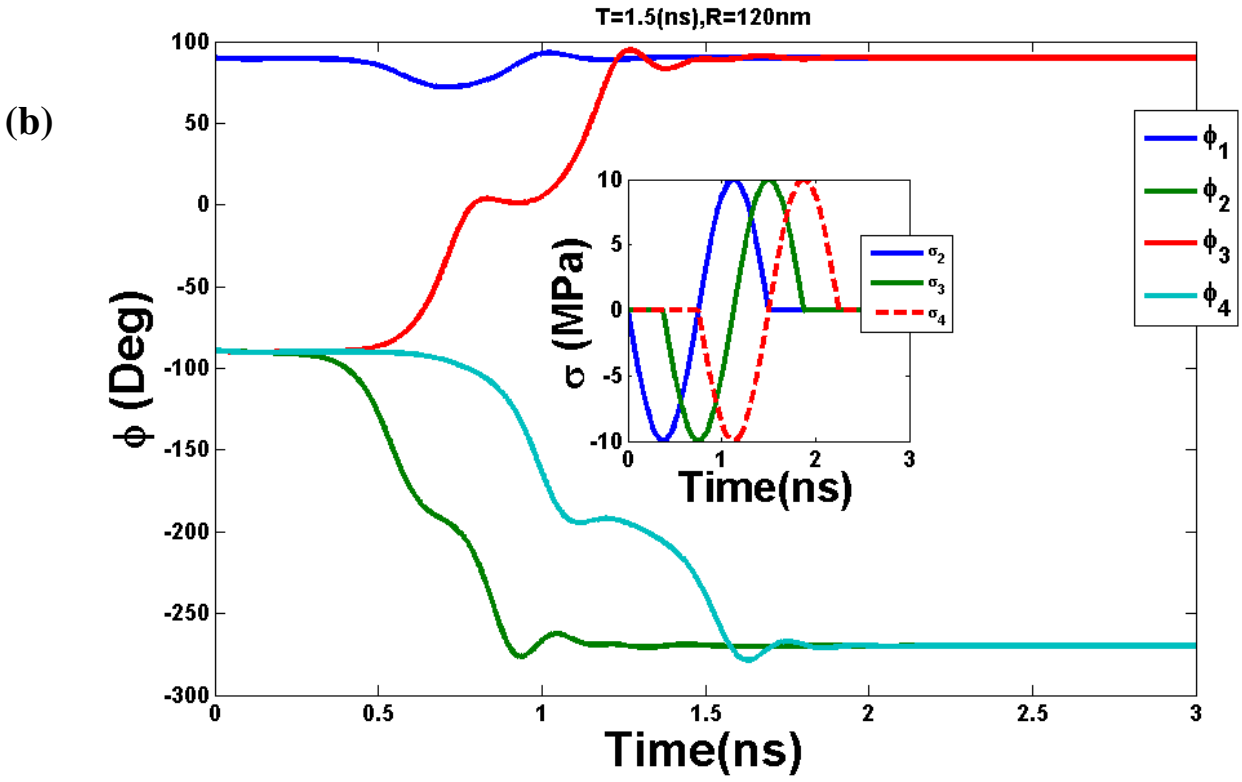

Fig.6.1 (a) A ferromagnetic logic chain with stiff input (Magnet#1).(b) A four-phase sinusoidal stress with T=1.5 ns have been applied to magnet#2 to 4 in order to eroding the shape anisotropy energy barrier of magnets and due to dipole coupling, all nanomagnet tend line up with the magnetization parallel to input after the SAW waves passes sequentially through them.

Next, the schematic configuration of a NAND gate amenable to clocking with SAW waves is shown in Fig 6.2. It is composed of eight nanomagnets, which include Input-1 and Input-2, NAND gate elements and output. Nanomagnets are categorized in different groups of I, II, III and IV as the SAWs reach all elements of a specific group simultaneously and trigger magnetization rotation in each element of that specific group at the same time. In order to implement clocking with SAW waves the NAND gate has to be designed so that no group of neighboring elements are in one vertical line or perpendicular to the direction of propagation of the SAW wave as this is not amenable to sequential clocking of nanomagnets with a SAW wave. Furthermore, the NAND design in Fig 6.3 has a set of magnets that follow input-1 which are all in a horizontal row while

magnets that follow input-2 are at 45 degrees to the horizontal. Such a geometry may be useful for implementing elements such a flip-flops where one of the input is basically the output fed back and cannot be in a nice horizontal line. A four-phase sinusoidal stress has also been applied to simulate SAWs with a stress magnitude of 15(MPa) and time period of T=1.5(ns). The 90 degree phase between each group of magnets clocked has to be achieved due to the path delay in the SAW wave travelling from one group to the next. We assume the velocities that are needed to achieve this may be obtained along specific orientations of the piezoelectric crystal or adding periodic barriers that slow the propagation velocity of the SAW wave. The bias magnetic field of -300(A/m) is also applied on magnet#4 to resolve the "tie" cases when the inputs are different from each other (i.e. the two inputs are "0" and "1" or vice versa) . Finally, the NAND gate behavior has been verified for various input cases in Fig 6.3 a-d.

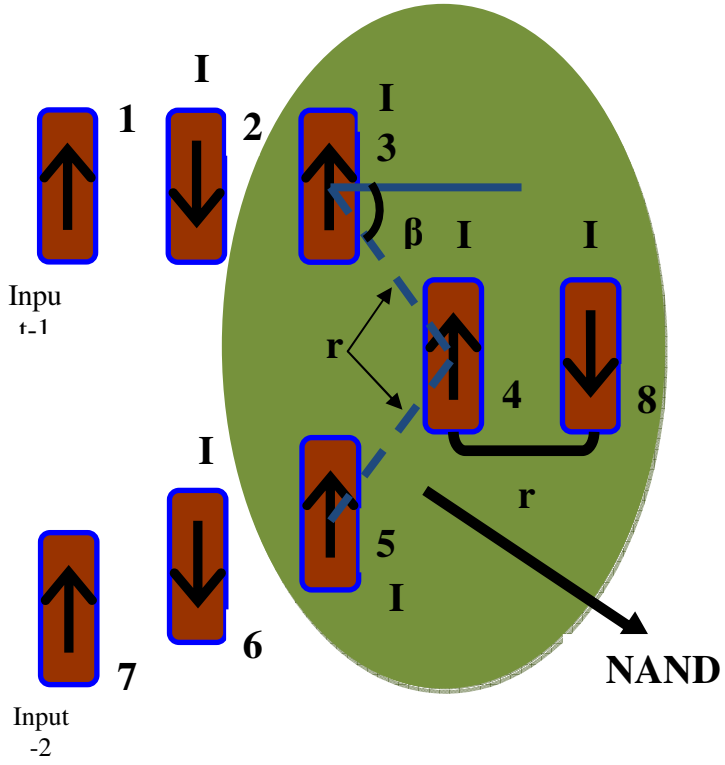

Fig. 6.2 Schematic view of computational Nand gate configuration under triggering of SAWs.

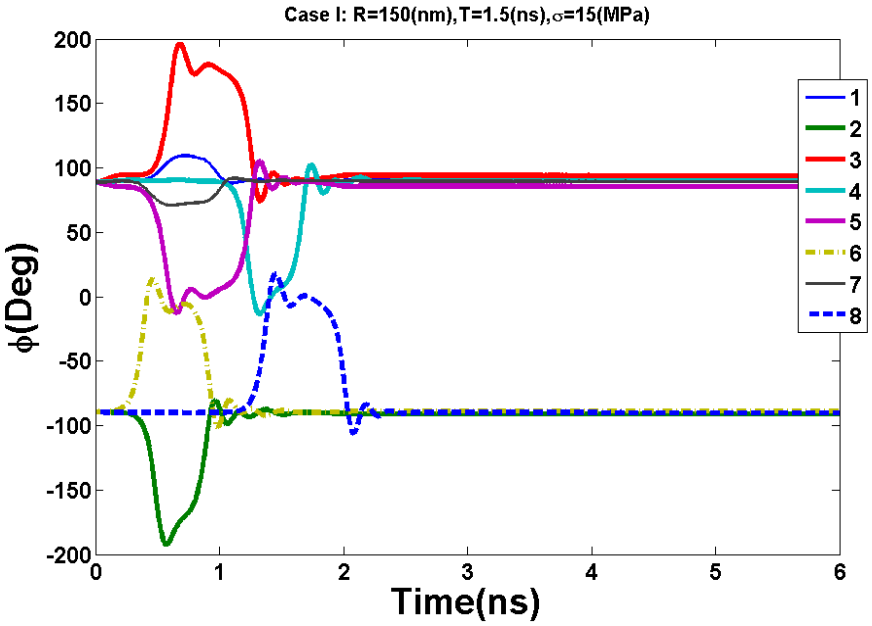

Fig6.3.a . Case I, computational nand gate under passing SAWs with "1"&"1" Inputs and "0" output.

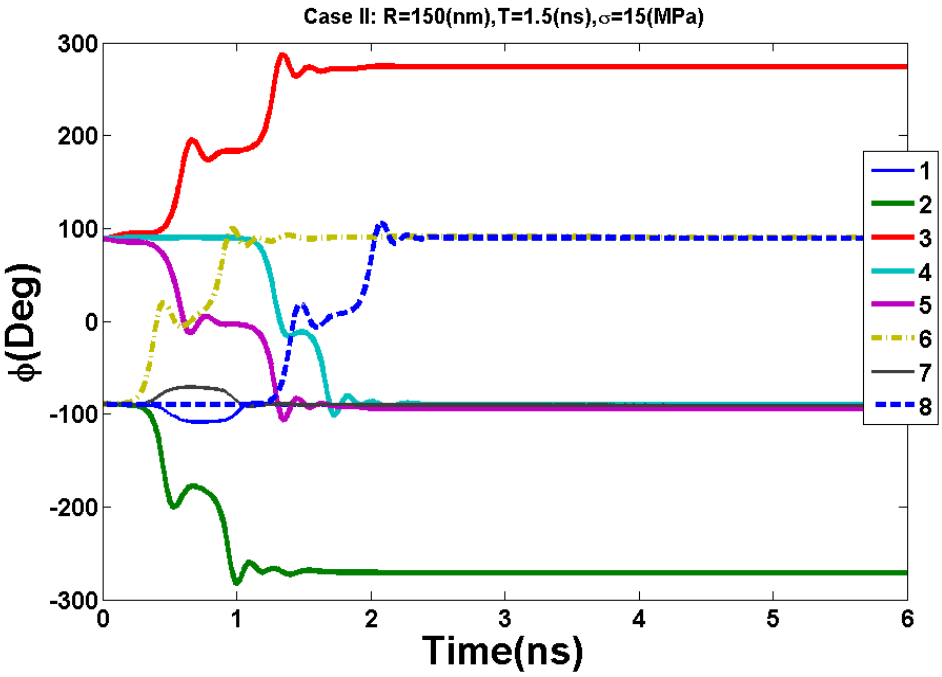

Fig 6.3.b. Show case II as inputs "1" & "1" and output"0".

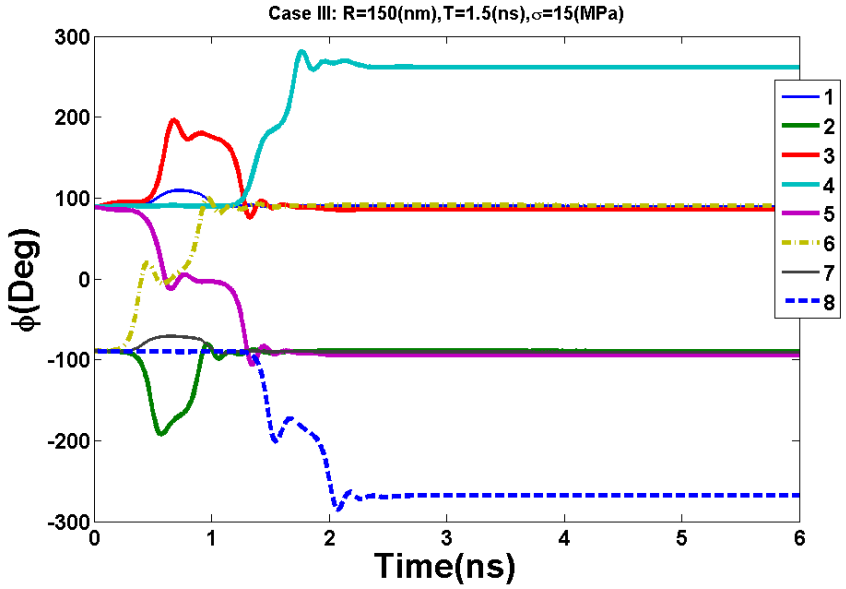

Fig 6.3.c .Input-1 and Input-2 as "1" and "0", the fast SAW do correct computation as output of "1".

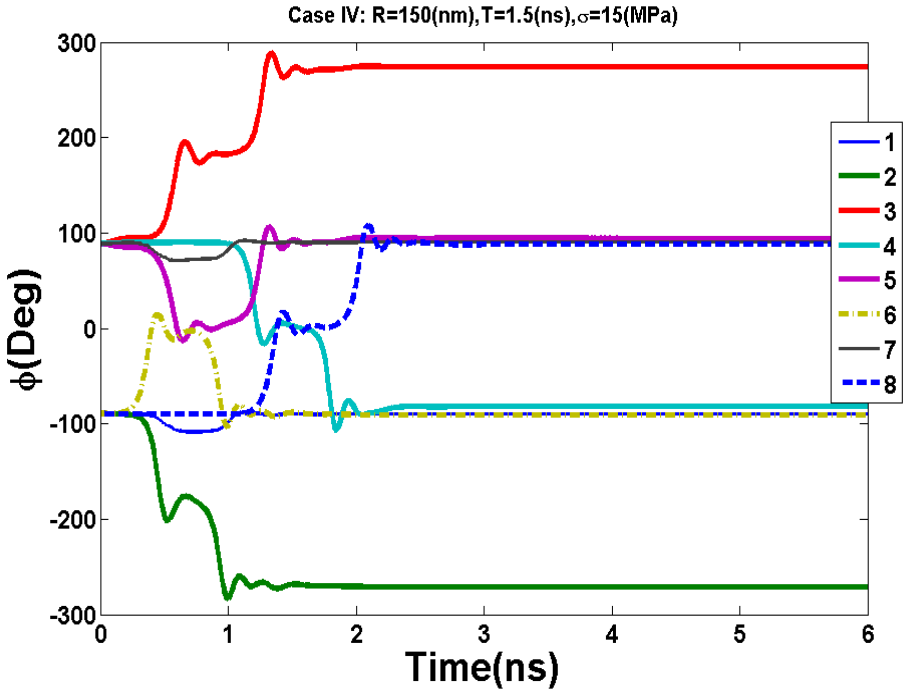

Fig 6.3.d. shows magnetic time evaluation of NAND gate with inputs "1" &"0" and output "1".

6.4 Conclusion

In summary, we have shown that it is possible to design universal nanomagnetic logic gates and logic wires that can be clocked with SAW waves. This technique retains the pipelining and energy efficiency of strain clocked nanomagnetic logic devices while at the same time drastically decreasing the lithographic burden that is needed to contact each multiferroic nanomagnet in order to be able to clock them sequentially to propagate information and perform computations. Specifically, we design a NAND gate where no group of neighboring elements are in one vertical line or perpendicular to the direction of propagation of the SAW wave. This design is amenable to sequential clocking of nanomagnets with a SAW wave. However, it is important to note that the SAW wave propagation velocities that are needed to allow sufficient time for clocking each nanomagnets may only be achieved along specific orientations of the piezoelectric crystal or possibly by adding periodic barriers that slow the propagation velocity of the SAW wave.

Chapter 7

Implementation of 4-state nanomagnetic devices with shape anisotropy

7.1 Overview

Nanomagnetic logic (NML) is currently seen as a promising candidate for digital computing architectures since it offers both energy-efficiency and non-volatility, thereby, making it extremely attractive for highly dense, low-power applications. In this work, we investigate the use of shape engineering to introduce biaxial anisotropy in single domain nanomagnets. This gives rise to multiple easy and hard axes (four degenerate energy minima corresponding to four different magnetization orientation directions separated by at least ~ 1 eV energy). Such nanomagnets, with dimensions of ~ 100 × 100 nm, double the logic density of conventional two-state devices by encoding more information (4-states) per nanomagnet and can be used in memory and logic devices as well as in higher order information processing applications. We study the magnetization switching coherence (as a single-domain or macro-spin state) in these nanomagnets with three-dimensional (3-D) micromagnetic simulations using Object Oriented Micro Magnetic Framework (OOMMF) and examine the extent to which parameters such as size, thickness, concavity, and geometry of the nanomagnet play a role in achieving reliable and coherent switching in these four-state magnetostrictive nanomagnets.

7.2 Introduction

The continued downscaling of conventional transistor-based electronics faces a challenging barrier in the form of increasing energy dissipation. In the quest for alternative paradigms, spin- and nanomagnet-based computing architectures [1,2,40 ,43,68]have emerged as promising candidates. Unlike transistor-based devices, nanomagnets experience a correlated switching of spins [3]and do not suffer from leakage currents. As a result, these methodologies suffer from no standby power dissipation and offer substantial benefits such as non-volatility, energy-efficiency, high integration density, CMOS-compatibility, and compact implementation of logic gates.

One of the most important properties of ferromagnetic materials is its magnetic anisotropy. This intrinsic property of magnetic materials plays an essential role in magnetoelectric applications such as permanent magnets, information storage media and magnetic recording heads, which require the magnetization to be pinned in a defined direction. In nanomagnets, the magnetic anisotropy also depends on the shape of the nanomagnet and its magnetic properties can be engineered by manipulating the shape of the nanomagnet, with different shapes giving rise to different anisotropic behaviors.

Basic shapes of nanomagnets, such as ellipsoid and rectangular (having uniaxial anisotropy and encoding two states) have attracted a lot of attention for its applications in ultra-low power binary logic [4,5,6,15,41]and non-volatile memory applications [7,8]. Nanomagnets encoding four states, instead of the conventional two-states, have been theoretically demonstrated to implement Boolean logic [9,70]. Besides increasing the logic density, this four-state scheme also holds promise for higher order computing applications such as associative memory, neuromorphic computing and image processing [10]. Since nanomagnetic logic devices require accurate propagation of magnetic information along dipole-couple nanomagnets, reliable switching behavior is paramount and has

been shown to be dependent on shape geometry, with different shapes and sizes playing an important role in the switching behaviour and correlation lengths along an array of nanomagnets [71]. In this work, we study switching coherence in four-state nanomagnets and investigate the effect of shape, size and thickness on the ability of the nanomagnets to switch their magnetization coherently.

A four-state memory element can be implemented with a magnetostrictive layer (for instance, single-crystal Ni), which would exhibit biaxial magnetocrystalline anisotropy in the (001) plane. Epitaxial films of single-crystal (001) Ni can be grown using molecular beam epitaxy (MBE) [72,73]. Biaxial anisotropy in magnetic thin-films has also been shown in single-crystal films [74], coupled films [75], double-layer films [76], as well as in a four-pointed star-shaped film [77], with the latter highlighting the relationship between shape-induced biaxial anisotropy and the geometry of a thin magnetic film element, indicating that in a four-pointed star-shaped film, the high-energy states occur when the average magnetization, $\vec{M}$, was oriented from tip to tip (along the long dimension), while the low-energy corresponds to $\vec{M}$ pointing diagonally (45°, along the short dimension).

Another technique used to modify a nanomagnet's magnetic anisotropy, similar to shape anisotropy, and termed 'configurational anisotropy', involves creating multiple "easy" axes by introducing small modifications to the uniformmagnetization of nanomagnets of a specific symmetric shape[78-80]. In experiments conducted by Lambson et al. [81], the effect of configurational anisotropy on the magnetic properties of triangular-, square- and pentagonal-shaped nanomagnets was studied. It was observed that by modifying parameters such as sample thickness and concavity of an indentation introduced along the edges, the magnitude and direction of the easy axes could be individually adjusted. Consequently, nanomagnetic logic devices requiring energy

efficiency and performance reliability could exploit the desirable features of this configurational anisotropy scheme, namely, anisotropy control and the ability to create multiple easy axes. In this study, Terfenol-D is chosen as the magnetostrictive material of our nanomagnets due to its high magnetostriction and magnetomechanical coupling constants, values that are instrumental for the realization of reliable and efficient four-state nanomagnets.

This section is organized as follows. In section 7.3,the theoretical framework for studying magnetization dynamics in four-state nanomagnets with configurational anisotropy is discussed. Section 7.4 examines and presents: (i) dynamic switching behavior in diamond- and concave-shaped nanomagnets using the micromagnetic simulation code, OOMMF [26], and (ii) the influence of various parameters such as size, thickness and concavity of the nanomagnets on single domain switching (coherent switching) while maintaining an energy barrier of ~1eV between the adjacent stable states.Section 7.5reviews the results in order to determine the best geometry of the nanomagnets for coherent switching and finally, in section 7.6, we present our conclusions.

7.3 Method: micro magnetic modeling

In our studies of shape-engineered four-state nanomagnets, two types of shapes are examined: (i) diamond, and (ii) concave nanomagnets (square nanomagnets with concave grooves in its sides). Nanomagnets with these shapes have been shown to possess a fourfold, symmetric anisotropy field [80, 15, 82]due to configurational anisotropy and also demonstrate different micromagnetic switching modes. The schematic of a four-state concave nanomagnet with its easy and hard axes is illustrated in Fig 7.1 .

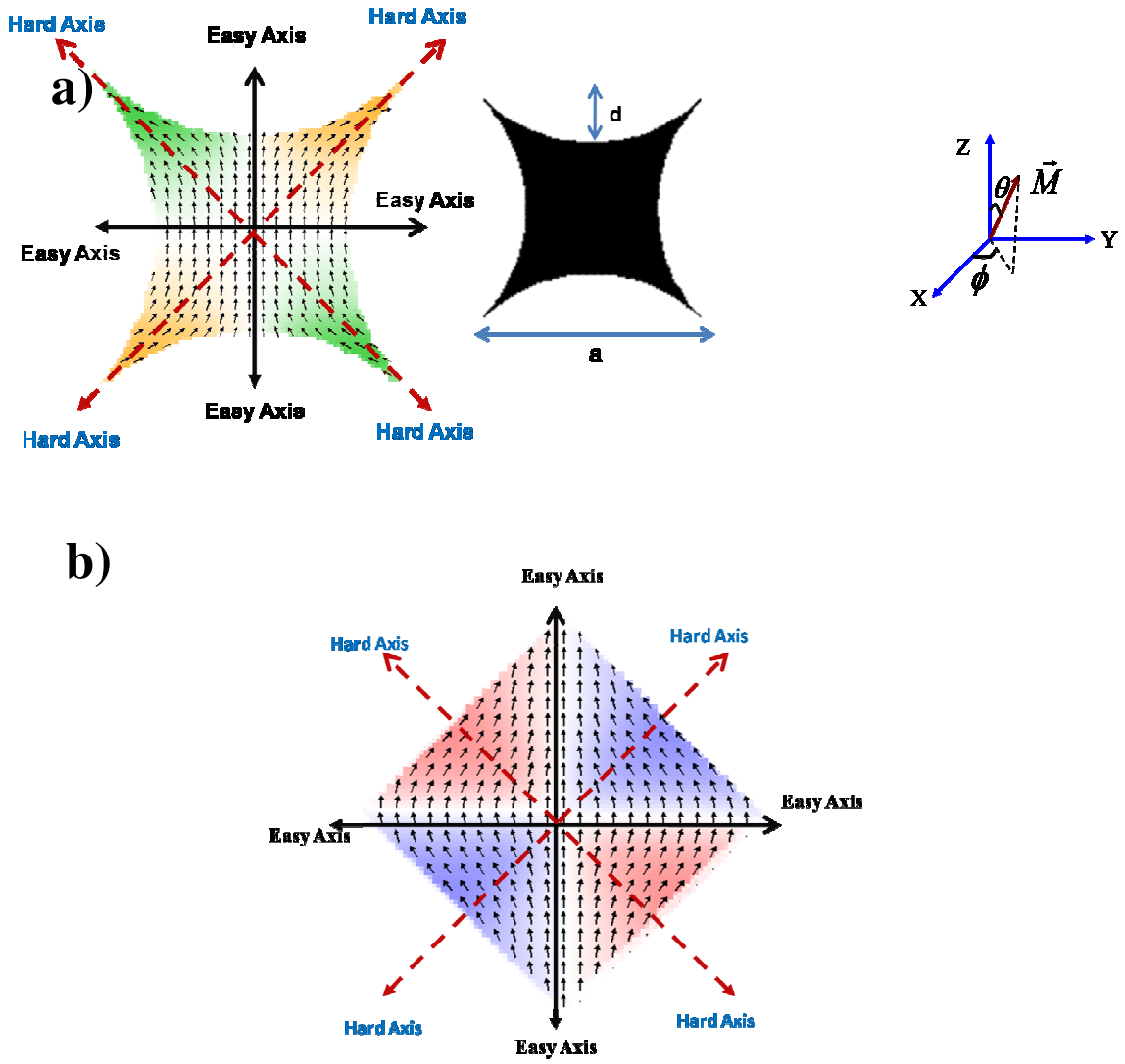

Figure 7.1. Four-state schematics showing the easy and hard axes of (a) concave-shaped nanomagnet with concavity, *d*, and lateral dimensions, *a*, and (b) diamond-shaped nanomagnet.

In the following sections, micromagnetic modeling is carried out based on the total Gibbs free energy of these two nanomagnet shapes. Simulations of the magnetization dynamics are performed using the Object Oriented MicroMagnetic Framework (OOMMF) software [26] in order to explore magnetization switching in these four-state diamond and concave nanomagnets. Micromagnetics is

a continuum theory used to describe the magnetization process within ferromagnetic materials. To study the behavior of these nanomagnets, it is necessary to consider the relevant energy terms such as the exchange energy, magnetocrystalline, magnetostatic anisotropy, stress anisotropy, and external magnetic field.

The total energy of these nanomagnets can be defined for a volume of Ω as:

$$U_i = \iiint_{\Omega} \{\underbrace{A[(\nabla m_x)^2 + (\nabla m_y)^2 + (\nabla m_z)^2]}_{E_{exchange}} \underbrace{-\frac{1}{2}\mu_0 \vec{H}_d . \vec{M}}_{E_{ms}} + \underbrace{[B_1(\alpha_1^2\varepsilon_{xx} + \alpha_2^2\varepsilon_{yy} + \alpha_3^2\varepsilon_{zz}) + B_2(\alpha_1\alpha_2\varepsilon_{xy} + \alpha_2\alpha_3\varepsilon_{yz} + \alpha_3\alpha_1\varepsilon_{zx})]}_{E_{me}} \underbrace{-\mu_0 \vec{M}.\vec{H}}_{E_{Zeeman}}\} d\Omega \quad (7.1)$$

in which the first term represents the exchange energy ($E_{exchange}$) having an exchange constant, A. The second term, E_{ms}, denotes the magnetostatic energy of the nanomagnet while E_{me} is the magnetoelastic energy of the magnetostrictive material having magnetoelastic coupling constants, B_i, and direction cosines, α_i, while experiencing a strain ε_{ij}. The final term, E_{Zeeman}, represents the energy of interaction with an external magnetic field, H.

In this work, the magnetocrystalline anisotropy is neglected as the sample is assumed to have random polycrystalline orientation. The detailed analytical expressions for exchange energy and shape anisotropy for fourfold square nanomagnets have been investigated with perturbation theory [83]. The magnetization dynamics of any nanomagnet under the influence of an effective field, $\vec{H}_{eff}$, is described by equation (2.43) the Landau-Lifshitz -Gilbert (LLG) equation [28].

In this equation, $\vec{H}_{eff}^{\,i}$ is the effective magnetic field as equation (2.33) on thenanomagnet, defined as the partial derivative of its total potential energy (U_i) with respect to its magnetization ($\vec{M}_i$), γ is the gyromagnetic ratio, M_s is the saturation magnetization of the magnetostrictive layer and α

is the Gilbert damping factor[45] associated with internal dissipation (equation 2.51) in the magnet owing to the magnetization dynamics.

The internal energy dissipated in a four-state nanomagnet during magnetization switching, E_d, can be described in equation 2.51 [28]:

To analyze the reversal process and time evaluation of magnetic moment in the four-state diamond and concave nanomagnets, three dimensional (3D) micromagnetic simulations were executed using OOMMF. These OOMMF simulations perform time integration of the PDE LLG equation, where the effective field includes the exchange, anisotropy, self-magnetostatic and external fields. The discredited cell size which used for modeling was 2 nm × 2 nm × 2 nm, implemented in the Cartesian coordinate system. The parameters used for the magnetostrictive nanomagnet (Terfenol-D) in the modeling are: exchange constant, $A = 9 \times 10^{-12}$ J m^{-1}[84], saturation magnetization, M_s = 800,000 A m^{-1}, anisotropy constant, $K_1 = 0(J.m^{-3})$ (no magnetocrystalline anisotropy), and damping coefficient, $\alpha = 0.1$.

7.4 Results

To realize reliable and efficient four-state nanomagnets, we study two different shapes: diamond and concave (shown in Fig 7.1). The magnetostrictive material of the four-state nanomagnets is chosen to be Terfenol-D due to its high magnetostriction constant. Here, we study the effects of magnetic fields on the switching characteristics of these nanomagnets. Stress-induced switching will be investigated in future studies. In this section, the following characteristics are examined: (i) magnetization hysteresis (anisotropy field) (ii) switching coherence, and (iii) magnetization dynamics, in order to determine the shape best suited for coherent and reliable switching for future four-state memory and logic applications as well as for higher-order applications such as image recovery and recognition schemes [9,70,10].

7.4.1. Nonlinear magnetization hysteresis and Anisotropy Field

In order to figure out the magnetization reversal process in the diamond and concave nanomagnets, micromagnetic simulations (OOMMF) were performed to verify its magnetization hysteresis. We study the hysteresis (m-B) loops of these nanomagnets for different thicknesses (10 nm and 15 nm) and lateral dimensions of 100 nm × 100 nm.

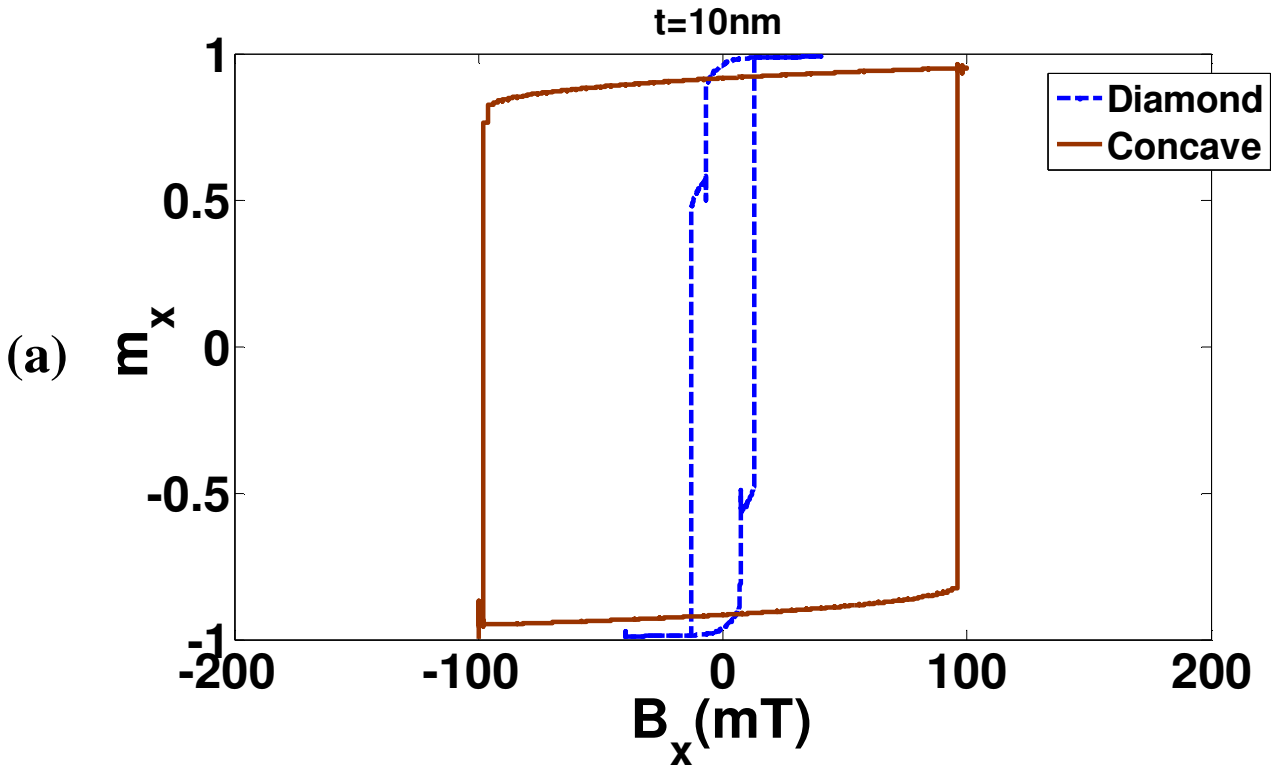

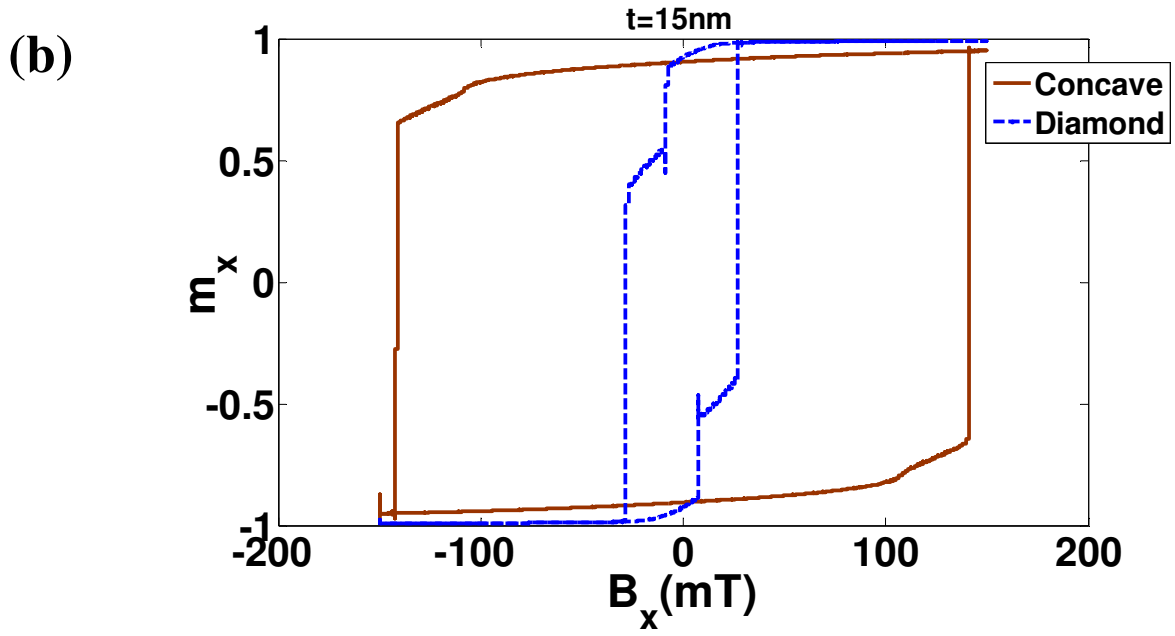

Figure 7.2. Magnetization hysteresis (m-B) curves for the concave and diamond nanomagnets with dimensions of 100 nm × 100 nm and having a thickness of (a) 10 nm, and (b) 15 nm.

The concavity depth, *d*, of the concave nanomagnet was chosen to be 20 nm. The results for both nanomagnets are shown in figure 7.2 which illustrates the normalized hysteresis loops for both shapes in the presence of an applied magnetic field along +*x* direction($\phi = 0^o$).

The switching field for the diamond magnet with a thickness of 10 nm is ~ 16 mT. However, for a concave nanomagnet with the same lateral dimensions and thickness but having a concavity depth, *d* = 20 nm, this field increases to ~ 96 mT (Fig 7.2). When repeated for a thickness of 15 nm, we observe a switching field of 27 mT for the diamond nanomagnet and 141 mT for the concave nanomagnet. Therefore, the introduction of concavity to the sides of the diamond nanomagnet results in an increase in the switching field by a factor of ~ 6. This increase in the energy barrier between the easy and hard axes is associated with the coherent magnetization switching in the concave nanomagnets as opposed to the diamond nanomagnets. This phenomenon can be attributed

to the configurational anisotropy introduced by the concavity in the sides of the nanomagnet and is described in the following sections.

The anisotropy field for both diamond and concave nanomagnets was examined next, with the magnetization of each nanomagnet initialized in the +*y* direction, followed by the application of a magnetic field along the +*x* direction. Increasing the magnitude of the field in the +*x* direction causes the magnetization of the magnets to rotate, from the initial 'up' direction to the 'right' direction once the external magnetic field overcomes the energy barrier of the nanomagnet. The value of this field (that causes a 90° magnetization rotation) is taken to be the anisotropy field of each nanomagnet. These simulations were performed for nanomagnets having the same lateral dimensions (100 nm × 100 nm) but different thickness and concavity depths, with the results illustrated in figure 7.3.

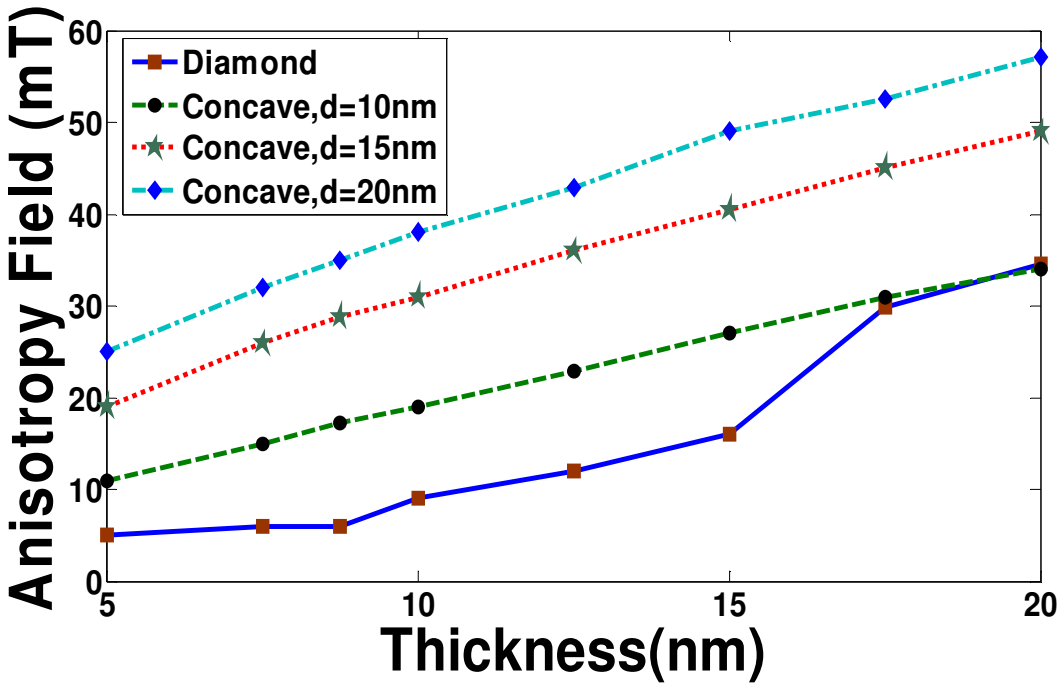

Fig7.3. Anisotropy field as a function of nanomagnet thickness for concave and diamond nanomagnets having lateral dimensions, a = 100 nm for different values of concavity, d.

For a diamond nanomagnet with a thickness of 7.5 nm, the anisotropy field is 6 mT. However, creating a concavity in its sides, with d = 10 nm, increases this anisotropy field to 15 mT, thereby increasing the energy barrier between the easy and hard axes by a factor of ~ 2.5. It is observed that the anisotropy field of the nanomagnets is sensitive to the thickness and concavity depth, with an increase in values of both parameters resulting in a corresponding increase in the anisotropy field.

It should be noted that increasing the thickness of the diamond magnet causes an increasing incoherence in its switching characteristics (resulting in the double-jump hysteresis loop [82]), but not in the concave nanomagnets. The trend of low energy barrier values for the diamond nanomagnet persists till a thickness of 20 nm, above which the diamond nanomagnet shows an anisotropy field higher than that of a concave nanomagnet having the same lateral dimensions (for d = 10 nm) and thickness, as can be seen in figure 7.3. However, this increase in anisotropy field comes at the expense of increased incoherence in its switching mode.

7.4.2 Switching modes in diamond- and concave-shaped nanomagnets

A single nanomagnet has two dominant and competing energy terms: (1) exchange energy, and (ii) anisotropy energy. In the previous section, it was shown that for higher thicknesses, the diamond nanomagnet shows a higher anisotropy field than that of a concave nanomagnet of similar dimensions (and concavity, d = 10 nm), at the expense of incoherent switching modes. Consequently, it is of interest to perform micromagnetic simulations using OOMMF and examine the evolution of this incoherence, from single-domain to incoherent vortex modes, in the diamond nanomagnet for different values of thickness as compared to that observed in a concave nanomagnet. Figure 7.4(a) illustrates the magnetization patterns of a 100 nm × 100 nm diamond nanomagnet for various thicknesses. In contrast, the magnetization patterns of a concave nanomagnet with similar dimensions are shown in figure 7.4(b) for concavity depths of 10 nm, 15 nm and 20 nm.

It can be seen that while the diamond nanomagnets are susceptible to increased incoherent switching of the magnetization as its thickness increases, the concave nanomagnets show a trivial amount of incoherence (hence, the magnetization patterns of only three values of thickness – 5 nm, 20 nm, and 30 nm are shown). This insensitivity is prevalent even at larger thicknesses (with the same lateral dimensions). This is because the concave nanomagnets have a higher value of magnetostatic anisotropy energy, which dominates the exchange energy, thereby resulting in coherent magnetization switching. Figure 7.4(c) represents this phenomenon in terms of the incoherence percentage of the nanomagnets, calculated as the percentage of the magnetization vectors aligned along the $+x$ direction (final settled state) after a 90° rotation from the hard axis ($+y$ axis). Therefore, an incoherence percentage of 0% represents a complete rotation and settling of all magnetization vectors within a nanomagnet to the easy axis along the $+x$ axis. In the diamond nanomagnet, the incoherence percentage

(a)

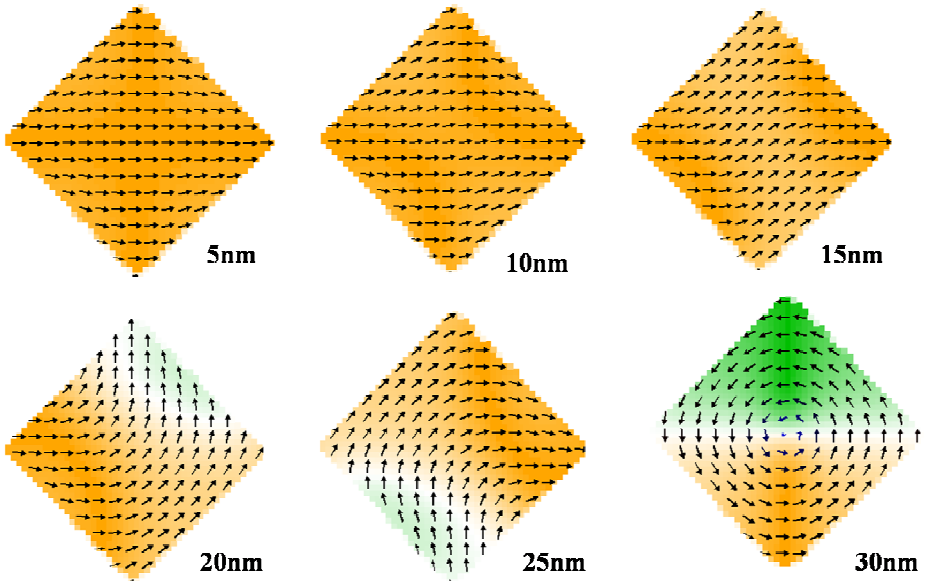

(b)

Concave Nanomagnet	t=5(nm)	t=20(nm)	t=30(nm)
d=10(nm)	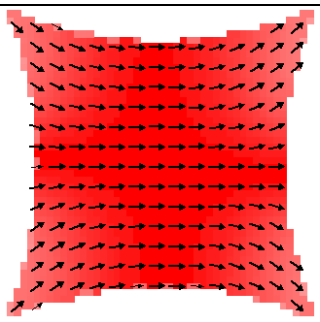	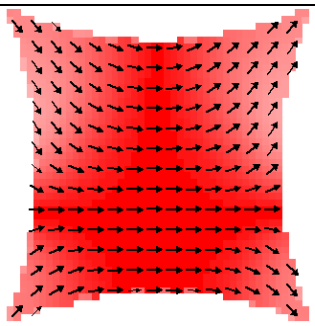	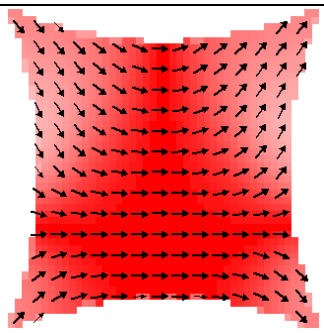
d=15(nm)	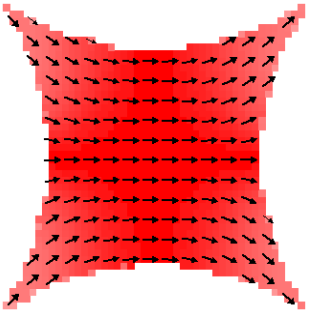	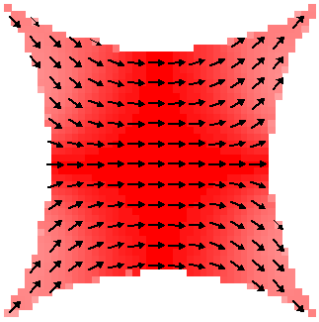	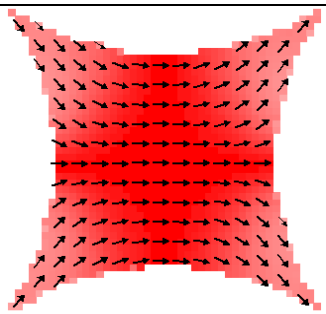
d=20(nm)	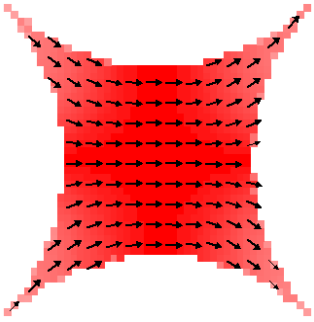	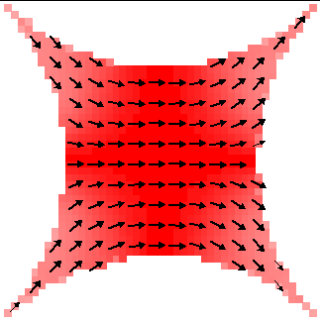	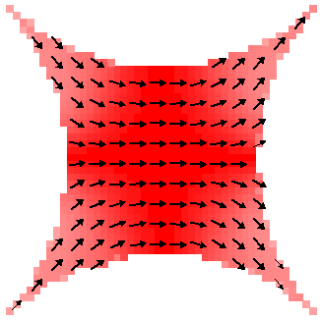

(c)

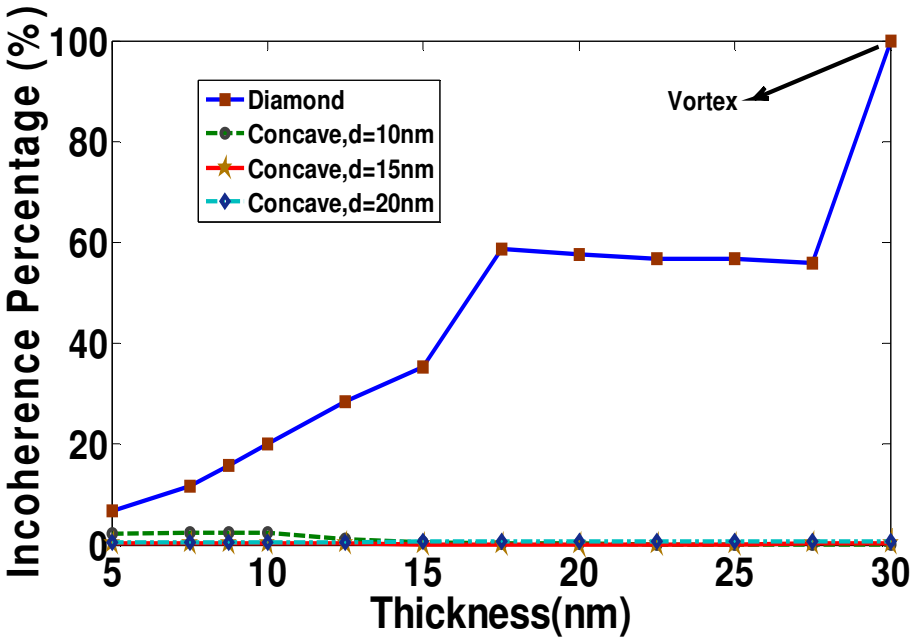

Figure 7.4. Magnetization patterns of a 100 nm × 100 nm (a) diamond nanomagnet, and (b) concave nanomagnet, for various thicknesses, *t*, and concavity depths, *d*. (c) The percentage of incoherent switching in diamond and concave nanomagnets vs. thickness.

values are ~ 6.7% and 20% for a thickness of 5 nm and 10 nm (figure 7.4(c)). However, for thicknesses greater than 17 nm, we see this incoherence percentage value rise to ~ 60% resulting in a high rate of inaccurate switching as well as an increase in energy dissipation during the magnetization switching; for a thickness of 30 nm, a vortex state arises, resulting in 100% incoherence in switching.

7.4.3 Magnetization Dynamics

Thus far, micromagnetic simulation results studying the magnetization characteristics of diamond- and concave-shaped nanomagnets have shown that concave nanomagnets entail coherent magnetization switching modes with an incoherence percentage rate that is near zero, for a variety

of thicknesses. The diamond nanomagnets, on the other hand, show increasing levels of incoherent switching with increasing thickness. In this section, we investigate the time evolution of these structures using OOMMF, in order to study the magnetization dynamics as the magnetization rotates from the hard axis and settles to its easy axis. The following two scenarios are examined. In figure 5(a), considering a (100×100×10) nm concave nanomagnet (d = 20 nm), the initial magnetization was set along the hard axis (ϕ_0 = 45°) with a 10° out-of-plane component, θ_0 = 80° (when θ = 90°, the magnetization vector lies in the plane of the nanomagnet). The resulting torque generated, $\left|\vec{M} \times \vec{H}\right|$, causes the magnetization to rotate to the easy axis along the +x direction, with a settling time of just ~ 0.5 ns. The magnetization dynamics are then examined for a diamond nanomagnet of similar dimensions, with its magnetization vector having the same initial configuration (ϕ_0 = 45°, θ_0 = 80°). The results, shown in figure 5(b), demonstrate an 'S' state switching mode (also with settling time of ~ 0.5 ns) resulting in an incoherence percentage of 20% in this diamond nanomagnet.

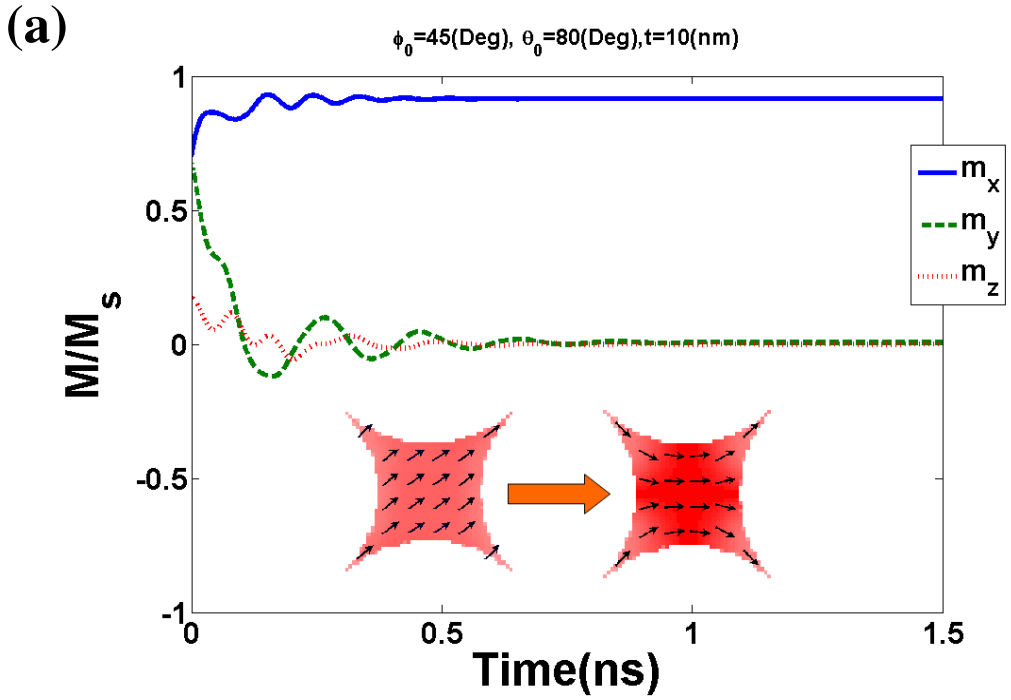

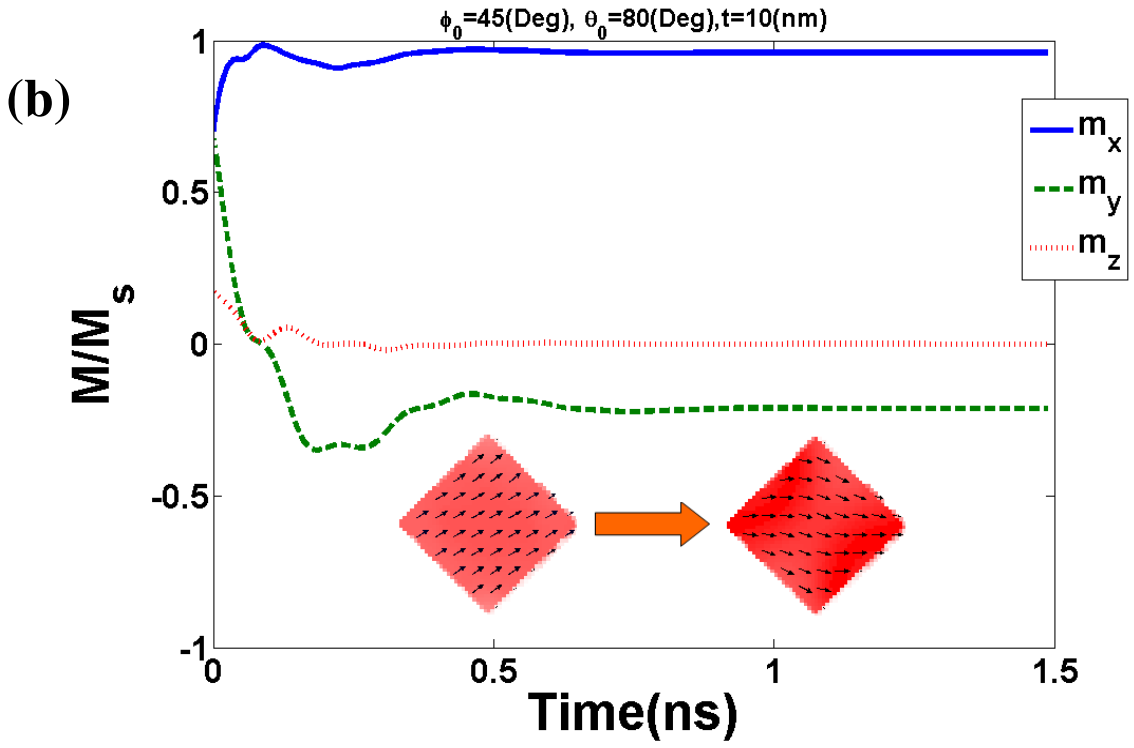

Fig7.5. Time evolution of the magnetization vector with an initial configuration of ϕ_0 = 45°, θ_0 = 80° for (a) concave nanomagnet, and (b) diamond nanomagnet.

7.4.4 Strain control of 4-State nanomagnets

It was shown that magnetization of four sate nanomagnet can be controlled by mechanical stress (σ) [9-10]. Here, we use the OOMMF to simulate magnetization dynamics of a concave 4-state nanomagnet under stress. The purpose is to show this tiny element can be used as memory component and low energy strain clocking can control its magnetization dynamics. Fig 7.6(a) shows a 4-state concave nanomagnet with dimension of 100nm x 100nm and thickness of 6nm. The 20(MPa) stress is applied along (010) direction for $0 \leq t \leq 0.1(ns)$ and can move the

magnetic moments coherently to the hard axis and ultimately to another easy axis by achieving a 90(Deg) rotation.

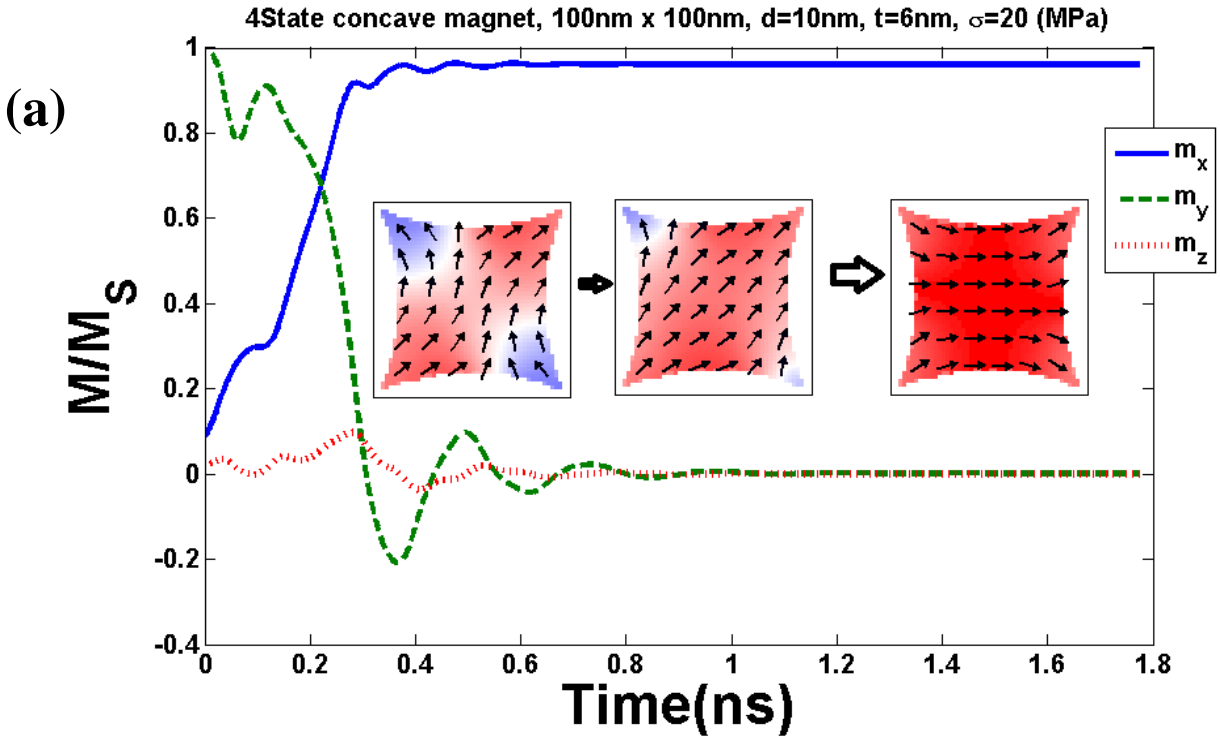

Fig 7.6(a). 90(Deg) magnetization switching from (010) to (100) with compressive stress of 20(MPa).

By considering binary bits of "1" or "0" along easy axes (010 and 100) of this 4-state nanomagnet, the switching between these bits would be possible by compressive and tensile stress along (010). In the second step, by applying 20(MPa) tensile stress along (010) the magnetization on nanomagnet would rotated from (100) to (010). This process just takes 0.6ns rotation from one easy axis to another one. The magnetization switching under tensile stress is shown in Fig 7.6(b).

(b)

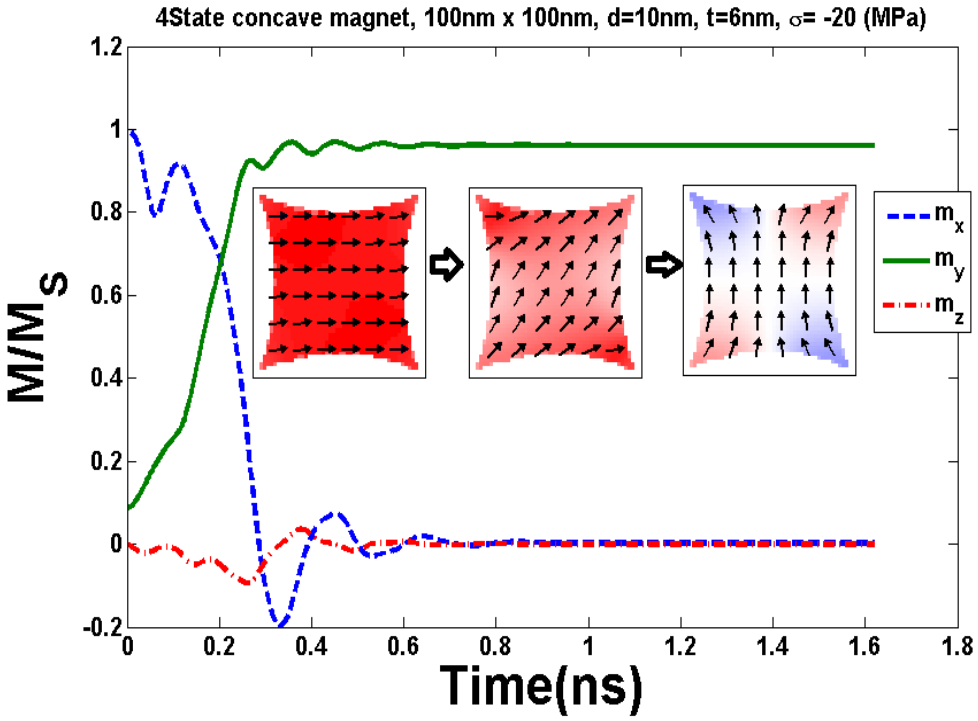

Fig 7.6(b). 90(Deg) magnetization switching from (100) to (010) with tensile stress of 20(MPa).

In order to benchmarking OOMMF simulation for stress induced magnetization dynamics, we benchmark LLG with OOMMF for and ellipsoid of 105nm x 95nm and t=6 nm under compressive stress of 10(MPa). The result shows (Fig 7.6 c) good agreement between LLG and OOMMF.

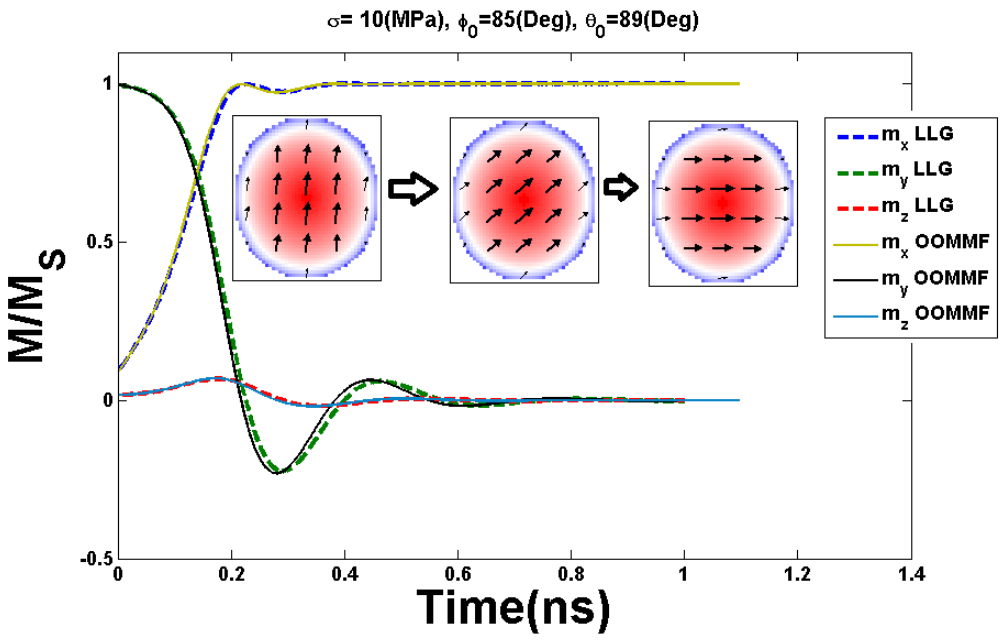

Fig 7.6(c). Benchmarking LLG and OOMMF for an ellipsoid.

7.5 Discussion

Four-state nanomagnets possessing fourfold, symmetric anisotropy fields, with energy barriers of ~ 1 eV, can be implemented in non-Boolean applications such as memory [86, 87], logic devices like four-state NOR gate [9] as well as in higher order applications such as image recognition and processing [10] and associative memory [29]. This study investigated the magnetization characteristics of a four-state diamond nanomagnet and, in particular, the incoherent switching modes that arise as the thickness increases. Through shape engineering of the edges, concave nanomagnets are created and the subsequent deviation in the uniform magnetization due to configurational anisotropy [15] results in an increase in the switching field of the nanomagnets. This effect is accompanied by coherent switching modes (lower incoherence percentages as the

concavity depth, *d*, increases), regardless of the nanomagnet thickness, thereby making concave-shaped nanomagnets more reliable than diamond nanomagnets during magnetization reversal. Furthermore, it is important to emphasize the limitations associated with nanolithography when fabricating a precise diamond-shaped nanomagnet having sides of equal dimensions (100 nm). It has been observed that a divergence of 15% from the nominal value results in the creation of a two-state, rather than the desired four-state, nanomagnet.

7.6 Four-State nanomagnetic device fabrication

The fabrication process for many nanomagneticdevices rely primarily on techniques that are in widespread use in the nanoscience community. The regular processes used are(i) Electron-beam resist (PMMA) coating on silicon wafer followed by (ii) Electron beam lithography (E-beam lithography) followed by (iii) Si wafer sample development by MIBK:IPA , (iv) Deposition : Electronbeam evaporation for magnetic alloys such as Ni and Co and RF Sputtering for deposition of rare-earth magnetic materials such as Terfenol-D, (v) lift off by acetone and finally (vi) topography and magnetic characterization by AFM and MFM respectively.

Electron beam lithography: In order to create a nanostructure, e-beam lithography is used. Here, computer-generated patterns in nanoscale would be transfer to a flat Si wafer or any flat surface like PZT. There is Nanometer Pattern Generation System (NPGS) software in which mask files can be created and nanomagnetic devices with any arbitrary shape can be created in its CAD system. This file is printed by an electron beam writer onto a silicon or PZT substrate coated with polymethyl-methacrylate(PMMA) resist. The tool we used was a Hitachi SU-70 30kV system

located at the VCU Nanocharacterization center. The configuration of this system is shown in the Fig 7.6(d).

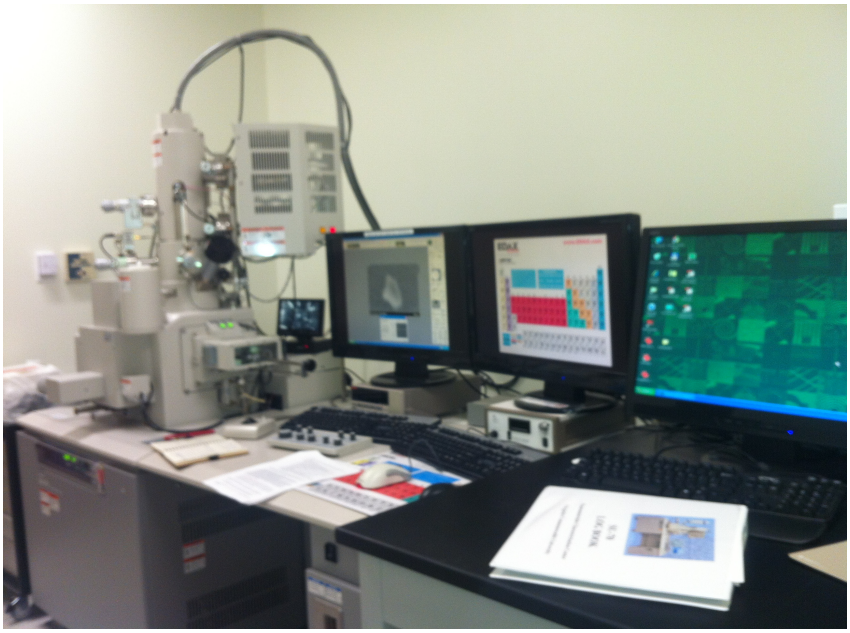

Fig.7.6 (d). The Hitachi SU-70 is used for SEM and E-beam lithography.

Upon completion of our device fabrication, the quality of our nanostructures was checked by a scanning electron microscopy(SEM). The exposed PMMA on our wafer was developed in a cold solution of 1:3 MIBK: IPA. The place which we used to develop our samples is shown in the Fig 7.7.

Fig 7.7 Schematic view of HOOD that the development was done there.

Metal Deposition: There were two methods available to us at VCU to deposit a magnetic film/nanostructure on our sample.

(i) Electron beam evaporation: This machine use electron beam to heat the magnetic alloys which are placed in a crucible. The beam heats this pure alloy to a temperature that causes the metal to evaporate at an appreciable rate and get deposited on the surface of the sample. We deposit 5nm Ti for adhesion and then 15nm Ni (or Co) on top of Ti. In order to prevent oxidation, we can deposit 2nm gold on top of Ni.

(ii) Sputtering: The secondary method for deposition of a magnetic thin layer is to use RF Sputtering machine which it is located in VCU cleanroom. This machine may be used to deposit Terfenol-D.

Fig 7.8 . The RF Sputtering picture in VCU Engineering Cleanroom for depositing Terfenol-D.

Lift-off: The final step of the nanofabrication is lift-off. This removes the metal deposited on the resist leaving behind the metallic nanostructures deposited in the exposed pores (created when the exposed resist was developed). We used acetone that was heated to 55 (C) . After about 5 minsthe PMMA and the metal on top was lift-off and then, using high frequency ultrasonic bath, the residual PMMA and other contaminants on the wafer are removed. Finally, the sample is removed from acetone and rinsed with isopropanol and blown with N_2 gun. Then the SEM was used to image the surface of the sample and verify the quality of our magnetic devices. The figures below show SEM image of a 200nm × 200nm lateral dimension 4-state nanomagnet with three different concavity depth of 20nm, 30nm, and 40nm.

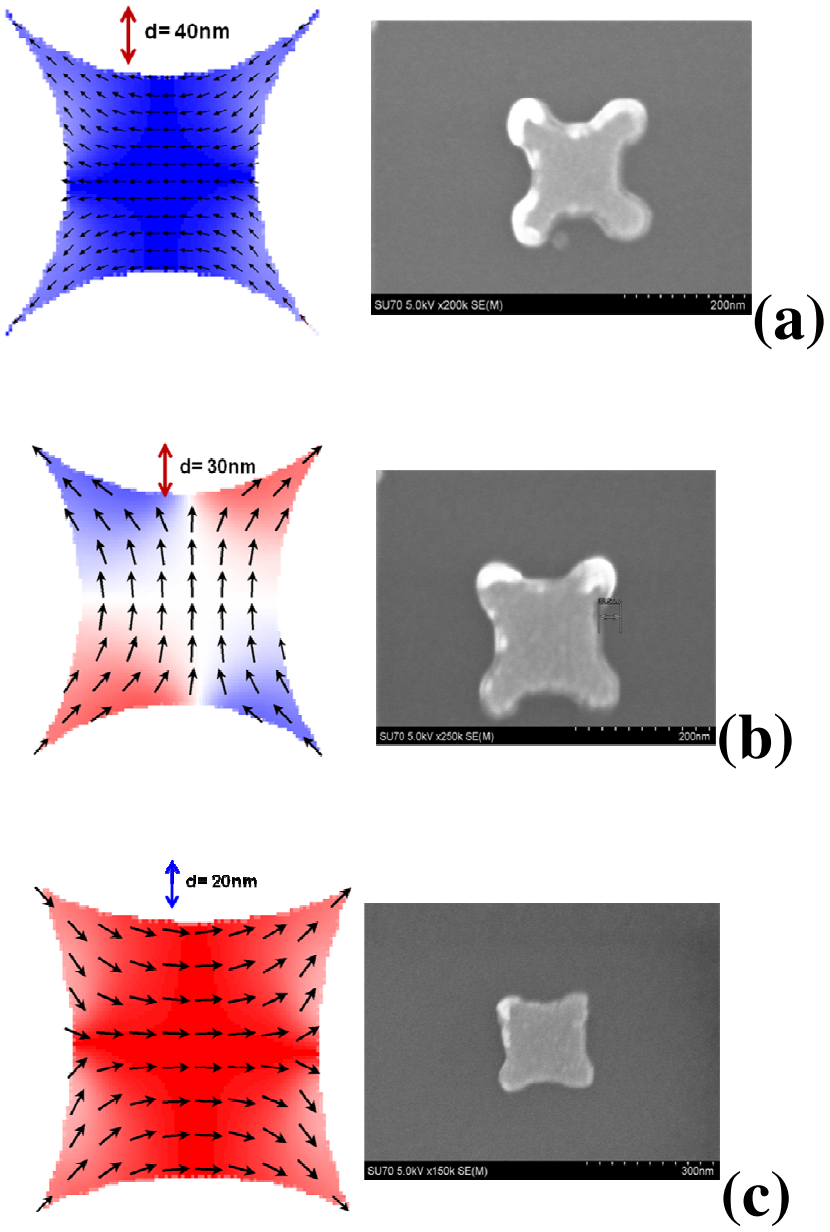

Fig 7.9 The OOMMF and SEM images of 4-state concave nanomagnets with different concavity depth was created by electron beam lithography and Ni was used as its magnetic material. (a) d=40(nm) , (b) d=30(nm) and (c) d=20 (nm).

Magnetic Force Microscopy

Magnetic force microscopy (MFM) is a scanning technique for mapping the stray magnetic fields around the surface of the nanomagnet or magnetic material. After determining the field around our magnet, it is possible to figure out the magnetization state of the nanomagnet.

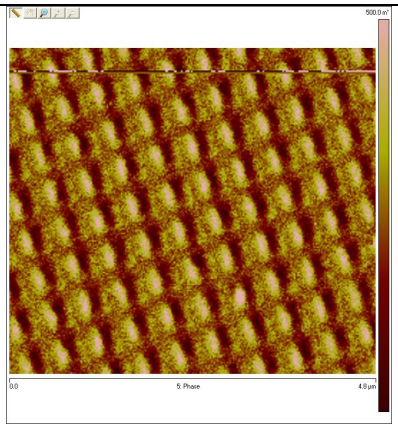

Fig 7.10 (a) MFM image showing the magnetic direction of 4-state nanomagnet array.

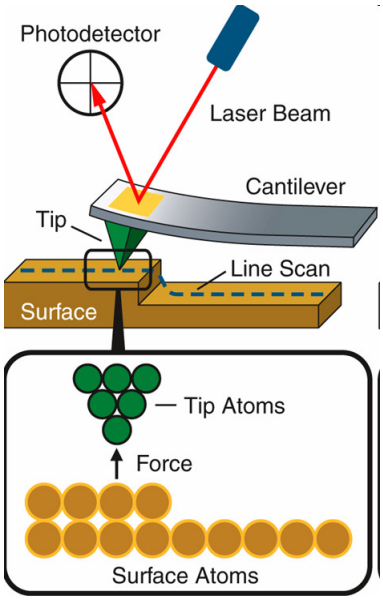

Fig 7.10 (b) Illustration of the scanning process: MFM passing over the surface of a magnetic material[98].

The topographic map is first obtained in the MFM mode and then the tip rescanned over the surface. It should be mentioned that MFM tips are coated with magnetic material which makes them experience a force dependent on the local magnetic field. As result, by passing tip during the second scan over the nanomagnet its magnetization orientation can be found. The Fig 7.10 (a) shows such a MFM image obtained by the AFM/MFM in Fig 11.

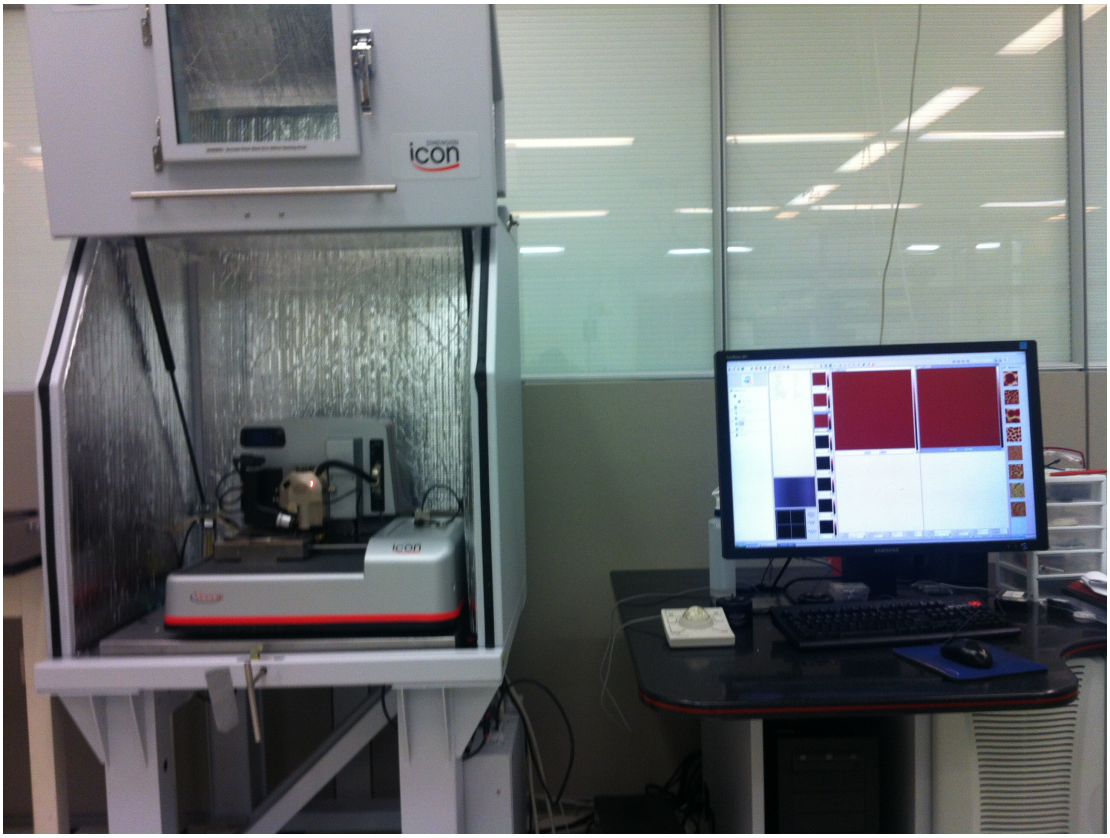

Fig 7.11 Schematic view of AFM/MFM device for magnetic characterization at NCC in VCU.

7.7 Conclusion

In this section, we have studied the influence of configurational anisotropy on the magnetization switching modes of nanomagnets of two distinct shapes: (i) diamond, and (ii) concave, in the

pursuit of reliable and efficient nanomagnets during magnetic field-induced switching. Various criteria were numerically examined for these two shapes, such as size, magnetic hysteresis, concavity depth and thickness, in order to determine the ideal shape for coherent and reliable magnetization switching for future magnetoelectonic devices. It was shown that concave nanomagnets, previously shown to generate four stable states due to configurational anisotropy, also tend to have coherent magnetization switching modes. While diamond nanomagnets are susceptible to incoherence in switching with increasing thickness, concave nanomagnets of similar dimensions show little to no incoherence and are, in fact, quite robust to variations in thickness, a vital attribute in terms of fabrication of nanostructures.

Chapter 8

Conclusions and Future work

8.1 Conclusions

In this dissertation, we proposed and extensively studied several multiferroic nanomagnet based logic architectures. During the course of this work there has been a spurt of research on multiferroic computing devices in several research groups [4, 5, 6, 7, 8, 9, 11, 13, 58, 70, 88, 89, 90, 91, 95, 96] However, many challenges still remain before SML can be considered as a viable commercial technology.

In chapter 3, we discussed the possibility of transferring information from one point to another in a nanomagnetic chain as well as performing nanomagnetic computation with a NAND gate clocked by mechanical strain. We then showed with Landau Lifshitz Gilbert (LLG) equation based simulations in the absence of thermal noise that this new nanomagnetic computing paradigm is both feasible and likely to be extremely energy efficient as the magnetostrictive nanomagnet can be clocked in ~ 1 ns by applying ~ few mV to the piezoelectric layer below it.

In chapter 4, we studied the effect of thermal noise on the dynamic switching error in multiferroic nanomagnetic logic devices. This study was performed by adding thermal

noise to our LLG simulations. It was shown that thermal noise causes perturbations in the magnetization switching trajectory that can lead to appreciable errors even in the presence of significant dipole coupling to "guide" the magnenetization to switch to the correct state. Typically, thermal noise leads to a distribution of magnetization orientation in both the in plane and out of plane directions in a single domain nanomagnet. The in-plane distribution creates switching tails while the out-of-plane distribution can lead to deleterious precessional torque that increases the switching failures. The reliability of a multiferroic NAND gate in the presence of thermal noise was also studied. We studied effects of (i) Dipole effect (ii) Stress level (iii) Clock frequency and (iv) Temperature on the switching error in strain clocked nanomagnetic devices and specifically on the performance of a strain clocked NAND gate.

In chapter 5, a lower analytical bound for energy dissipation as a function of switching error was derived [for a practical scenario when the dipole coupling field or “tilt” is always present and the barrier is a two-well potential that is eroded and then restored]. We explained how the out-of-plane magnetization distributions lead to higher energy dissipation than this bound, for a given switching error.

In chapter 6, we studied nanomagnetic computing device designs that are amenable to clocking withsurface acoustic waves (SAW) that obviates the need to make lithographic contacts to each nanomagnet for individual clocking. We showed with preliminary LLG simulations in the absence of thermal noise that show that NAND gate designs and logic wires clocked by SAW waves are indeed feasible.

In chapter 7, weexplored the use of shape engineering to create nanomagnets with four states and specifically studied if such geometries are amenable to coherent switching of magnetization. A comparison of single-domain (or macro-spin) LLG analysis with modified OOMMF based models that allow incoherent switching was performed to get a preliminary idea of the possible extent of deviation of magnetization dynamics from the macro-spin approximation. Two different shapes: diamond (square) and concavewere studied and it was found that the concave nanomagnet is better suited for coherent switching of magnetization between the four stable states.

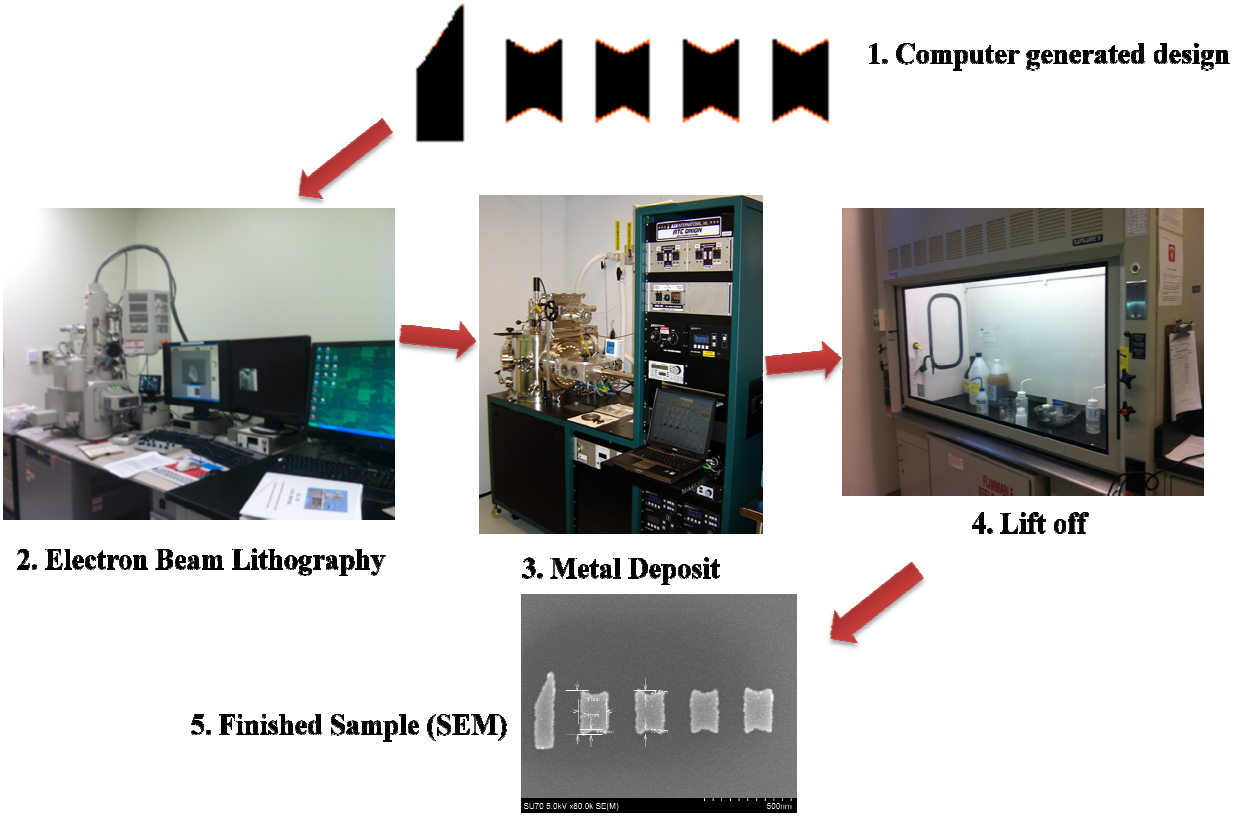

Fig 8.1 Process of nanofabrication to nanomagnetic devices

8.2 Future work

While multiferroic nanomagnets are possibly one of the most energy efficient (~ 1 aJ/bit) switches extant (http://arxiv-web3.library.cornell.edu/abs/1404.2980), many challenges remain inthe practical application of multiferroic nanomagnetic logic in commercial computing technology. Some of the problems and future work that may alleviate some of these issues are discussed.

One dominant challenge, not only in dipole coupled multiferroic logic discussed in this dissertation, but also in all dipole coupled nanomagnetic architectures, is the dynamic switching error due to thermal noise. Perhaps, further research in use of appropriate geometry, pulse shaping, etc may reduce the error to ~10^{-6} but this is still unacceptable for conventional Boolean logic. There, however, will always be niche applications for wearable or building mounted monitoring devices, face recognition, etc where such error rates (few bits being wrong) are not critical but low energy dissipation is a premium so that the processors can be run without a battery (using energy harvested from the environment). Such applications may drive the use of these devices in the future. Furthermore, the modeling tools and insights from this PhD thesis can be used to study architectures such as hybrid multiferroic-MTJ and neuromorphic architectures that are more fault tolerant to errors in switching due to thermal noise at room temperature.

Experimentally, substrate clamping could be an issue for piezoelectric layers below 100 nm but an elegant scheme discussed in Ref 97 may provide a way to solving this problem.

References:

[1]. R. P. Cowburn and M. E. Welland, “Room temperature magnetic quantum cellular automata”, Science, 485, 2003.

[2]. G. Csaba, A. Imre, G. H. Bernstein, W. Porod and V. Metlushko, “Nanocomputing by field-coupled nanomagnets”, IEEE Trans. Nanotechnol., 1, 209, 2002.

[3]. S. Salahuddin and S. Datta, “Interacting systems for self correcting low power switching”, Appl. Phys. Lett., 90, 093503, 2007.

[4]. J. Atulasimha and S. Bandyopadhyay, "Bennett clocking of nanomagnetic logic using multiferroic single-domain nanomagnets", Appl. Phys. Lett., 97, 173105, 2010.

[5]. **M. Salehi Fashami**, K. Roy, J. Atulasimha, S. Bandyopadhyay, “Magnetization dynamics, Bennett clocking and associated energy dissipation in multiferroic logic”, Nanotechnology, 22, 155201, 2011.

[6]. **M.Salehi Fashami**, J. Atulasimha, S. Bandyopadhyay, "Magnetization Dynamics, Throughput and Energy Dissipation in a Universal Multiferroic Nanomagnetic Logic Gate with Fan-in and Fan-out", Nanotechnology, 23, 105201, 2012.

[7]. K. Roy, S. Bandyopadhyay and J. Atulasimha, “Hybrid spintronics and straintronics: A magnetic technology for ultra low energy computing and signal processing”, Appl. Phys. Lett., 99, 063108, 2011.

[8]. K. Roy, S. Bandyopadhyay and J. Atulasimha, "Energy dissipation and switching delay in stress-induced switching of multiferroic devices in the presence of thermal fluctuations", J. of App. Phys., 112, 023914, 2012.

[9]. N. D’Souza, J. Atulasimha and S. Bandyopadhyay, “Four-state nanomagnetic logic using multiferroics”, J. Phys. D: App. Phys.,44 265001, 2011.

[10]. N. D’Souza, J. Atulasimha and S. Bandyopadhyay, "An ultrafast energy-efficient image reconstructor implemented with nanomagnets possessing biaxial magnetocrystalline anisotropy", IEEE Trans on Nanotechnology, in-press.

[11]. **M. Salehi Fashami**, K. Munira, J. Atulasimha, S. Bandyopadhyay and A. W. Ghosh, “Switching of dipole coupled multiferroic nanomagnets in the presence of thermal noise: reliability analysis of hybrid spintronic-straintronic nanomagnetic logic”.*Nanotechnology, IEEE Transactions on* , vol.12, no.6, pp.1206,1212, Nov. 2013

[12]. K. Munira, S. Nadri, M. B. Forgues, **M.Salehi Fashami**, J. Atulasimha, S. Bandyopadhyay and A. W. Ghosh, "Reducing error rates in straintronic multiferroic nanomagnetic logic by pulse shaping", under review, IEEE Trans. on. Electron Devices.

[13]. M. Salehi Fashami, J. Atulasimha, and S. Bandyopadhyay. "Energy dissipation and error probability in fault-tolerant binary switching." Scientific reports 3 (2013).

[14]. en.wikipedia.org

[15]. R .P .Cowburn, D. K. Koltsov, A.O.Adeyeye, M. E .Welland and D .M .Tricker 1999 *Phys. Rev. Lett.***83** 1042.

[16]. B. Behin-Aein, D. Datta, S. Salahuddin, and S. Datta. "Proposal for an all-spin logic device with built-in memory." Nature nanotechnology 5, no. 4 (2010): 266-270.

[17]. S. Bandyopadhyay, and M. Cahay. "Electron spin for classical information processing: a brief survey of spin-based logic devices, gates and circuits." Nanotechnology 20, no. 41 (2009): 412001.

[18]. M.T. Alam, M. J. Siddiq, G. H. Bernstein, M. Niemier, W. Porod, and Xi. S. Hu. "On-chip clocking for nanomagnet logic devices." *IEEE Transactions on Nanotechnology* 9, no. 3 (2010): 348-351.

[19]. D. C. Ralph, and M. D. Stiles. "Spin transfer torques." Journal of Magnetism and Magnetic Materials 320, no. 7 (2008): 1190-1216.

[20]. M. Yamanouchi, D. Chiba, F. Matsukura, and H. Ohno. "Current-induced domain-wall switching in a ferromagnetic semiconductor structure." Nature 428, no. 6982 (2004): 539-542.

[21]. H. Tanigawa, T. Koyama, G. Yamada, D. Chiba, S. Kasai, S. Fukami, T. Suzuki et al. "Domain wall motion induced by electric current in a perpendicularly magnetized Co/Ni nano-wire." Applied Physics Express 2, no. 5 (2009): 053002..

[22]. Chikazumi S 1964 *Physics of Magnetism* John Wiley & Sons, New York.

[23]. J.Atulasimha," Characterization and modeling of the magnetomechanical behavior of iron-gallium alloys",UMD, 2006.

[24]. Physics.nist.gov/TechAct.2001/Div841/div841h.html

[25]. R. P. Cowburn , D. K. Koltsov, A. O. Adeyeye, M. E. Welland, and D. M. Tricker. "Single-domain circular nanomagnets." Physical Review Letters 83, no. 5 (1999): 1042.

[26]. M. J. Donahue, D. G. Porter, National Institute of Standards, and Technology (U.S.).OOMMF user's guide [microform] / M.J. Donahue, D.G. Porter. U.S. Dept. of

Commerce,Technology Administration, National Institute of Standards and Technology, Gaithersburg, MD, version 1.0. edition, 1999.

[27]. A. P. Guimarães. Principles of nanomagnetism. Springer, 2009.

[28]. G.Bertotti, C.Serpico, and I. D. Mayergoyz ." Nonlinear Magnetization Dynamics in Nanosystems (Elsevier Series in Electromagnetism)". 2008, Elsevier, Oxford.

[29]. V. Roychowdhury, D. Janes, S. Bandyopadhyay and X.Wang ."Collective computational activity in self-assembled arrays of quantum dots: a novel neuromorphic architecture for nanoelectronics". *Electron Devices, IEEE Trans.*2002.**43** 1688–99.

[30]. K. J. Lee, N. Y. Park, and T. D. Lee. "Numerical study of spin relaxation by thermal fluctuation: Effect of shape anisotropy." *Journal of Applied Physics* 89.11 (2001): 7460-7462.

[31]. G.Brown, M. A. Novotny, and P. A. Rikvold. "Langevin simulation of thermally activated magnetization reversal in nanoscale pillars." *Physical Review B* 64.13 (2001): 134422.

[32]. G. M. Müller, J. Walowski, M. Djordjevic, G.X. Miao, A. Gupta, A. V. Ramos, K. Gehrke, V. Moshnyaga, K. Samwer, J. Schmalhorst, A. Thomas, A. Hütten, G. Reiss, J. S. Moodera, and M. Münzenberg, "Spin Polarization in Half-Metals Probed by Femtosecond Spin Excitation", Nature Mater. 8, 56 (2008).

[33]. K. Ried, M. Schnell, F. Schatz,M. Hirscher,B. Ludescher, W. Sigle andH. Kronmuller 1998 *Phys. Stat. Sol. (a)***167**, 195; Abbundi R and Clark A E 1977 *IEEE Trans. Mag.***13** 1547.

[34]. R. A. Kellogg and A. B. Flatau 2008 J. of Intelligent Material Systems and Structures **19** 583.

[35]. D. E. Nikonov, G. I. Bourianoff, G. Rowlands, and I. N. Krivorotov, "Strategies and tolerances of spin transfer torque switching." Journal of Applied Physics 107, no. 11 (2010): 113910.

[36]. http://www.itrs.net/Links/2009ITRS/2009Chapters_2009Tables/2009_Interconnect.pdf.

[37]. http://www.piezo.com/prodmaterialprop.html.

[38]. B. Behin-Aein, S. Salahuddin, and S. Datta. "Switching energy of ferromagnetic logic bits," Nanotechnology, IEEE Transactions on 8, no. 4 (2009): 505-514.

[39]. CORE9GPLL_HCMOS9_TEC-4.0 Databook, ST Micro (2003).

[40]. D.B.Carlton, N.C.Emley, E.Tuchfeld, J. Bokor, "Simulation studies of Nanomagnet-Based Logic Architecture',Nano Letters Vol.8,No.12 pages 4173-4178 (2008).

[41]. A.Imre , G.Csaba , L.Ji , A.Orlov ,G.H. Bernstein , W.Porod, "Majority logic gate for magnetic quantum-dot cellular Automata", Science Vol 311 page 205 (2006).

[42]. R.P.Cowburn , M.E.Welland, "Room temperature Magnetic Quantum Cellular Automata", Science Vol 287 page 1466 (2000).

[43]. S.A.Wolf , D.D.Awschalom, R.A.Buhrman, J.M.Daughton, S. V. Molnar ,M.L.Roukes, A.Y.Chtchelkanova , D.M.Treger ,"Spintronics: A spin-based Electronics Vision for the future", Science vol 294 page 1488 (2001).

[44]. C. Augustine, B. Behin-Aein, and K. Roy, "Nano-magnet based ultra-low power logic design using non-majority gates." In Nanotechnology, 2009. IEEE-NANO 2009. 9th IEEE Conference on, pp. 870-873. IEEE, 2009.

[45]. L. Gilbert "A phenomenological theory of Damping in Ferromagnetic materials", IEEE Transaction on magnetics, Vol 40, No 6 (2004)

[46]. R. Abbund, and A. E. Clark. "Anomalous thermal expansion and magnetostriction of single crystal Tb. 27 Dy. 73 Fe 2." Magnetics, IEEE Transactions on 13, no. 5 (1977): 1519-1520..

[47]. R. Landauer, "Uncertainty principle and minimal energy-dissipation in the computer", Inter, J. Theoretical Physics, 21, 283-297, 1982.

[48]. S. Bandyopadhyay , B. Das, and A. E. Miller. "Supercomputing with spin-polarized single electrons in a quantum coupled architecture." Nanotechnology 5, no. 2 (1994): 113.

[49]. N. D'Souza, J. Atulasimha, and S. Bandyopadhyay. "Four-state nanomagnetic logic using multiferroics." Journal of Physics D: Applied Physics 44, no. 26 (2011): 265001.

[50]. R.C. Calvin, V. V. Zhirnov, J.A. Hutchby and G.I. Bourianoff, "Energy barriers, demons and minimum energy operation of electronic devices", Fluctuation and Noise Letters, 5 (4), C29, 2005.

[51]. K. K. Likharev, “Classical and quantum limitations on energy consumption in computation,” *Int. J. Theor. Phys.*, vol. 21, pp. 311–325, 1982.

[52]. R. W. Keyes, and R. Landauer. "Minimal energy dissipation in logic." IBM Journal of Research and Development 14, no. 2 (1970): 152-157.

[53]. C. H. Bennett, Int. J. Theor. Phys.,**21,** 905 (1982).

[54]. S. Salahuddin, and S. Datta. "Interacting systems for self-correcting low power switching." Applied Physics Letters 90, no. 9 (2007): 093503-093503.

[55]. E. Fredkin, T. Toffoli, "Conservative logic" Int. J. Theor. Phys., 21 (1982), pp. 219–253

[56]. G.Csaba and W. Porod. "Behavior of nanomagnet logic in the presence of thermal noise." *Computational Electronics (IWCE), 2010 14th International Workshop on*. IEEE, 2010

[57]. B. Lambson, D. Carlton, and J. Bokor. "Exploring the thermodynamic limits of computation in integrated systems: Magnetic memory, nanomagnetic logic, and the landauer limit." Physical review letters 107, no. 1 (2011): 010604.

[58]. N. Tiercelin, Y. Dusch, A. Klimov, S. Giordano, V. Preobrazhensky, and P. Pernod, "Room temperature magnetoelectric memory cell using stress-mediated magnetoelastic switching in nanostructured multilayers", Appl. Phys. Lett. 99, 192507, 2011.

[59]. F. M. Spedalieri, A. P. Jacob, D. E. Nikonov, and V. P. Roychowdhury, "Performance of Magnetic Quantum CellularAutomata and Limitations Due to Thermal Noise", IEEE Transaction on Nnaotechnology, 10, 537, 2011,.

[60]. J. P. Strachan,V. Chembrolu, Y. Acremann, X.W. Yu, A. A. Tulapurkar, T. Tyliszczak, J. A. Katine, M. J. Carey, M. R. Scheinfein, H. C. Siegmann, and J. Stohr, "Direct Observation of Spin-Torque Driven Magnetization Reversal through Nonuniform odes", PRL 100, 247201, 2008.

[61]. D. Carlton, B. Lambson, A. Scholl, A. Young, P. Ashby, S. Dhuey and J. Bokor, "Investigation of Defects and Errors in Nanomagnetic Logic Circuits, IEEE Transaction on Nanaotechnology, **11**, 560, 2012.

[62]. H. E. Bömmel, and K. Dransfeld. "Attenuation of hypersonic waves in quartz." *Physical Review Letters* 2, no. 7 (1959): 298-299.

[63]. M. Bombeck, A. S. Salasyuk, B. A. Glavin, A. V. Scherbakov, C. Brüggemann, D. R. Yakovlev, V. F. Sapega et al. "Excitation of spin waves in ferromagnetic (Ga, Mn) As layers by picoseconds strain pulses." *Physical Review B* 85, no. 19 (2012): 195324.

[64]. M.Weiler, L. Dreher, C. Heeg, H. Huebl, R. Gross, M. S. Brandt, and S. T. B. Goennenwein. "Elastically driven ferromagnetic resonance in nickel thin films." *Physical Review Letters* 106, no. 11 (2011): 117601.

[65]. S.Davis, A. Baruth, and S. Adenwalla. "Magnetization dynamics triggered by surface acoustic waves." *Applied Physics Letters* 97, no. 23 (2010): 232507-232507.

[66]. O.Kovalenko, T.Pezeril, and V.V. Temnov. "New Concept for Magnetization Switching by Ultrafast Acoustic Pulses." *Physical Review Letters* 110, no. 26 (2013): 266602.

[67]. L. Thevenard, J. Y. Duquesne, E. Peronne, H. J. Bardeleben, H. Jaffres, S. Ruttala, J. M. George, A. Lemaître, and C. Gourdon. "Irreversible magnetization switching using surface acoustic waves." *Physical Review B* 87, no. 14 (2013): 144402.

[68]. S. Bandyopadhyay, andM. Cahay."Electron spin for classical information processing: a brief survey of spin-based logic devices, gates and circuits". *Nanotechnology***20** 4120012009

[69]. F.J. Albert, J. A. Katine, R. A. Buhrman and D. C. Ralph." Spin-polarized current switching of a Co thin film nanomagnet ", 2000, *Appl. Phys. Lett.***77** 3809

[70]. N. D'Souza, J. Atulasimha and S. Bandyopadhyay." An energy-efficient Bennett clocking scheme for 4-state multiferroic logic".2012 *Nanotechnology, IEEE Trans.* **11** 418–25.

[71]. A.Imre, G.Csaba , G. H. Bernstein, W.Porod and V.Metlushko. "Investigation of shape-dependent switching of coupled nanomagnets". *Superlattices Microstruct.*2003 .**34** 513–8.

[72]. R. Naik, C. Kota, J. Payson and G. Dunifer 1993 Ferromagnetic-resonance studies of epitaxial Ni, Co, and Fe films grown on Cu(100)/Si(100). *Phys. Rev. B. Condens. Matter***48** 1008–13.

[73]. P. P.Chow " Molecular Beam Epitaxy *Thin film processes II* ed J L Vossen and W Kern . 1991 .(Boston: Academic Press).

[74]. E.Boyd." Magnetic anisotropy in single-crystal thin films ".*IBM J. Res. Dev.***4** 1960 .116–29.

[75]. C. P. Wang ." A Coupled Magnetic Film Device for Associative Memories".1968 *J. Appl. Phys.***39** 1220

[76]. W.T.Siegle ."Exchange Coupling of Uniaxial Magnetic Thin Films". *J. Appl. Phys.*1965.**36** 1116.

[77]. F.Lee." Shape-induced biaxial anisotropy in thin magnetic films". *IEEE Trans. Magn.*1968**4** 502–6.

[78]. R. P. Cowburn, D. K. Koltsov, A. O. Adeyeye and M. E. Welland."Designing nanostructured magnetic materials by symmetry" *Europhys. Lett.*1999**48** 221–7.

[79]. P. Vavassori , D. Bisero, F. Carace, A. di Bona, G. Gazzadi, M.Liberati and S.Valeri "Interplay between magnetocrystalline and configurational anisotropies in Fe(001) square nanostructures". *Phys. Rev.* 2005 . *B***72** 054405.

[80]. B. Lambson, Z. Gu, D.Carlton, S.Dhuey, A.Scholl, A.Doran, A. Young and J. Bokor ." Cascade-like signal propagation in chains of concave nanomagnets *Appl. Phys. Lett.*2012.**100** 152406.

[81]. B. Lambson, Z. Gu, M. Monroe, S. Dhuey, A.Scholl and J.Bokor. "Concave nanomagnets: investigation of anisotropy properties and applications to nanomagnetic logic". *Appl. Phys. A*2013**111** 413–21.

[82]. L. Torres, E. Martinez, L. Lopez-Diaz and J.Iñiguez ." Micromagnetic switching of patterned square magnetic nanostructures". *J. Appl. Phys.*2001**89** 7585.

[83]. R. P.Cowburn and M.Welland ."Micromagnetics of the single-domain state of square ferromagnetic nanostructures". *Phys. Rev.*1998. *B***58** 9217–26.

[84]. G. Dewar ."Effect of the large magnetostriction of Terfenol-D on microwave transmission." *J. Appl. Phys.*1997 .**81** 5713.

[85]. Z. Shi, C. Wang, X. Liu and C.Nan."A four-state memory cell based on magnetoelectric composite". *Chinese Sci. Bull.*2008**53** 2135–8.

[86]. T. Uemura, T. Marukame, K. Matsuda and M.Yamamoto ."Four-State Magnetoresistance in Epitaxial CoFe-Based Magnetic Tunnel Junctions." *IEEE Trans. Magn.*2007 .**43** 2791–3

[87]. V. Roychowdhury, D. Janes, S. Bandyopadhyay and X.Wang ."Collective computational activity in self-assembled arrays of quantum dots: a novel neuromorphic architecture for nanoelectronics". *Electron Devices, IEEE Trans.*2002.**43** 1688–99.

[88]. N. A. Pertsev , and H. Kohlstedt. "Resistive switching via the converse magnetoelectric effect in ferromagnetic multilayers on ferroelectric substrates." *Nanotechnology* 21, no. 47 (2010): 475202.

[89]. N. Tiercelin, Y. Dusch, V. Preobrazhensky, and P. Pernod. "Magnetoelectric memory using orthogonal magnetization states and magnetoelastic switching." *Journal of Applied Physics* 109, no. 7 (2011): 07D726.

[90]. S. Giordano, Y. Dusch, N. Tiercelin, P. Pernod, and V. Preobrazhensky. "Combined nanomechanical and nanomagnetic analysis of magnetoelectric memories." *Physical Review B* 85, no. 15 (2012): 155321.

[91]. S. Giordano, Y. Dusch, N. Tiercelin, P. Pernod, and V. Preobrazhensky. "Thermal effects in magnetoelectric memories with stress-mediated switching." *Journal of Physics D: Applied Physics* 46, no. 32 (2013): 325002.

[92]. K. Roy, S. Bandyopadhyay, and J. Atulasimha. "Switching dynamics of a magnetostrictive single-domain nanomagnet subjected to stress." *Physical Review B* 83, no. 22 (2011): 224412.

[93]. T. Suzuki, H. Tanigawa, Y. Kobayashi, K. Mori, Y. Ito, Y. Ozaki, K. Suemitsu et al. "Low-current domain wall motion MRAM with perpendicularly magnetized CoFeB/MgO magnetic tunnel junction and underlying hard magnets." In *VLSI Technology (VLSIT), 2013 Symposium on*, pp. T138-T139. IEEE, 2013.

[94]. D. A. Allwood, G. Xiong, C. C. Faulkner, D. Atkinson, D. Petit, and R. P. Cowburn. "Magnetic domain-wall logic." *Science* 309, no. 5741 (2005): 1688-1692.

[95]. T. Wu, A. Bur, P. Zhao, K. P. Mohanchandra, K. Wong, K. L. Wang, C. S. Lynch, and G. P. Carman. "Giant electric-field-induced reversible and permanent magnetization reorientation on magnetoelectric Ni/(011)[Pb (Mg 1/3 Nb 2/3) O 3](1-x)–[PbTiO 3] x heterostructure." *Applied Physics Letters* 98, no. 1 (2011): 012504-012504.

[96]. H. K. Kim, L. T. Schelhas, S. Keller, J. L. Hockel, S. H. Tolbert, and G. P. Carman. "Magnetoelectric control of superparamagnetism." *Nano letters* 13, no. 3 (2013): 884-888.

[97]. J. Cui J. L. Hockel, P. K. Nordeen, D. M. Pisani,C. Liang, G. P. Carman and C. S. Lynch,"A method to control magnetism in individual strain-mediated magnetoelectric islands",*Applied Physics Letters* 103,(2013), 232905.

[98]. http://www.keysight.com/main/editorial.jspx?cc=US&lc=eng&ckey=1774141&nid=-33986.0.02&id=1774141